Fiber-Optic Parametric Amplifiers: Their Advantages and Limitations

by

Fatih Yaman

Submitted in Partial Fulfillment

of the

Requirements for the Degree

Doctor of Philosophy

Supervised by

Professor Govind P. Agrawal

The Institute of Optics
The College
School of Engineering and Applied Sciences

University of Rochester
Rochester, New York

2006

Curriculum Vitae

The author was born in Diyarbakir, in 1978 and grew up in Aydin, Turkey. He graduated first in his class with B.S. degrees in both Physics and Mathematics from Koc University, Istanbul in 2000. He then began graduate studies at the Institute of Optics same year. He has carried out his doctoral research in nonlinear fiber optics under the direction of Professor Govind P. Agrawal.

Publications

Journal Articles

F. Yaman, Q. Lin, and G. P. Agrawal, "A novel design for polarization-independent single-pump fiber-optic parametric amplifiers," submitted to IEEE Photon. Technol. Lett.

Q. Lin, F. Yaman, and G. P. Agrawal, "Photon-pair generation in optical fibers through four-wave mixing: role of Raman scattering and pump polarization," submitted to Phys. Rev. A.

F. Yaman, Q. Lin, S. Radic, and G. P. Agrawal, "Impact of polarization-mode dispersion and polarization-dependent loss on fiber-optic parametric amplifiers," accepted for publication in J. Lightwave Technol.

Q. Lin, F. Yaman, and G. P. Agrawal, "Raman-induced polarization-dependent gain in parametric amplifiers pumped with orthogonally polarized lasers," IEEE Photon. Technol. Lett. **18**, 397 (2006).

Q. Lin, F. Yaman, and G. P. Agrawal, "Photon-pair generation by four-wave mixing inside optical fibers," Opt. Lett. **31**, 1286 (2006).

A. Sennaroglu, U. Demirbas, S. Ozharar, and F. Yaman, "Accurate determination of saturation parameters for $Cr4^{+}$-doped solid-state saturable absorbers," J. Opt. Soc. Am. B **23**, 241 (2006).

F. Yaman, Q. Lin, S. Radic, and G. P. Agrawal, "Impact of pump-phase modulation on dual-pump fiber-optic parametric amplifiers and wavelength convertors," IEEE Photon. Technol. Lett. **17**, 2053 (2005).

F. Yaman, Q. Lin, S. Radic, and G. P. Agrawal "Pump noise transfer in dual-pump fiber-optic parametric amplifiers: walk-off effects," Opt. Lett. **30**, 1048 (2005).

F. Yaman, Q. Lin, S. Radic, and G. P. Agrawal, "Impact of dispersion fluctuations on dual-pump fiber-optic parametric amplifiers," IEEE Photonic Technol. Lett. **16**, 1292 (2004).

F. Yaman, Q. Lin, and G. P. Agrawal, "Effects of polarization mode dispersion in dual-pump fiber-optic parametric amplifiers," IEEE Photon. Technol. Lett. **16**, 431 (2004).

A. Levent, S. G. Rajeev, F. Yaman, and G. P. Agrawal, "Nonlinear theory of polarization-mode dispersion for fiber solitons," Phys. Rev. Lett. **90**, 013902 (2003).

Book Chapters

F. Yaman, Q. Lin, and G. P. Agrawal, "Fiber-optic parametric amplifiers for lightwave systems," *Guided Wave Optical Components and Devices*, B. P. Pal Ed. (Academic Press, San Diego, CA, 2005), Chap. 7, pp. 101–117.

Presentations

F. Yaman, Q. Lin, and G. P. Agrawal, "A novel design for polarization-independent single-pump fiber-optic parametric amplifiers," in *Proc. Conf. on Lasers and Electro-Optics (CLEO) 2006*, Long Beach, CA, Paper JWB59.

F. Yaman, Q. Lin, S. Radic, and G. P. Agrawal, "Impact of pump-phase modulation on fiber-optic parametric amplifiers and wavelength converters," in *Proc. Conf. on Lasers and Electro-Optics (CLEO) 2005*, Baltimore, MD, Paper CTuJ6.

Q. Lin, F. Yaman, S. Radic, and G. P. Agrawal, "Fundamental noise limits in dual-pump fiber-optic parametric amplifiers and wavelength converters," in *Proc. Conf. on Lasers and Electro-Optics (CLEO) 2005*, Baltimore, MD, Paper CTuT4.

F. Yaman, Q. Lin, S. Radic, and G. P. Agrawal, "Impact of pump-phase modulation on the performance of dual-pump fiber-optic parametric amplifiers," in *Proc. Conf. Optical Fiber Communications (OFC) 2005*, Anaheim, CA, Paper OWN3.

F. Yaman, Q. Lin, and G. P. Agrawal, "Impact of polarization mode dispersion on dual-pump fiber optic parametric amplifiers," in *Proc. Conf. Nonlinear Guided Waves (NLGW) 2004*, Toronto, Paper MC31.

Q. Lin, F. Yaman, and G. P. Agrawal, "Impact of randomly varying fiber dispersion on dual-pump fiber optic parametric amplifiers," in *Proc. Conf. Nonlinear Guided Waves (NLGW) 2004*, Toronto, MC36.

Acknowledgements

I would like to express my gratitude to all those who gave me the opportunity to complete this thesis. First and foremost, I would like to thank my advisor, Professor Govind P. Agrawal. He not only taught me how to do scientific research, he also taught me how to think coherently and write coherently. I am also grateful to him for leading me into the exciting field of nonlinear fiber optics.

I am grateful to Professor Stojan Radic for his valuable discussions and suggestions, as well as providing the point of view of an experimentalist. I would like to thank Professor Sarada G. Rajeev for helping me see the concept of soliton propagation in fibers from a whole new perspective. I am grateful to Professor John C. Howell for letting me use his laboratory equipment.

Among my colleagues, I am particularly grateful to Qiang Lin for his constant contributions to my work, through passionate and fruitful discussions. He not only helped me develop a sound physical intuition about nonlinear processes in fibers but he also helped me find my way through the complicated mathematics of polarization-mode dispersion and stochastic processes. I would like to thank Nick Usechak for the stimulating discussions about mode-locked lasers and pulse characterization. I am grateful to him for answering my questions about laboratory equipment. I thank Dr. Ekaterina Poutrina and Dr. Jayanthi Santhanam for helping me have a better understanding of fiber communication systems. I am grateful to Dr. Levent Akant for introducing to me the exciting mathematical tools that were so helpful in understanding soliton propagation in fibers. I thank Irfan Ali Khan for helping me in Professor Howell's laboratory.

Abstract

Fiber-optic parametric amplifiers (FOPAs) can be used in lightwave systems for several signal-processing applications including optical amplification, phase conjugation, and wavelength conversion. In principle, FOPAs can provide high gain uniform over a wide wavelength range ($>$ 100 nm). What is more, FOPAs add little noise to the amplified signal. FOPAs can have noise figure as low as 0 dB when operated in the phase-sensitive mode and 3 dB in the phase insensitive mode. However, in practice, these advantages of FOPAs are compromised. In this work, I investigate several factors that limit the performance of FOPAs, and propose practical schemes to minimize those limitations.

FOPAs can provide a relatively large gain bandwidth because the gain spectrum of FOPAs is not determined by material resonances but by the phase-matching condition. For the same reason, FOPAs are very sensitive to perturbations stemming from fiber irregularities. One such irregularity is that fiber dispersion varies randomly along the fiber length. My numerical modeling showed that, because of such variations, FOPA gain spectrum cannot maintain its flatness and also that FOPA gain profile changes from one fiber to the other. Using stochastic methods, an analytic theory is developed that can predict an "average gain spectrum." This analytic theory can be used to show that flatness of FOPA gain is recovered at the expense of reducing the gain bandwidth.

Another fiber irregularity that affects FOPA gain spectrum is the residual birefringence. During the fiber-drawing process, the cross section of fiber core inevitably deviates from perfect circular symmetry. As a result, all non-polarization maintaining fibers exhibit residual birefringence. Both the magnitude of birefringence and the direction of

its principal axis vary along the fiber length as well as in time. Because of residual birefringence, state of polarizations of the propagating fields change randomly also. Since the underlying four-wave mixing (FWM) process depends on the state of polarizations of the interacting fields, FOPA gain profile cannot maintain its flatness, and changes in time. The impact of residual birefringence on dual-pump FOPAs are investigated by means of numerical simulations. It is shown that residual birefringence also causes a trade off between flatness of FOPA gain spectrum and FOPA gain bandwidth. The FOPA gain bandwidth required to maintain a flat gain profile is determined.

FOPAs can be used for all-optical signal processing applications since the underlying FWM process responds almost instantaneously. However, the ultrashort response time of FWM makes FOPAs susceptible to pump noise. This becomes a limitation on the noise properties of FOPAs. I investigated the impact of pump noise on the amplified signal in the context of intensity noise transfer. It is shown that the group-velocity difference between the signal and pumps play an important role and reduces the transfer of intensity noise from the pump to the signal.

Another limitation of FOPAs is that, since the efficiency of FWM process depends on polarization states of the interacting fields, FOPA gain becomes sensitive to input polarization of the signal. There are several schemes that have been proposed to eliminate polarization dependence of FOPA gain. However, in the case of single-pump FOPAs the existing methods are cumbersome to implement. In this work, I propose a relatively simple way to achieve polarization-insensitive gain by using a highly birefringent fiber.

Table of Contents

List of Tables

List of Figures

1 Introduction

Fiber-optic parametric amplifiers (FOPAs) employ the nonlinear phenomenon of four-wave mixing (FWM) to transfer energy from one or two strong pump fields to weak signal fields. FWM is a parametric process stemming from the third-order nonlinear response of materials [1]–[3]. The first experiment that demonstrated FWM in fiber dates back to 1974 [4]. Since then, FOPAs have proved to be a versatile tool for important applications [3], [5]. Among these applications are periodic signal amplification for communication systems [6], [7], broadband wavelength conversion [8]–[12], phase conjugation [13]–[17], phase-sensitive amplification [18]–[20], ultrafast optical sampling [21], all-optical time-division demultiplexing [22]–[24], optical switching [25], and entangled photon-pair generation [26].

1.1 Historical Review of Previous Work

Early work on FWM in fibers was limited because of the lack of good-quality fibers and pump sources. Fibers were attractive as a nonlinear medium not because of their high nonlinearity but because they can increase the nonlinear interaction length by confining the optical fields to a tight area and guiding them in the same spatial mode over long distances [3]. In principle, the nonlinear interaction length can be as large as the fiber length. However, in early experiments the nonlinear interaction length was limited

because fibers had large dispersion, high losses, and also because tunable, powerful, continuous-wave (CW) lasers were not readily available in the wavelength region of interest [4], [27].

Fast growth of the field of fiber-optic communications in the eighties and nineties provided the technology that was needed to make the FOPAs practical. First came the telecommunication fibers having low losses and low dispersion in the wavelength region near 1.3 and 1.5 μm, [28], [29]. The second big leap was the introduction of erbium-doped fiber amplifiers [30] and high-quality, tunable semiconductor lasers capable of providing required high power levels [22], [31]. The final step was the introduction of highly nonlinear fibers and the so-called micro-structured fibers [33], [34]. These fibers can increase the effective fiber nonlinearity by a factor of more than 100. Moreover the dispersive properties of microstructured fibers can be tailored easily, providing an additional flexibility in designing FOPAs.

Advances in fiber-optic communication systems provided FOPAs not only with the technology that was essential but also with the motivation to make better FOPAs. Modern optical communication systems require not only signal amplification periodically but also devices that are capable of ultrafast, all-optical, signal processing [28]. FOPAs are attracting considerable attention because they can provide broadband amplification which can cover the entire telecommunication window, and thus, replace erbium-doped fiber amplifiers used commonly for signal amplification [5]–[19]. FOPAs are also an ideal candidate for ultrafast, all-optical, signal processing because of an instantaneous electronic response of the silica nonlinearity responsible for FWM in optical fibers. Moreover, amplification provided by FOPAs is accompanied with relatively low noise, allowing operation close to the quantum limit [18]–[20].

1.2 Thesis Objective

The objective of this thesis is to develop a comprehensive theory of FWM that takes into account the vectorial nature of FWM process, which can be applied to both single and dual-pump FOPAs. This theory is then used to study the impact of fiber imperfections on parametric amplification. For instance, the effect of randomly varying zero-dispersion wavelength of the fiber on the FOPA gain band-width and gain spectrum uniformity is investigated using a stochastic approach. The full vectorial nature of the theory developed for FWM allows for an understanding of the effects of residual birefringence on the FOPA gain.

The comprehensive theory of FWM is then used to understand the impact of pump noise on the amplified signal and idler fields. The theory points out the potential mechanisms through which pump noise can be transferred to the signal. In particular, the effect of group-velocity difference between the pumps and the signal is taken into account when calculating the degree of signal degradation. Since these equations can describe the vectorial nature of FWM process, the impact of variations in the polarization state of the pumps on the signal gain can also be calculated.

Finally, a simple scheme for making polarization-insensitive single-pump FOPA is proposed through a detailed analysis of FWM in highly-birefringent fibers.

1.3 Thesis Organization

Chapter 2 shows a derivation of the vector nonlinear Schrödinger equation which describes nonlinear evolution of optical fields in fibers. From the vector NLS equation, vectorial FWM equations are derived. These equations are used in later chapters whenever states of polarization of the fields involved in the FWM process have to be taken into account. At the end of this Chapter, the vectorial FWM equations are reduced to a simple scalar form to discuss a few basic properties of the FWM process.

In Chapter 3, basic aspects of parametric amplification are discussed in terms of the role of phase matching, the schemes used for satisfying the phase-matching condition in single- and dual-pump FOPAs, and the dependence of parametric gain on the states of polarization of the interacting fields. Examples of experiments that used FOPAs for several different applications are described and their performances are summarized.

Chapter 4 investigates the impact of fiber imperfections on the FOPA gain bandwidth and flatness of the gain spectrum. Two common imperfections of most fibers are random variations in the dispersion along the fiber length, and polarization-mode dispersion induced by randomly varying residual birefringence.

Chapter 5 shows that the noise associated with two pumps is a major source of signal degradation. It is shown that preparation of FOPA pumps is usually done in multiple stages during which pumps can be distorted through three different mechanisms. These mechanisms are introduced and their impacts on the amplified signal and idler are discussed separately. For each degradation mechanism a simple solution is provided.

Chapter 6 discusses FWM in a highly birefringent fiber. It is proposed in this Chapter that a highly birefringent fiber can be used to achieve polarization-independent gain in single-pumped FOPAs. This scheme is superior to the existing techniques because of its simplicity.

2 Theoretical Framework

The FWM process originates from the nonlinear response of bound electrons to the intense optical waves propagating inside nonlinear media such as silica fibers. When two intense pump waves at frequencies ω_1 and ω_2 copropagate inside an optical fiber, they can force the bound electrons to oscillate almost instantaneously at any frequency stemming from the mixing of these waves. Even though the potential provided by silica molecules confines electrons to their original atom, electrons respond to the applied electromagnetic field by emitting secondary waves not only at the original frequencies ω_1 and ω_2 (linear response), but also at two new frequencies denoted as ω_3 and ω_4 (third-order nonlinear response).

2.1 Basic Properties of FWM

Physically, two photons at the original frequencies are scattered elastically into two new photons at frequencies ω_3 and ω_4 as shown in Fig. 2.1.

The total energy and momentum of the original two photons are conserved during FWM. Noting that photon energy and momentum are $\hbar\omega$ and $\hbar\beta$, respectively, for an optical field of frequency ω propagating with the propagation constant β, the conser-

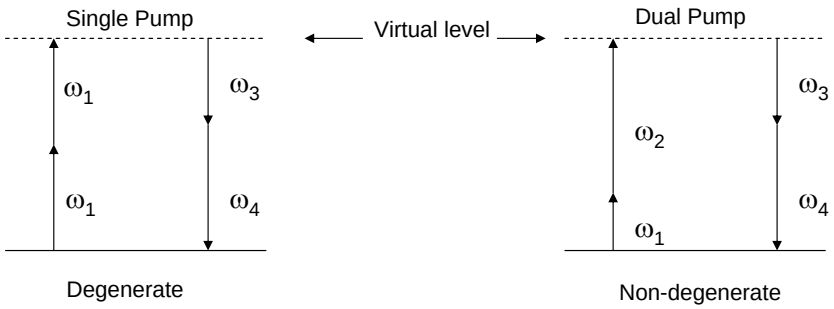

Figure 2.1: Degenerate and nondedenerate FWM process depicted on an energy level diagram.

vation relations take the form:

$$\omega_1 + \omega_2 = \omega_3 + \omega_4, \tag{2.1}$$

$$\beta(\omega_1) + \beta(\omega_2) = \beta(\omega_3) + \beta(\omega_4), \tag{2.2}$$

Only the magnitude of wave vectors appears in Eq. (2.1), because all four waves propagate along the same direction in single-mode fibers. Since $\beta(\omega_j)$ governs the phase shift experienced by the jth wave, Eq. (2.2) is also referred to as the phase-matching condition [2].

A question that must be answered is what determines the frequencies ω_3 and ω_4 during the FWM process. If only the pump beams are incident on an optical fiber, the new waves grow from noise and their frequencies are determined by the phase-matching condition through spontaneous FWM. In practice, the efficiency of the FWM process is enhanced by seeding it. Seeding is accomplished by launching a signal wave at the frequency ω_3. The probability of creating photons at the frequency ω_4 depends on how many photons at ω_3 already exist inside the fiber. As a result, the FWM process is stimulated, and new photons at ω_3 and ω_4 are created with an exponential growth rate, provided the phase-matching condition is nearly satisfied. It is common to refer to the fourth wave at the frequency ω_4 as the *idler wave*, following the terminology used in the microwave literature. It is not obligatory to launch two separate pump beams for FWM to occur. The same process can occur even when the two pump photons have the

same frequency (degenerate FWM). The general case of two independent pump beams is called nondegenerate FWM.

2.2 Maxwell's and Helmholtz's Equations

So far, the FWM process is discussed without referring to the medium in which it takes place. To describe FWM in a fiber correctly, the guiding nature of the fiber has to be taken into account. Propagation of intense optical fields in fibers is described by the nonlinear Schödinger equation. Using this equation, the nonlinear evolution of the four fields involved in FWM (as well as other nonlinear processes) can be studied. Starting point for derivation of the nonlinear Schödinger equation is the set of Maxwell equations:

$$\nabla \cdot \boldsymbol{D} = \rho, \tag{2.3}$$

$$\nabla \cdot \boldsymbol{B} = 0, \tag{2.4}$$

$$\nabla \times \boldsymbol{E} = -\frac{\partial \boldsymbol{B}}{\partial t}, \tag{2.5}$$

$$\nabla \times \boldsymbol{H} = \boldsymbol{J} + \frac{\partial \boldsymbol{D}}{\partial t}, \tag{2.6}$$

where $\boldsymbol{D}$ and $\boldsymbol{B}$ are electric and magnetic flux densities, $\boldsymbol{E}$ and $\boldsymbol{H}$ are electric and magnetic field vectors, ρ is the charge density, and $\boldsymbol{J}$ is the current density vector.

The electric and magnetic flux densities, $\boldsymbol{D}$ and $\boldsymbol{B}$, are related to the electric and magnetic field vectors, respectively, as follows:

$$\boldsymbol{D} = \varepsilon_0 \boldsymbol{E} + \boldsymbol{P}, \tag{2.7}$$

$$\boldsymbol{B} = \mu_0 \boldsymbol{H} + \boldsymbol{M}, \tag{2.8}$$

where ε_0 is the vacuum permittivity and μ_0 is vacuum permeability. The induced electric and magnetic polarizations $\boldsymbol{P}$ and $\boldsymbol{M}$ account for the material response.

The equation that describes the propagation of the electric field can be written in terms of a single, second-order, partial differential equation known as the electromag-

netic wave equation. First, taking the curl of Eq. (2.5) and using Eqs. (2.6) and (2.8) we obtain

$$\nabla \times \nabla \times \boldsymbol{E} = -\frac{\partial(\nabla \times \boldsymbol{B})}{\partial t} = -\mu_0 \varepsilon_0 \frac{\partial^2 \boldsymbol{E}}{\partial t^2} - \mu_0 \frac{\partial^2 \boldsymbol{P}}{\partial t^2} - \mu_0 \frac{\partial \boldsymbol{J}}{\partial t} - \frac{\partial(\nabla \times \boldsymbol{M})}{\partial t}. \quad (2.9)$$

As fibers do not typically contain free charges, ($\rho = 0$ and $\boldsymbol{J} = 0$) and have a non-magnetic nature, the last two terms in Eq. (2.9) can be dropped. Left-hand side of the equation can be simplified through the identity

$$\nabla \times \nabla \times \boldsymbol{E} = \nabla(\nabla \cdot \boldsymbol{E}) - \nabla^2 \boldsymbol{E} = -\nabla^2 \boldsymbol{E}, \quad (2.10)$$

where Eq. (2.3) is used in the last step. With these simplifications Eq. (2.9) becomes

$$\nabla^2 \boldsymbol{E} - \frac{1}{c^2} \frac{\partial^2 \boldsymbol{E}}{\partial t^2} = \frac{\varepsilon_0}{c^2} \frac{\partial^2 \boldsymbol{P}}{\partial t^2}, \quad (2.11)$$

where the definition for the speed of light $c = (\mu_0 \varepsilon_0)^{-\frac{1}{2}}$ is used.

The induced polarization $\boldsymbol{P}$ is typically a complicated function of the electric field. In the case of fibers, the electric field is rarely intense enough to necessitate knowing the exact dependence of $\boldsymbol{P}$ on $\boldsymbol{E}$. Such dependence is usually studied by expanding the induced polarization in a Taylor series as a function of the electric field strength and retaining only those terms that become significant. In fibers, the first nonlinear term that becomes important is the third-order term (because the even-order terms vanish for a medium exhibiting the inversion symmetry). Retaining only the first-and third-order terms, the induced polarization can be separated into a linear and a nonlinear part as

$$\boldsymbol{P} = \boldsymbol{P}_L + \boldsymbol{P}_{NL}. \quad (2.12)$$

The linear and nonlinear parts of the induced polarization can be expressed as

$$\boldsymbol{P}_L(\boldsymbol{r},t) = \varepsilon_0 \int_{-\infty}^{\infty} \boldsymbol{\chi}^{(1)}(t-t') \cdot \boldsymbol{E}(\boldsymbol{r},t')\, dt', \quad (2.13)$$

and

$$\boldsymbol{P}_{NL}(\boldsymbol{r},t) = \varepsilon_0 \iiint_{-\infty}^{t} \boldsymbol{\chi}^{(3)}(t-t_1, t-t_2, t-t_3) \vdots \boldsymbol{E}(\boldsymbol{r},t_1)\boldsymbol{E}(\boldsymbol{r},t_2)\boldsymbol{E}(\boldsymbol{r},t_3)\, dt_1 dt_2 dt_3 \quad (2.14)$$

where $\chi^{(1)}$ and $\chi^{(3)}$ are the first- and third-order susceptibilities representing the response of the material. In general, neither linear nor nonlinear response of the material is instantaneous. The delayed linear response leads to material dispersion as well as intrinsic material loss, and it is also response is responsible for the nonlinear resonant processes such as the Raman and Brillouin scattering. FWM, on the other hand, is a nonresonant nonlinear process that is produced by the instantaneous part of the third-order susceptibility. In designing FOPAs, special care is taken to ensure that contribution of Raman and Brillouin scattering remains small compared to FWM and can be neglected. With this approximation, the nonlinear induced polarization can be written as

$$\boldsymbol{P}_{NL}(\boldsymbol{r},t) = \varepsilon_0 \boldsymbol{\chi}^{(3)} \vdots \boldsymbol{E}(\boldsymbol{r},t)\boldsymbol{E}(\boldsymbol{r},t)\boldsymbol{E}(\boldsymbol{r},t). \tag{2.15}$$

For typical electric field strengths, the contribution of the nonlinear part of induced polarization is much smaller compared to the linear part. This feature allows us to treat the effect of the nonlinear contribution in a perturbative manner. In the first step, the nonlinear part is assumed to vanish, i.e. $\boldsymbol{P}_{NL} \approx 0$. As a result of this simplification Eq. (2.11) reduces to a linear equation and it takes a simpler form in the frequency domain known as Helmholtz Equation :

$$\nabla^2 \tilde{\boldsymbol{E}}(\boldsymbol{r},\omega) + \frac{\varepsilon(\boldsymbol{r},\omega)\omega^2}{c^2}\tilde{\boldsymbol{E}}(\boldsymbol{r},\omega) = 0, \tag{2.16}$$

where, $\tilde{\boldsymbol{E}}(\boldsymbol{r},\omega)$ is the Fourier transform of $\boldsymbol{E}(\boldsymbol{r},t)$ defined through the relation

$$\tilde{\boldsymbol{E}}(\boldsymbol{r},\omega) = \int_{-\infty}^{\infty} \boldsymbol{E}(\boldsymbol{r},t)\exp(i\omega t)\,dt. \tag{2.17}$$

The quantity $\varepsilon(\boldsymbol{r},\omega)$ is known as the dielectric constant of the material and is related to the linear susceptibility as

$$\varepsilon(\boldsymbol{r},\omega) = 1 + \tilde{\boldsymbol{\chi}}^{(1)}(\boldsymbol{r},\omega). \tag{2.18}$$

The real and imaginary parts of dielectric constant can be used to define the refractive index $n(\omega)$ and absorption coefficient $\alpha(\omega)$ through relation

$$\varepsilon = (n + i\alpha c/2\omega)^2. \tag{2.19}$$

Using Eqs. (2.18) and (2.19), the refractive index and the absorption coefficient can be written approximately as

$$n = 1+\frac{1}{2}\mathrm{Re}[\tilde{\chi}^{(1)}], \tag{2.20}$$

$$\alpha = \frac{\omega}{2c}\mathrm{Im}[\tilde{\chi}^{(1)}]. \tag{2.21}$$

2.3 Modes of Optical Fibers

Because of the cylindrical symmetry of the fiber it is suitable to write Eq. (2.16) as

$$\frac{\partial^2\tilde{\boldsymbol{E}}}{\partial\rho^2}+\frac{1}{\rho}\frac{\partial\tilde{\boldsymbol{E}}}{\partial\rho}+\frac{1}{\rho^2}\frac{\partial^2\tilde{\boldsymbol{E}}}{\partial\phi^2}+\frac{\partial^2\tilde{\boldsymbol{E}}}{\partial z^2}+n^2k_0^2\tilde{\boldsymbol{E}}=0, \tag{2.22}$$

where ρ, ϕ and z are the cylindrical coordinates and $k_0=\omega/c$ is the propagation constant in free space. A similar equation can be obtained for the magnetic field $\tilde{\boldsymbol{H}}$. Since the electric and magnetic fields have to satisfy the Maxwell's equations, only two out of the six components $\tilde{E}_\rho$, $\tilde{E}_\phi$, $\tilde{E}_z$, $\tilde{H}_\rho$, $\tilde{H}_\phi$ and $\tilde{H}_z$ are independent. It is customary to solve for $\tilde{E}_z$ and $\tilde{H}_z$ independently, both of which satisfy Eq. (2.22), and obtain the rest of the field components from these two using the Maxwell's equations.

The Helmhotz equation for the z component of the electric field can be solved using the method of separation of variables. For this purpose a solution of the following form is assumed

$$\tilde{E}_z = F(\rho)\exp(\pm im\phi)\exp(i\beta z). \tag{2.23}$$

Inserting Eq. (2.23) into Eq. (2.22) the following equation is obtained

$$\frac{\partial^2F}{\partial\rho^2}+\frac{1}{\rho}\frac{\partial F}{\partial\rho}-\left(\frac{m^2}{\rho^2}+\beta^2-n^2k_0^2\right)F=0. \tag{2.24}$$

Equation (2.24) has solutions in the form:

$$F(\rho)=\begin{cases} J_m(\eta\rho), & \rho\le a,\\ K_m(\zeta\rho), & \rho\ge a,\end{cases} \tag{2.25}$$

where J_m and K_m are the Bessel and modified Bessel functions, respectively, $\eta = (n_1^2 k_0^2 - \beta^2)^{1/2}$, $\zeta = (\beta^2 - n_2^2 k_0^2)^{1/2}$, a is the radius of the fiber core, and n_1 and n_2 are the refractive indices of the core and the cladding of the fiber, respectively. Solution for $\tilde{H}_z$ can be found in the same manner. Once the z components of the fields are found, rest of the field components can be determined from Maxwell's equations. Since fibers do not have any free charges across the boundary between the core and the cladding, the tangential components of the fields have to be continuous. Imposing this condition on the solution obtained for the fields results in the following eigenvalue equation involving the propagation constant β:

$$\left[\frac{J_m'(\eta a)}{\eta J_m(\eta a)} + \frac{K_m'(\zeta a)}{\zeta K_m(\zeta a)}\right]\left[\frac{J_m'(\eta a)}{\eta J_m(\eta a)} + \frac{n_2^2}{n_1^2}\frac{K_m'(\zeta a)}{\zeta K_m(\zeta a)}\right] = \left[\frac{m\beta k_0(n_1^2 - n_2^2)}{a n_1 \zeta^2 \eta^2}\right]^2. \quad (2.26)$$

Depending on the fiber parameters a, n_1 and n_2, in general, Eq. (2.26) has multiple solutions for every integer value of m. These solutions for the propagation constant are denoted as β_{nm} and the corresponding field distributions are called HE_{nm} or EH_{nm}, depending on whether the axial component of the electric field or the magnetic field dominates. Each of these solutions correspond to a transverse mode supported by the fiber.

According to Eq. (2.25), the electric field is not confined entirely in the fiber core but experiences the refractive indices of both the core and the cladding. Therefore, it is useful to introduce an effective refractive index defined as $\bar{n} = \beta/k_0$. Its physical significance can be understood from the fact that, for a given fiber design, a transverse mode of the fiber is a guided mode as long as its effective index satisfies the condition $n_2 < \bar{n} < n_1$. Clearly, if the effective index is smaller than the cladding index, the field cannot be guided by the fiber since it cannot experience total internal reflection. Indeed, Eq. (2.25) shows that when $\bar{n} < n_2$, ζ becomes imaginary, therefore, the portion of the field in the cladding does not decay anymore. This condition can be used to design single-mode fibers that support only the fundamental mode. Single-mode fibers are the

most commonly used fibers since they have better spatial beam quality and they do not suffer from intermodal dispersion.

The fundamental mode of fibers is the HE_{11} mode. This mode is dominated by the transverse components, and its axial component can be neglected. Even though fibers can be designed to guide only the fundamental mode, in the transverse plane, the electric field can be decomposed into two orthogonally polarized components. Therefore, even single-mode fibers support two distinct modes known as the polarization modes. If the electric field is polarized along the x–axis, the fundamental mode takes the following form

$$\tilde{E}_x = \begin{cases} E_0[J_0(\eta\rho)/J_0(\eta a)]\exp(i\beta(\omega)z), & \rho \leq a, \\ E_0\,[K_0(\zeta\rho)/K_0(\zeta a)]\exp(i\beta(\omega)z), & \rho \geq a, \end{cases} \tag{2.27}$$

where E_0 is the field amplitude.

In a fiber with perfect cylindrical symmetry, the two polarization modes are degenerate in the sense that they have the same transverse profile as well as the same propagation constant. If this symmetry is broken, either on purpose or due to manufacturing defects, the two polarization modes cease to be degenerate. In general, deviations from cylindrical symmetry are small enough that they do not affect the transverse-mode distribution but change the propagation constants of the two polarization components slightly. In this case the fiber is said to exhibit birefringence. It is useful to introduce a quantity called the degree of birefringence $B = |\bar{n}_x - \bar{n}_y|$, where $\bar{n}_x$ and $\bar{n}_y$ are the effective refractive indices experienced by the polarization components of the field along x and y axes, respectively. In practice, it is difficult to reduce the degree of birefringence below 10^{-7} because of an imperfect circular shape, and the stress and strain induced during the fiber-drawing process. What is more, since such residual birefringence cannot be controlled, the orientation of the slow and fast axes vary along the fiber length.

2.4 Third-order Nonlinear Response

The next step is to incorporate the effect of third-order nonlinearity into Eq. (2.11). To do that, a few approximations and simplifications are needed. The first of these simplifications comes from the assumption that the field is quasi-monochromatic. This assumption, also known as the slowly-varying envelope approximation, is valid whenever the spectral spread $\Delta\omega$ of the field is much smaller than the central frequency ω_0 of the spectrum. This approximation remains valid until the width of the field envelope reduces to below a few optical cycles. The second simplification is due to the fact that nonlinear induced polarization is much smaller than the linear induced polarization and it does not affect the transverse field distribution to the first order. Finally, it is assumed that the dipole approximation is valid and the material response is local. With these assumptions in mind, the electric field can be written as

$$\boldsymbol{E}(\boldsymbol{r},t) = \frac{1}{2}[\hat{x}E_x(\boldsymbol{r},t) + \hat{y}E_y(\boldsymbol{r},t)]\exp(-i\omega_0 t) + \text{c.c.}, \tag{2.28}$$

where $\hat{x}$ and $\hat{y}$ are unit vectors, E_x and E_y are the two polarization components of the slowly varying envelope in the linear basis. The optical field is propagating along the z axis with an unchanging transverse profile.

The material response of the fiber can also be separated into its slowly varying envelope and its rapidly oscillating carrier frequency in a similar way as

$$\begin{aligned}\boldsymbol{P}(\boldsymbol{r},t) = \frac{1}{2}\{\hat{x}[P_{Lx}(\boldsymbol{r},t) + P_{NLx}(\boldsymbol{r},t)] + \hat{y}[P_{Ly}(\boldsymbol{r},t) + P_{NLy}(\boldsymbol{r},t)]\}\exp(-i\omega_0 t) \\ + \text{c.c.}\end{aligned} \tag{2.29}$$

Using Eqs. (2.13), (2.15), (2.28) and (2.29), the expression for the slowly varying envelope of the induced polarization becomes

$$P_{Li}(\boldsymbol{r},t) = \varepsilon_0 \int_{-\infty}^{\infty} \sum_j \chi_{ij}^{(1)}(t-t')E_j(\boldsymbol{r},t')\exp[i\omega_0(t-t')]\,dt', \tag{2.30}$$

$$P_{NLi}(\boldsymbol{r},t) = \varepsilon_0 \frac{3}{4} \sum_{j,k,l} \chi_{ijkl}^{(3)} E_j(r,t)E_k(r,t)E_l(r,t)^*, \tag{2.31}$$

where i, j, k, and l stand for x or y. In deriving Eq. (2.31), the induced nonlinear polarization at the third harmonic of the electric field is ignored since this process rarely satisfies the phase-matching condition to have an appreciable contribution. The factor of three in the expression is the number of ways the three fields can mix up to create a response at the carrier frequency.

In an isotropic medium such as an optical fiber, the elements of the nonlinear susceptibility tensor cannot be completely independent but must satisfy several relations imposed by the material symmetry. As a result, the number of independent elements of $\chi^{(3)}$ reduce to three and they satisfy the following relation

$$\chi^{(3)}_{ijkl} = \chi^{(3)}_{xxyy}\delta_{ij}\delta_{kl} + \chi^{(3)}_{xyxy}\delta_{ik}\delta_{jl} + \chi^{(3)}_{xyyx}\delta_{il}\delta_{jk}, \tag{2.32}$$

where δ_{ij} is the Kronecker delta function. Using Eq. (2.32), nonlinear part of the induced polarization can be written as

$$P_{NLi} = \frac{3\varepsilon_0}{4}\sum_j \left(\chi^{(3)}_{xxyy}E_iE_jE_j^* + \chi^{(3)}_{xyxy}E_jE_iE_j^* + \chi^{(3)}_{xyyx}E_jE_jE_i^*\right). \tag{2.33}$$

The relative contributions of the three independent terms are determined by the physical origin of the nonlinear process. In fibers and other materials where the nonlinearity is mainly of electronic origin, all of the three independent terms contribute equally. Finally, using Eq. (2.32) they can be expressed in terms of the single parameter $\chi^{(3)}_{xxxx}$

$$\frac{1}{3}\chi^{(3)}_{xxxx} = \chi^{(3)}_{xxyy} = \chi^{(3)}_{xyxy} = \chi^{(3)}_{xyyx}. \tag{2.34}$$

Equation (2.33) can be simplified even further using Eq. (2.34) to become

$$P_{NLi} = \frac{\varepsilon_0\chi^{(3)}_{xxxx}}{4}\sum_j \left(E_iE_jE_j^* + E_jE_iE_j^* + E_jE_jE_i^*\right). \tag{2.35}$$

The explicit forms of nonlinear induced polarization along the x- and y-axis becomes

$$P_{NLx} = \frac{3\,\varepsilon_0\chi^{(3)}_{xxxx}}{4}\left[\left(|E_x|^2 + \frac{2}{3}|E_y|^2\right)E_x + \frac{1}{3}E_x^*E_y^2\right], \tag{2.36}$$

$$P_{NLy} = \frac{3\,\varepsilon_0\chi^{(3)}_{xxxx}}{4}\left[\left(|E_y|^2 + \frac{2}{3}|E_x|^2\right)E_y + \frac{1}{3}E_y^*E_x^2\right]. \tag{2.37}$$

The equations governing the evolution and interaction of the two polarization components of the field can be written in a compact form in the Jones space. In this notation, complex valued electric field components are represented by the elements of a vector as shown in the following example:

$$|E(\boldsymbol{r},t)\rangle = \begin{pmatrix} E_x(\boldsymbol{r},t) \\ E_y(\boldsymbol{r},t) \end{pmatrix}, \qquad |P(\boldsymbol{r},t)\rangle = \begin{pmatrix} P_x(\boldsymbol{r},t) \\ P_y(\boldsymbol{r},t) \end{pmatrix}. \tag{2.38}$$

With this notation, Eqs. (2.36) and (2.37) can be written in a simpler form as

$$|P_{NL}\rangle = \varepsilon_0 \overleftrightarrow{\varepsilon}_{NL} |E\rangle, \qquad \overleftrightarrow{\varepsilon}_{NL} = \frac{3\chi^{(3)}_{xxxx}}{4} \begin{pmatrix} |E_x|^2 + \frac{2}{3}|E_y|^2 & \frac{1}{3}E_x^* E_y \\ \frac{1}{3}E_y^* E_x & |E_y|^2 + \frac{2}{3}|E_x|^2 \end{pmatrix}. \tag{2.39}$$

Complex valued 2×2 matrices such as the one shown in Eq. (2.39) can also be represented in a simpler form by introducing the Pauli matrices defined as

$$\boldsymbol{\sigma}_1 = \begin{pmatrix} 1 & 0 \\ 0 & -1 \end{pmatrix} \qquad \boldsymbol{\sigma}_2 = \begin{pmatrix} 0 & 1 \\ 1 & 0 \end{pmatrix} \qquad \boldsymbol{\sigma}_3 = \begin{pmatrix} 0 & -i \\ i & 0 \end{pmatrix}. \tag{2.40}$$

Together with the identity matrix $\boldsymbol{\sigma}_0$ these matrices form a complete set in the sense that any 2×2 matrix can be written as a linear combination of them, for example

$$\overleftrightarrow{\varepsilon}_{NL} = \frac{3\chi^{(3)}_{xxxx}}{4} \left[\frac{5}{6}\langle E|E\rangle \boldsymbol{\sigma}_0 + \frac{1}{6}\langle E|\boldsymbol{\sigma}_1|E\rangle \boldsymbol{\sigma}_1 + \frac{1}{6}\langle E|\boldsymbol{\sigma}_2|E\rangle \boldsymbol{\sigma}_2 - \frac{1}{6}\langle E|\boldsymbol{\sigma}_3|E\rangle \boldsymbol{\sigma}_3 \right]. \tag{2.41}$$

To make the notation more compact, one can show that $|P_{NL}\rangle = (3\varepsilon_0 \chi^{(3)}_{xxxx}/4)\boldsymbol{\Gamma}|E(\boldsymbol{r},t)\rangle$ where

$$\boldsymbol{\Gamma} = \langle E|E\rangle \boldsymbol{\sigma}_0 - \frac{1}{3}\langle E|\boldsymbol{\sigma}_3|E\rangle \boldsymbol{\sigma}_3. \tag{2.42}$$

Written this way, the two contributions to the nonlinear response of the material can be identified. The first term on the left-hand side of Eq. (2.42), depends only on the total power of the field and it affects both polarization components of the field equally. Therefore contribution of this term is said to be isotropic. The second term is a traceless matrix and it leads to what is known as the nonlinear birefringence. When the electric field is linearly or circularly polarized, the second term in Eq. (2.42) vanishes and it

does not experience nonlinear birefringence. In contrast, any elliptically polarized field experiences an effective birefringence and propagates in a way that transfers the energy back and forth between the two polarization components.

2.5 Vectorial NLS Equation

To proceed further, it is useful to transform Eq. (2.11) into the Fourier domain using the following definition for the Fourier transform

$$|\tilde{E}(\boldsymbol{r},\omega-\omega_0)\rangle = \int_{-\infty}^{\infty} |E(\boldsymbol{r},t)\rangle \exp[i(\omega-\omega_0)t]\,dt. \tag{2.43}$$

Taking the Fourier transform of the nonlinear induced polarization $|P_{NL}\rangle$ would result in complicated convolutions. However, based on the fact that the nonlinear contribution of the material response is only perturbative in nature, and also under the slowly varying envelope approximation, the nonlinear terms such as $\langle E|E\rangle$ and $\langle E|\boldsymbol{\sigma}_3|E\rangle$ appearing in the expression of $|P_{NL}\rangle$ can be treated as constants. Using Eqs. (2.13), (2.39) and (2.42) together with the slowly varying envelope approximation, Eq. (2.11) can be written in the Fourier domain as

$$\nabla^2|\tilde{E}\rangle + \overleftrightarrow{\varepsilon}(\omega)k_0^2|\tilde{E}\rangle = 0, \tag{2.44}$$

where $k_0 = \omega/c$ and $\overleftrightarrow{\varepsilon}(\omega) = \overleftrightarrow{\varepsilon}_L(\omega) + \overleftrightarrow{\varepsilon}_{NL}$ is the dielectric tensor incorporating both the linear and nonlinear material response, and $\overleftrightarrow{\varepsilon}_{NL}$ is given in Eq. (2.39). The linear part of the dielectric tensor is defined as

$$\overleftrightarrow{\varepsilon}_L(\omega) = \varepsilon_{L0}(\omega)\boldsymbol{\sigma}_0 + \vec{\varepsilon}_L(\omega)\cdot\vec{\boldsymbol{\sigma}}, \tag{2.45}$$

where $\varepsilon_{L0} = 1 + (\tilde{\chi}_{xx}^{(1)} + \tilde{\chi}_{yy}^{(1)})/2$ is the isotropic contribution and $\vec{\varepsilon}_L(\omega)\cdot\vec{\boldsymbol{\sigma}} \equiv \varepsilon_{L1}\boldsymbol{\sigma}_1 + \varepsilon_{L2}\boldsymbol{\sigma}_2 + \varepsilon_{L3}\boldsymbol{\sigma}_3$ is the anisotropic contribution to the dielectric constant with $\overleftrightarrow{\varepsilon}_{L1} = (\tilde{\chi}_{xx}^{(1)} - \tilde{\chi}_{yy}^{(1)})/2$, $\overleftrightarrow{\varepsilon}_{L2} = (\tilde{\chi}_{xy}^{(1)} + \tilde{\chi}_{yx}^{(1)})/2$ and $\overleftrightarrow{\varepsilon}_{L3} = i(\tilde{\chi}_{xy}^{(1)} - \tilde{\chi}_{yx}^{(1)})/2$.

Equation (2.44) can be solved using the method of separation of variables and assuming that the electric field is of the form

$$|\tilde{E}(\boldsymbol{r},\omega-\omega_0)\rangle = F(\rho)|\tilde{A}(z,\omega-\omega_0))\rangle \exp(\pm im\phi)\exp(i\beta_0 z), \tag{2.46}$$

where ρ, ϕ and z are the cylindrical coordinates, z being the propagation direction along the fiber, and β_0 is the wave number of the field at the carrier wavelength to be determined later from the boundary conditions. The transverse profile of the field distribution is assumed to be the same for both polarization components since the anisotropic contribution to the dielectric tensor is typically orders of magnitude smaller compared to the isotropic part. Inserting Eq. (2.46) into Eq. (2.44) the following equations are obtained

$$\left(\frac{\partial^2 F}{\partial \rho^2}+\frac{1}{\rho}\frac{\partial F}{\partial \rho}-\frac{m^2 F}{\rho^2}\right)\boldsymbol{\sigma_0}+\left(\overleftrightarrow{\beta}^2-\overleftrightarrow{\varepsilon}(\omega)k_0^2\right)F=0, \tag{2.47}$$

$$\frac{\partial^2|\tilde{A}\rangle}{\partial z^2}+2i\beta_0\frac{\partial|\tilde{A}\rangle}{\partial z}+(\overleftrightarrow{\beta}^2-\beta_0^2)|\tilde{A}\rangle=0. \tag{2.48}$$

The dielectric constant in Eq. (2.47) can be approximated in terms of the refractive index as follows

$$\overleftrightarrow{\varepsilon}=\varepsilon_{L0}(\omega)\boldsymbol{\sigma}_0+\vec{\varepsilon}_L(\omega)\cdot\vec{\boldsymbol{\sigma}}+\overleftrightarrow{\varepsilon}_{NL}\approx(n^2+in\alpha/k_0)\boldsymbol{\sigma_0}+2n\vec{\delta}_n\cdot\vec{\boldsymbol{\sigma}}+2n\overleftrightarrow{n}_2, \tag{2.49}$$

where n is the average of the refractive indices along the fast and slow axes and $\overleftrightarrow{n}_2$ is the nonlinear index. The Stokes vector $\vec{\delta}_n$ points in the direction of the fast birefringence axis and its magnitude gives the refractive index difference between the slow and fast axes. These three quantities are related to different contributions of the dielectric constants as follows

$$n^2(\omega)+\frac{in(\omega)\alpha}{k_0}=\varepsilon_{L0}(\omega),\qquad \vec{\delta}_n=\frac{\vec{\varepsilon}_L(\omega)}{2n},\qquad \overleftrightarrow{n}_2=\frac{\overleftrightarrow{\varepsilon}_{NL}}{2n}. \tag{2.50}$$

In the absence of fiber birefringence and the nonlinear contribution to the dielectric constant Eq. (2.47) reduces to Eq. (2.24), which has a solution given by Eq. (2.27). Since the nonlinear and anisotropic terms are small, their effect can be studied by perturbation. As a first-order approximation, the nonlinear and anisotropic terms do not affect the transverse field distribution but only modify the propagation constant slightly as follows:

$$\overleftrightarrow{\beta}=\beta(\omega)\boldsymbol{\sigma}_0+\overleftrightarrow{\delta\beta}. \tag{2.51}$$

The change in the propagation constant due to the fiber nonlinearity and birefringence can be calculated by inserting the zeroth-order solution given by Eq. (2.25) into Eq. (2.47), and ignoring terms that are higher than first order. By requiring that $\overleftrightarrow{\delta\beta}$ satisfies the equation in the first order gives

$$\overleftrightarrow{\delta\beta} = \frac{nk_0^2}{\beta(\omega)}\left[\frac{i\alpha}{2k_0}\boldsymbol{\sigma}_0 + \vec{\delta}_n(\omega)\cdot\vec{\boldsymbol{\sigma}} + \frac{\iint_\infty^\infty |F(x,y)|^2 \overleftrightarrow{n}_2(x,y)dxdy}{\iint_\infty^\infty |F(x,y)|^2 dxdy}\right]. \tag{2.52}$$

Once the propagation constant is determined, equation describing the evolution of the field along the fiber can be found from Eq. (2.48) in the form

$$\frac{\partial|\tilde{A}\rangle}{\partial z} = i\Big\{[\beta(\omega)-\beta_0]\boldsymbol{\sigma}_0 + \overleftrightarrow{\delta\beta}\Big\}|\tilde{A}\rangle, \tag{2.53}$$

where the second derivative with respect to z is neglected on the basis of slowly varying envelope approximation and $(\overleftrightarrow{\beta}^2 - \beta_0^2\boldsymbol{\sigma}_0)$ is assumed to be approximately equal to $2\beta_0(\overleftrightarrow{\beta} - \beta_0\boldsymbol{\sigma}_0)$.

Equation (2.53) can be inverse-Fourier-transformed to obtain the propagation equation in the time domain. However, the exact frequency dependence of $\beta(\omega)$ and $\overleftrightarrow{\delta\beta}(\omega)$ may be complicated, or may not be fully known. As an approximation, it is customary to expand them in a Taylor series around the carrier frequency and retain only those terms that can contribute significantly for a given spectral width of the field. Using this simplification, the propagation equation in the time domain becomes

$$\begin{aligned}\frac{\partial|A\rangle}{\partial z} = &-\frac{\alpha}{2}|A\rangle + i\vec{b}_0\cdot\vec{\boldsymbol{\sigma}}|A\rangle - \vec{b}_1\cdot\vec{\boldsymbol{\sigma}}\frac{\partial|A\rangle}{\partial t} - \beta_1\frac{\partial|A\rangle}{\partial t} - i\frac{\beta_2}{2}\frac{\partial^2|A\rangle}{\partial t^2}\\ &+ i\gamma\left[\langle A|A\rangle\boldsymbol{\sigma}_0 - \frac{1}{3}\langle A|\boldsymbol{\sigma}_3|A\rangle\boldsymbol{\sigma}_3\right]|A\rangle,\end{aligned} \tag{2.54}$$

where α is the loss coefficient, $\vec{b}_0 = k_0\vec{\delta}_n(\omega_0)$ is the fiber birefringence at the carrier wavelength, $\vec{b}_1 = [\partial(k_0\vec{\delta}_n)/\partial\omega]_{\omega=\omega_0}$ is the polarization-mode dispersion (PMD) vector, β_1 and β_2 are the first and second order terms in the Taylor expansion of propagation constant $\beta(\omega)$ around the carrier frequency, and γ defined as

$$\gamma = \frac{3\chi^{(3)}_{xxxx}k_0}{8nA_{\text{eff}}}, \tag{2.55}$$

where A_{eff} is the effective mode area defined as

$$A_{eff} = \frac{\left(\iint_{\infty}^{\infty} |F(x,y)|^2 dxdy\right)^2}{\iint_{\infty}^{\infty} |F(x,y)|^4 dxdy}. \tag{2.56}$$

Defining A_{eff} in this form, the quantity $\langle A|A\rangle$ represents optical power.

Equation (2.54) is called the vectorial nonlinear Schrödinger equation, which describes nonlinear evolution of a quasi-monochromatic optical field with an arbitrary state of polarization (SOP) in a birefringent and dispersive fiber. It is instructive to go through the individual terms in Eq. (2.54) and attach a physical meaning to them. Starting with the dispersive terms, $\beta_1 = 1/v_g$ is the inverse of the group velocity. In describing a single field, this term can be omitted by switching to a frame moving at the speed v_g along the z direction. However, when describing spectrally distinct fields and their interactions, the group-velocity difference between these fields can lead to significant walk off, which needs to be included properly. Group-velocity dispersion (GVD) is described by the β_2 term. Loosely speaking, because of β_2 different spectral components of a field have different group velocities, and this leads to broadening of the pulse in the time domain. It is useful to define a length scale L_D, called the dispersion length, at which a pulse goes through noticeable broadening:

$$L_D = \frac{T^2}{|\beta_2|}, \tag{2.57}$$

where T is a measure of pulse width. When the total length of the fiber L is much shorter than L_D it is usually safe to ignore the effects of fiber dispersion.

Fiber birefringence at the carrier frequency is described vector $\vec{b}_0$. This vector points in the direction of the fast birefringence axis in the Stokes space. Its magnitude is proportional to the fiber birefringence. Because of fiber birefringence, the two polarization components of the field aligned with the fast and slow axes of the fiber have different phase velocities. This causes periodic rotation of the polarization vector of the field if it initially lies in any direction other than the fast or slow axis. The period

of this rotation, L_B, is called the beat length and it is inversely proportional to fiber birefringence as

$$L_B = \frac{2\pi}{b_0}, \tag{2.58}$$

where $b_0 = |\vec{b}_0|$.

If the field has a wide spectrum, different polarization components of the field experience not only different phase velocities but also different group velocities. The axes that are parallel and orthogonal to the polarization-mode dispersion vector $\vec{b}_1$ are the directions in which group velocity is maximum and minimum, respectively. The difference between the maximum and minimum group velocities is related to the magnitude of the PMD vector as

$$b_1 = \frac{1}{v_{gy}} - \frac{1}{v_{gx}}, \tag{2.59}$$

where $b_1 = |\vec{b}_1|$ is the differential group delay, and v_{gx} and v_{gy} are the group velocities along the x and y axis, which are also assumed to be the fast and slow axes of the fiber, respectively. If two polarization components of a field travel with different group velocities a pulse splits in the time domain. Hence it experiences polarization-mode dispersion. The effect of a PMD vector in the frequency domain is that different frequency components experience different amounts of birefringence. Unless, the SOP of a field is parallel to the fast or slow axis, different frequency components of the field rotate at different rates, which leads to *polarization diffusion*.

The terms involving the nonlinear parameter γ in Eq. (2.54) describe the nonlinear evolution of the field. In the absence of linear terms, Eq. (2.54) has the following formal solution

$$|A(z,t)\rangle = \exp\left[i\gamma P z - \frac{i\gamma}{3}\int_0^z \langle A(z',t)|\boldsymbol{\sigma}_3|A(z',t)\rangle \boldsymbol{\sigma}_3 dz'\right]|A(0,t)\rangle, \tag{2.60}$$

where $P = \langle A|A\rangle$ is the total power. One effect of fiber nonlinearity is to introduce a power dependent phase shift, therefore it is said to cause self-phase modulation (SPM). If the field has a time-dependent power profile, SPM introduces time-dependent phase

shifts and thus broadens the field spectrum. In the special cases in which the initial SOP of the field is linear or circular, the exponent in Eq. (2.60) simplifies to scalar quantities $i\gamma PLz$ and $2i\gamma PLz/3$, respectively. However, for any other elliptically polarized field, the exponent in Eq. (2.60) is not scalar. Therefore, these fields experience an effective birefringence that depends on the total pump power, as well as on its polarization state. As a result, elliptically polarized fields are said to experience nonlinear polarization rotation. Nonlinear processes are discussed in more detail in the context of FWM equations.

2.6 Vectorial FWM Equations

The vectorial nonlinear Schrödinger equation can be used to describe various nonlinear processes that take place in a FOPA. An important nonlinear process is four-wave mixing (FWM); it allows power transfer from one or more strong pump fields to the so-called signal and idler fields. Launching only the strong pump fields leads to spontaneous parametric scattering. The process becomes stimulated when a weak signal field is launched together with the pump. As a result, the signal field is amplified and at the same time the idler is created such that the four fields satisfy the energy conservation requirement

$$\omega_1 + \omega_2 = \omega_3 + \omega_4, \tag{2.61}$$

where ω_1, ω_2, ω_3 and ω_4 are the frequencies for the two pumps, signal and idler respectively. If only a single pump is used, energy conservation requirement becomes $2\omega_1 = \omega_3 + \omega_4$.

As the four interacting fields are spectrally distinct, it is possible to obtain a separate equation for each field that explicitly shows the nonlinear interaction among them. To do this, the field is assumed to have the following form

$$|A(z,t)\rangle = \sum_{m=1}^{4} |A_m(z,t)\rangle \exp\{-i\beta(\omega_0)z - i(\omega_m - \omega_0)t\}. \tag{2.62}$$

Substituting Eq. (2.62) into Eq. (2.54) and separating different frequency components we obtain

$$\begin{aligned}\frac{\partial|A_j\rangle}{\partial z} &= \mathscr{L}(\omega_j)|A_j\rangle + i\gamma\Big\{\langle A_j|A_j\rangle - \frac{1}{3}\langle A_j|\boldsymbol{\sigma_3}|A_j\rangle\boldsymbol{\sigma_3} \\ &\quad + \sum_{m\neq j}^{4}\Big[\langle A_m|A_m\rangle + |A_m\rangle\langle A_m| - \frac{1}{3}\Big(\langle A_m|\boldsymbol{\sigma_3}|A_m\rangle + \boldsymbol{\sigma_3}|A_m\rangle\langle A_m|\Big)\boldsymbol{\sigma_3}\Big]\Big\}|A_j\rangle \\ &\quad + i\gamma\Big[|A_3\rangle\langle A_4^*| + |A_4\rangle\langle A_3^*| - \frac{\boldsymbol{\sigma_3}}{3}\Big(|A_3\rangle\langle A_4^*| + |A_4\rangle\langle A_3^*|\Big)\boldsymbol{\sigma_3}\Big]|A_{3-j}^*\rangle e^{-i\Delta\beta z}, \quad (2.63) \\ \frac{\partial|A_k\rangle}{\partial z} &= \mathscr{L}(\omega_k)|A_k\rangle + i\gamma\Big\{\langle A_k|A_k\rangle - \frac{1}{3}\langle A_k|\boldsymbol{\sigma_3}|A_k\rangle\boldsymbol{\sigma_3} \\ &\quad + \sum_{m\neq k}^{4}\Big[\langle A_m|A_m\rangle + |A_m\rangle\langle A_m| - \frac{1}{3}\Big(\langle A_m|\boldsymbol{\sigma_3}|A_m\rangle + \boldsymbol{\sigma_3}|A_m\rangle\langle A_m|\Big)\boldsymbol{\sigma_3}\Big]\Big\}|A_k\rangle \\ &\quad + i\gamma\Big[|A_1\rangle\langle A_2^*| + |A_2\rangle\langle A_1^*| - \frac{\boldsymbol{\sigma_3}}{3}\Big(|A_1\rangle\langle A_2^*| + |A_2\rangle\langle A_1^*|\Big)\boldsymbol{\sigma_3}\Big]|A_{7-k}^*\rangle e^{i\Delta\beta z}, \quad (2.64)\end{aligned}$$

where, $j = 1$ or 2, $k = 3$ or 4, m runs from 1 to 4, and $\Delta\beta$ is the wave-vector mismatch given by

$$\Delta\beta = \beta(\omega_3) + \beta(\omega_4) - \beta(\omega_1) - \beta(\omega_2). \quad (2.65)$$

The linear operator $\mathscr{L}(\omega_m)$ governs the evolution of the fields in the absence of nonlinearity and is given by

$$\begin{aligned}\mathscr{L}(\omega_m) &= -\frac{\alpha}{2} + i\left(\vec{b}_0(\omega_m) + i\vec{b}_1(\omega_m)\frac{\partial}{\partial t}\right)\cdot\vec{\boldsymbol{\sigma}} \\ &\quad + \beta(\omega_m) - \beta_1(\omega_m)\frac{\partial}{\partial t} - i\frac{\beta_2(\omega_m)}{2}\frac{\partial^2}{\partial t^2}. \quad (2.66)\end{aligned}$$

In Eqs. (2.63) and (2.64) the terms containing the nonlinearity coefficient γ show explicitly the nonlinear interactions among the fields. The first two terms are the SPM terms since they depend only on the field itself, and their only effect is to modify the phase of the field. Similarly, the terms gathered within the summation symbol only affect the phase of the field. Since these terms only consist of other fields, they are called the cross-phase modulation (XPM) terms. The last four terms are responsible for the FWM process. Unlike the SPM and XPM terms, the FWM terms are not purely imaginary; as a result, FWM can lead to power exchange among the fields. The efficiency

of the energy exchange depends on the wave-vector mismatch $\Delta\beta$ as well as on how strong the fields are.

Equations (2.63) and (2.64) describe the general case where the signal and idler fields can be as strong as the pumps. In fact, these equations are symmetric in the sense that subscripts 1 and 2 can be exchanged freely with 3 and 4, which also shows that energy flow can be from pumps to the signal and idler or vice versa. In practice, pump fields are much stronger than the signal and idler fields. Assuming weak signal and idler fields, we can drop those terms that are proportional to signal or idler amplitudes in Eq. (2.63) and linearize Eq. (2.64) in terms of the signal and idler fields as follows

$$\begin{aligned}\frac{\partial|A_1\rangle}{\partial z} &= \mathscr{L}(\omega_1)|A_1\rangle + i\gamma\Big[\langle A_1|A_1\rangle + \langle A_2|A_2\rangle + |A_2\rangle\langle A_2| \\ &\quad - \frac{1}{3}\Big(\langle A_1|\boldsymbol{\sigma_3}|A_1\rangle + \langle A_2|\boldsymbol{\sigma_3}|A_2\rangle + \boldsymbol{\sigma_3}|A_2\rangle\langle A_2|\Big)\boldsymbol{\sigma_3}\Big]|A_1\rangle, \qquad (2.67)\\ \frac{\partial|A_3\rangle}{\partial z} &= \mathscr{L}(\omega_3)|A_3\rangle + i\gamma\sum_{m=1}^{2}\Big[\langle A_m|A_m\rangle + |A_m\rangle\langle A_m| \\ &\quad - \frac{1}{3}\Big(\langle A_m|\boldsymbol{\sigma_3}|A_m\rangle + \boldsymbol{\sigma_3}|A_m\rangle\langle A_m|\Big)\boldsymbol{\sigma_3}\Big]|A_3\rangle \\ &\quad + i\gamma\Big[|A_1\rangle\langle A_2^*| + |A_2\rangle\langle A_1^*| - \frac{\boldsymbol{\sigma_3}}{3}\Big(|A_1\rangle\langle A_2^*| + |A_2\rangle\langle A_1^*|\Big)\boldsymbol{\sigma_3}\Big]|A_4^*\rangle e^{i\Delta\beta z}, \qquad (2.68)\end{aligned}$$

where equations for the second pump and the idler can be obtained by exchanging the subscript 1 with 2 in Eq. (2.67) and 3 with 4 in Eq. (2.68). Note also that as a result of neglecting terms that are proportional to signal and idler fields in Eq. (2.67), pump fields remain undepleted.

In many applications, continuous-wave (CW) or quasi-CW pumps are used. In this case, Eqs. (2.67) and (2.68) can be simplified even further since pumps retain their temporal profile. The change in the temporal profile of the pump is negligible as long as fiber is much shorter than the dispersion length $L < L_D$. When the pump fields have a narrow spectral width, and fiber losses are neglected for a relatively short fiber, the terms related to linear propagation of the fields $\mathscr{L}(\omega_m)$ in Eqs. (2.67) and (2.68) can be simplified to

$$\mathscr{L}(\omega_m) \approx i\vec{b}_0(\omega_m)\cdot\vec{\boldsymbol{\sigma}}. \qquad (2.69)$$

With these simplifications, it can be shown easily that pump powers remain unchanged during the propagation:

$$\frac{\partial\langle A_1|A_1\rangle}{\partial z} = \frac{\partial\langle A_2|A_2\rangle}{\partial z} = 0. \tag{2.70}$$

However, pump phases and polarizations can still evolve in a complicated manner depending on their initial values. Making use of the fact that pump powers remain constant, and by introducing a change of variables such that

$$|B_1\rangle = \exp\left[i\big(\langle A_1|A_1\rangle + \langle A_2|A_2\rangle\big)z\right]|A_1\rangle, \tag{2.71}$$

$$|B_3\rangle = \exp\left[i\left(\langle A_1|A_1\rangle + \langle A_2|A_2\rangle + \frac{\Delta\beta}{2}\right)z\right]|A_3\rangle. \tag{2.72}$$

Equations (2.67) and (2.68) can be written as

$$\begin{aligned}\frac{d|B_1\rangle}{dz} &= i\vec{b}_0(\omega_1)\cdot\vec{\boldsymbol{\sigma}}|B_1\rangle \\ &\quad + i\gamma\Big[|B_2\rangle\langle B_2| - \frac{1}{3}\Big(\langle B_1|\boldsymbol{\sigma_3}|B_1\rangle + \langle B_2|\boldsymbol{\sigma_3}|B_2\rangle + \boldsymbol{\sigma_3}|B_2\rangle\langle B_2|\Big)\boldsymbol{\sigma_3}\Big]|B_1\rangle, \qquad (2.73)\\ \frac{d|B_3\rangle}{dz} &= i\vec{b}_0(\omega_3)\cdot\vec{\boldsymbol{\sigma}}|B_1\rangle + i\frac{\Delta\beta}{2}|B_3\rangle \\ &\quad + i\gamma\sum_{m=1}^{2}\Big[|B_m\rangle\langle B_m| - \frac{1}{3}\Big(\langle B_m|\boldsymbol{\sigma_3}|B_m\rangle + \boldsymbol{\sigma_3}|B_m\rangle\langle B_m|\Big)\boldsymbol{\sigma_3}\Big]|B_3\rangle \\ &\quad + i\gamma\Big[|B_1\rangle\langle B_2^*| + |B_2\rangle\langle B_1^*| - \frac{\boldsymbol{\sigma_3}}{3}\Big(|B_1\rangle\langle B_2^*| + |B_2\rangle\langle B_1^*|\Big)\boldsymbol{\sigma_3}\Big]|B_4^*\rangle. \qquad (2.74)\end{aligned}$$

Once again, equations for the evolution of the second pump and the idler can be found by exchanging the subscripts 1 by 2 and 3 by 4.

The preceding FWM equations are derived for the more general case in which two pumps with distinct frequencies are used. FWM equations in the case of a single-pump FOPA can also be derived by the same procedure. These equations can also be obtained from the dual-pump FWM equations (2.73) and (2.74) by putting $|A_2\rangle = 0$, in Eq. (2.73) and by replacing both $|A_2\rangle$ and $|A_1\rangle$ by $|A_1\rangle/\sqrt{2}$ in Eq. (2.74). The FWM equations Eq. (2.63) that include pump depletion can also be used to get the single-pump equations in the same way.

2.7 Scalar FWM Equations

Even though Eqs. (2.73) and (2.74) are linear equations, they do not have a closed form analytical solution since in general pumps undergo a complicated nonlinear polarization rotation depending on their initial SOPs. It is possible to get solutions in the special cases in which pumps retain their SOPs. It is easy to verify from Eq. (2.67) that if the fiber has negligible birefringence, and both pumps are either linearly or circularly polarized such that their SOPs are either parallel or orthogonal, then pumps do not undergo nonlinear-polarization rotation. In fact, these four cases are frequently used in practice. Among these four schemes, it is instructive to examine the situation when all fields have the same linear SOP. Assuming that a field with narrow spectral bandwidth are traveling in a fiber with small birefringence and that fiber losses can be neglected, the solution of Eq. (2.73) for the non-depleted pumps can be written as follows

$$B_1(z) = B_1(0)\exp(2i\gamma P_2 z), \tag{2.75}$$

$$B_2(z) = B_2(0)\exp(2i\gamma P_1 z). \tag{2.76}$$

Inserting the solution for the pump fields into Eq. (2.74) for the signal and a similar equation for the idler leads to:

$$\frac{dB_3}{dz} = \frac{i}{2}\kappa B_3 + 2i\gamma B_1 B_2 B_4^*, \tag{2.77}$$

$$\frac{dB_4}{dz} = \frac{i}{2}\kappa B_4 + 2i\gamma B_1 B_2 B_3^*, \tag{2.78}$$

where B_k is the scalar field amplitude for the kth field defined as $|B_k\rangle = B_k|l\rangle$ and $|l\rangle$ is an arbitrary unit vector with real components in a linear basis. $\kappa = \Delta\beta + \gamma(P_1 + P_2)$ is called the phase-mismatch parameter. It incorporates phase mismatch originating from fiber dispersion as well as the imbalance in the nonlinear phase shift experienced by the two pumps, and the signal and idler. P_1 and P_2 are the pump powers.

Equations (2.77) and (2.78) can be used to find equations for the evolution of signal and idler powers $P_3 = |B_3|^2$ and $P_4 = |B_4|^2$ as [35]

$$\frac{dP_3}{dz} = \frac{dP_4}{dz} = 2\sqrt{P_1 P_2 P_3 P_4}\sin(\theta), \tag{2.79}$$

where $\theta = \phi_3 + \phi_4 - \phi_1 - \phi_2$ describes the accumulated phase mismatch among the four waves. Here ϕ_j is the phase of the field B_j, i.e., $B_j = \sqrt{P_j}\exp(i\phi_j)$. When the two pumps are assumed to remain undepleted, ϕ_1 and ϕ_2 maintain their initial values, and the accumulated phase mismatch is governed by

$$\frac{d\theta}{dz} = \kappa + 2\gamma\cos\theta\frac{\sqrt{P_1P_2}(P_3+P_4)}{\sqrt{P_3P_4}}. \tag{2.80}$$

Equation (2.79) shows clearly that the growth of the signal and idler waves inside a fiber is determined by the phase-matching condition. When $\theta = \pi/2$, the signal and idler extract energy from the two pumps. In contrast, when $\theta = -\pi/2$, energy can flow back to the two pumps from the signal and idler. If only the two pumps and the signal are launched into FOPA initially, the idler wave is automatically generated by the FWM process. This can be seen from Eq. (2.78). Even if $B_4 = 0$ at $z = 0$, its derivative is not zero as long as $B_3(0)$ is finite. Integrating this equation over a short fiber section of length Δz, one obtains $\Delta B_4 \approx 2i\gamma B_1 B_2 B_3^*(0)\Delta z$. The factor of i provides an initial value of $\pi/2$ for θ and shows that the correct phase difference is automatically picked up by the FWM process [35]. If $\kappa = 0$ initially (perfect phase matching), Eq. (2.80) shows that θ will remain frozen at its initial value of $\pi/2$. However, if $\kappa \neq 0$, θ will change along the fiber as dictated by Eq. (2.80), and energy will flow back into the two pumps in a periodic fashion. Thus, phase matching is critical for signal amplification and idler generation.

3 Parametric Amplifiers

Fiber-optic parametric amplifiers (FOPAs) are based on the FWM process. However, the gain produced by FOPAs cannot be described by the FWM process itself. Important FOPA properties such as available gain bandwidth and gain uniformity depend on the phase-matching condition. This Chapter discusses in detail how FOPAs are designed to yield wide and uniform gain bandwidths.

FOPAs can be divided into two broad categories depending on whether they use a single pump or two pumps at different frequencies. In Section 3.1, a simplified scalar FWM theory is used to introduce the basic concepts of FOPAs in the case of single-pump FOPAs. Section 3.2 introduces dual-pump FOPAs, and discusses their differences, and advantages by comparing to single-pump FOPAs. In Section 3.3, the polarization-dependence of FOPAs is discussed in detail for both single-and dual-pump FOPAs, by making full use of the vectorial nature of FWM equations derived in Chapter 2. Finally, in Section 3.4, several important applications that make use of FOPAs are described, and the limitations of FOPAs are discussed.

3.1 Single-Pump Parametric Amplifiers

In this Section the focus is on a simpler case in which a single intense pump is launched into a fiber together with the signal, and a single idler wave is generated through the degenerate FWM process. FWM equations in the case of single-pump FOPAs can be derived starting from Eqs. (2.73) and (2.74). Assuming for the sake of simplicity that all fields are linearly polarized along x-axis, $|B_k\rangle = B_k\hat{x}$, simple scalar FWM equations can be obtained by putting $B_2 = 0$ in Eq. (2.73) and replacing both B_1 and B_2 by $B_1/\sqrt{2}$ in Eq. (2.74). With these simplifications, signal and idler equations become:

$$\frac{dB_3}{dz} = \frac{i}{2}\kappa B_3 + i\gamma B_1^2 B_4^* \tag{3.1}$$

$$\frac{dB_4}{dz} = \frac{i}{2}\kappa B_4 + i\gamma B_1^2 B_3^* \tag{3.2}$$

where in this case $\kappa = \Delta\beta + 2\gamma P_1$. Equations (3.1) and (3.2) can easily be solved to find the signal gain. These equations can also be integrated in an elegant fashion by making use of the Pauli spin matrices. With the use of Pauli spin matrices Eqs. (3.1) and (3.2) can be written as

$$\frac{d}{dz}\begin{bmatrix} B_3 \\ B_4^* \end{bmatrix} = \vec{g}\cdot\vec{\boldsymbol{\sigma}}\begin{bmatrix} B_3 \\ B_4^* \end{bmatrix}, \tag{3.3}$$

where $[B_3, B_4^*]^{\mathrm{T}}$ does not correspond to any physical vector but is merely a mathematical construct and $\vec{g} = [i\kappa/2, -\gamma\mathrm{Im}(B_1^2), -\gamma\mathrm{Re}(B_1^2)]$ is a constant vector. Equation (3.3) can be integrated formally to obtain

$$\begin{bmatrix} B_3(L) \\ B_4^*(L) \end{bmatrix} = \exp(\vec{g}\cdot\vec{\boldsymbol{\sigma}}L)\begin{bmatrix} B_3(0) \\ B_4^*(0) \end{bmatrix}. \tag{3.4}$$

The exponential matrix can be expanded as follows

$$\exp(\vec{a}\cdot\vec{\boldsymbol{\sigma}}) = \cosh a + \hat{a}\cdot\vec{\boldsymbol{\sigma}}\sinh a, \tag{3.5}$$

where $\vec{a}$ is any three-component vector with $a = \sqrt{\vec{a}\cdot\vec{a}}$ and $\hat{a} = \vec{a}/a$. Using this relation in Eq. (3.4), solutions for the signal and idler fields is found to be

$$B_3(L) = B_3(0)\left[\cosh(gL) + \frac{i\kappa}{2g}\sinh(gL)\right] + B_4^*(0)\frac{i\gamma B_1^2}{g}\sinh(gL), \tag{3.6}$$

$$B_4(L) = B_4(0)\left[\cosh(gL) + \frac{i\kappa}{2g}\sinh(gL)\right] + B_3^*(0)\frac{i\gamma B_1^2}{g}\sinh(gL), \tag{3.7}$$

where the parametric gain coefficient g is given by (with $P_1 = |B_1|^2$)

$$g = \sqrt{\vec{g}\cdot\vec{g}} = \sqrt{(\gamma P_1)^2 - (\kappa/2)^2}. \tag{3.8}$$

Signal gain at the end of the fiber, defined as $G(\omega_3) = |B_3(L)/B_3(0)|^2$, can be found from Eq. (3.6). In particular, when there is no idler field at the input of the fiber, the signal gain becomes

$$G(\omega_3) = \left[1 + (1 + \kappa^2/4g^2)\sinh^2(gL)\right]. \tag{3.9}$$

Equation (3.8) shows that the parametric gain is reduced by phase mismatch κ and is maximum when $\kappa = 0$. Both the nonlinear (SPM and XPM) and the linear effects (fiber dispersion) contribute to κ. Although the nonlinear contribution is constant at a given pump power, the linear phase mismatch depends on the wavelengths of the three waves. To realize net amplification of the signal, the parametric gain g should be real. Thus, tolerable values of the linear phase mismatch $\Delta\beta$ are limited to the range $-4\gamma P_1 \leq \Delta\beta \leq 0$. The FOPA gain is maximum when the phase mismatch κ approaches zero, or when $\Delta\beta = -2\gamma P_1$. This relation indicates that optimal operation of FOPAs requires some amount of negative linear mismatch to compensate for the nonlinear phase mismatch. In fact, the bandwidth of the gain spectrum is determined by the pump power and the nonlinear parameter γ. Figure 3.1 shows this dependence clearly by plotting the parametric gain coefficient g as a function of $\Delta\beta$ for three different power levels of the pump [3].

The linear phase mismatch $\Delta\beta$ depends on the dispersion characteristics of the fiber. As the signal and idler frequencies are located symmetrically around the pump fre-

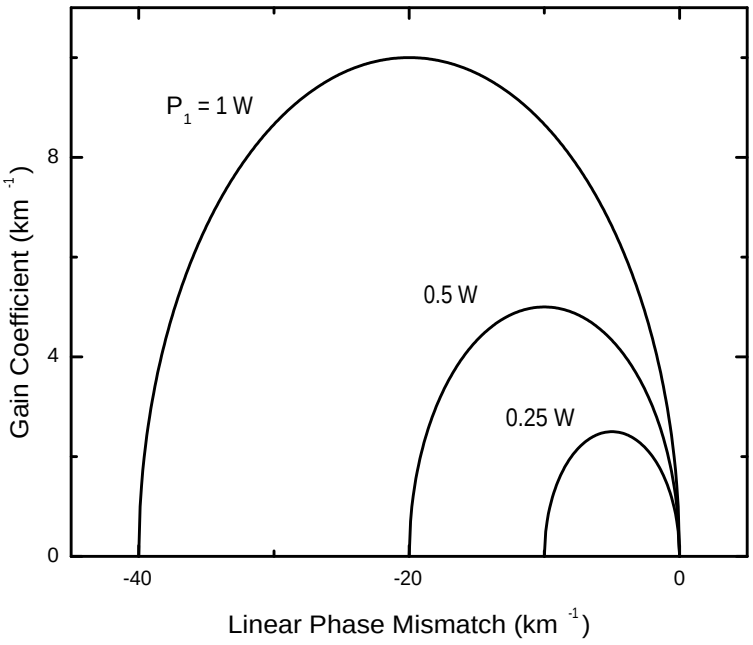

Figure 3.1: Parametric gain coefficient g for a single-pump FOPA as a function of linear phase mismatch at three pump powers P_1 for a fiber with $\gamma = 10$ W^{-1}/km.

quency ($\omega_4 = 2\omega_1 - \omega_3$), it is useful to expand $\Delta\beta$ in a Taylor series around the pump frequency as [31]

$$\Delta\beta = \beta(\omega_3) + \beta(\omega_4) - 2\beta(\omega_1) = 2\sum_{m=1}^{\infty} \beta_{mp} \frac{(\omega_3 - \omega_1)^{2m}}{(2m)!}, \tag{3.10}$$

where $\beta_{mp} = (d^{2m}\beta / d\omega^{2m})_{\omega=\omega_1}$. This equation shows that only even-order dispersion parameters evaluated at the pump frequency contribute to the linear phase mismatch. Clearly, the choice of the pump wavelength is very critical while designing a FOPA. The linear phase mismatch $\Delta\beta$ is dominated by the second-order dispersion parameter β_{2p} when the signal wavelength is close to the pump but by the fourth- and higher-order dispersion parameters (β_{4p}, β_{6p}, etc.) when the signal deviates far from it. Thus, the ultimate FOPA bandwidth depends on the spectral range over which the linear phase mismatch is negative but large enough to balance the constant positive nonlinear phase mismatch of $2\gamma P_1$. This can be achieved by slightly displacing the pump wavelength from the ZDWL of the fiber such that β_{2p} is negative but β_{4p} is positive.

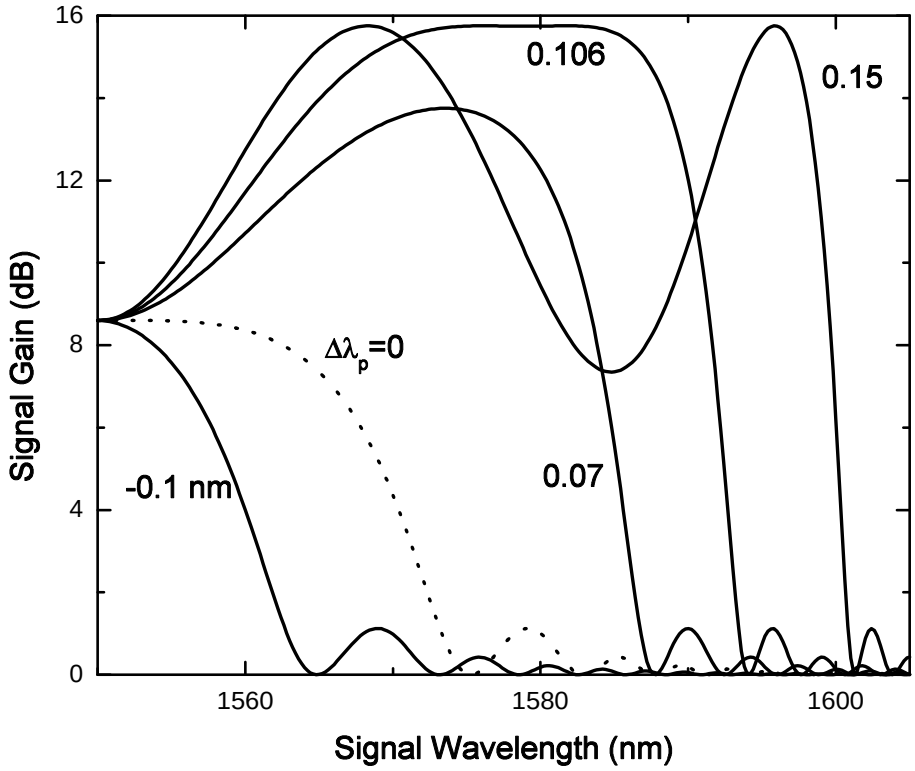

Figure 3.2: Gain spectra for a single-pump FOPA for several values of pump detuning $\Delta\lambda_p = \lambda_1 - \lambda_0$ from the ZDWL λ_0. The parameters used are $\gamma = 2$ W^{-1}/km, $P_1 = 0.5$ W, $L = 2.5$ km, $\beta_3 = 0.1$ ps^3/km, and $\beta_4 = 10^{-4}$ ps^4/km.

One should relate the parameters β_{2p} and β_{4p} to the fiber-dispersion parameters, $\beta_m = (d^m\beta/d\omega^m)_{\omega=\omega_0}$, calculated at the ZDWL of the fiber. This can be accomplished by expanding $\beta(\omega)$ in a Taylor series around ω_0. Keeping the terms up to fourth order in this expansion gives:

$$\beta_{2p} \approx \beta_3(\omega_1 - \omega_0) + \frac{\beta_4}{2}(\omega_1 - \omega_0)^2, \qquad \beta_{4p} \approx \beta_4. \tag{3.11}$$

Depending on the values of the fiber parameters β_3 and β_4, one can choose the pump frequency ω_1 such that β_{2p} and β_{4p} have opposite signs. More specifically, since both β_3 and β_4 are positive for most silica fibers, one should choose $\omega_1 < \omega_0$, i.e., the pump wavelength should be longer than the ZDWL of the fiber.

Figure 3.2 shows the gain spectra $G(\omega_3)$ at several different pump wavelengths in the vicinity of the ZDWL λ_0 (chosen to be 1550 nm) by changing the pump detuning $\Delta\lambda_p = \lambda_1 - \lambda_0$ in the range -0.1 to $+0.15$ nm. The dotted curve shows the case $\Delta\lambda_p = 0$ for which pump wavelength coincides with the ZDWL exactly. The peak gain is about 8 dB and the gain bandwidth is limited to below 40 nm. When the pump is tuned toward shorter-wavelength side, the bandwidth actually decreases. In contrast, both the peak gain and the bandwidth are enhanced by tuning the pump toward the longer-wavelength side. The signal gain in the vicinity of pump is the same regardless of pump wavelength. When signal wavelength moves away from the pump, the linear phase mismatch $\Delta\beta$ strongly depends on the pump wavelength. If both the third- and forth-order dispersion parameters are positive at ZDWL, according to Eq (3.11) the second order dispersion at the pump is negative when $\Delta\lambda_p$ is slightly positive, and thus can compensate for the nonlinear phase mismatch. This is the reason why the gain peak is located at a wavelength far from the pump when $\lambda_1 > \lambda_0$. When phase matching is perfect ($\kappa = 0$), FOPA gain grows exponentially with the fiber length L as $G = 1 + \exp(2\gamma P_1 L)/4$. For the parameters used for 3.2, the best case occurs when $\Delta\lambda_p = 0.106$ nm. However, when $\Delta\lambda_p < 0$, both the second- and forth-order dispersion parameters for the pump are positive. As a result, the linear phase mismatch adds up with with the nonlinear one, making κ relatively large. As a result, the FOPA bandwidth is reduced. For fibers that have a negative β_4, it is not possible to balance β_2 and β_4, therefore these fibers provide a narrower gain bandwidth.

As the pump wavelength is pushed further into the anomalous side, a second gain peak forms. This peak moves away from the ZDWL, and it narrows as $\Delta\lambda_p$ is increased. This feature can be used when a signal far from the pump field has to be amplified but a large gain bandwidth is not essential [32]. Figure 3.3 shows that as the pump detuning from the ZDWL is increased from 0.2 to 1 nm, the second peak moves from 1605 nm to 1685 nm. In principle, this peak can be moved arbitrarily far. However, as the gain bandwidth narrows down with a larger detuning, and the peak location is

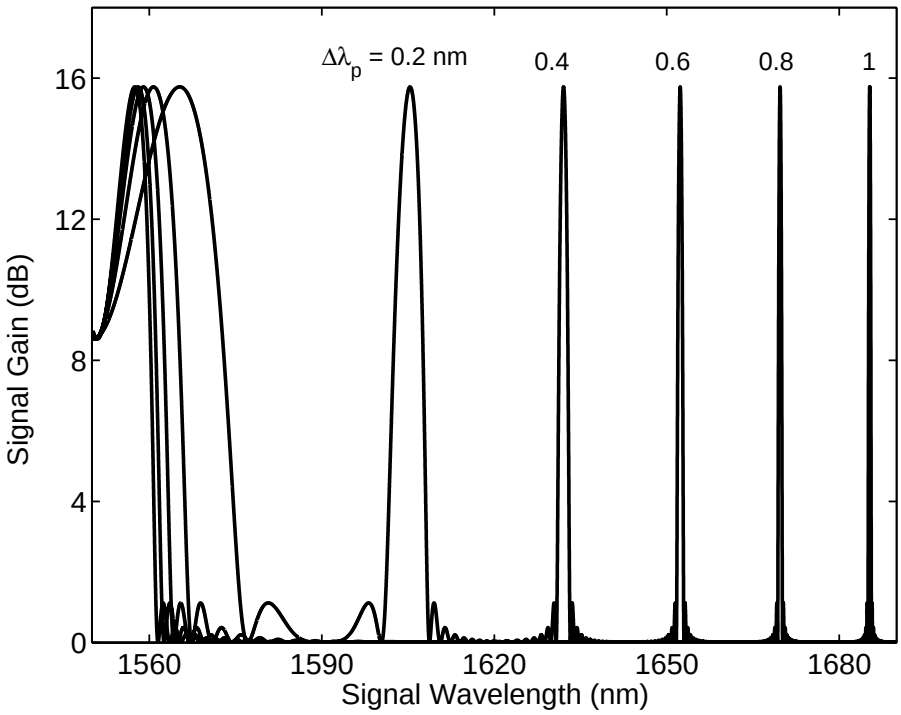

Figure 3.3: Gain spectra for a single-pump FOPA for several values of pump detuning. The same parameter set that is used in Fig. 3.2 is used.

highly sensitive to the exact value of pump wavelength, slight deviations in the pump wavelength causes large changes in the signal gain. Similar results are obtained when β_4 is negative by tuning the pump wavelength into the normal dispersion side.

From a practical standpoint, one wants to maximize both the peak gain and the gain bandwidth at a given pump power P_1. Since the peak gain in Eq. (3.9) is approximately given by $G_p \approx \exp(2\gamma P_1 L)/4$, its value increases exponentially with the fiber length. However, the gain bandwidth scales inversely with L because the phase mismatch increases for longer fibers. The obvious solution is to use a fiber as short as possible. However, as the available amount of gain is a function of $\gamma P_1 L$, shortening of fiber length must be accompanied with an increase in the value of γP_1 to maintain the same amount of gain. This behavior is illustrated in Figure 3.4 where the gain bandwidth is shown to increase significantly when large values of γP_1 are combined with shorter

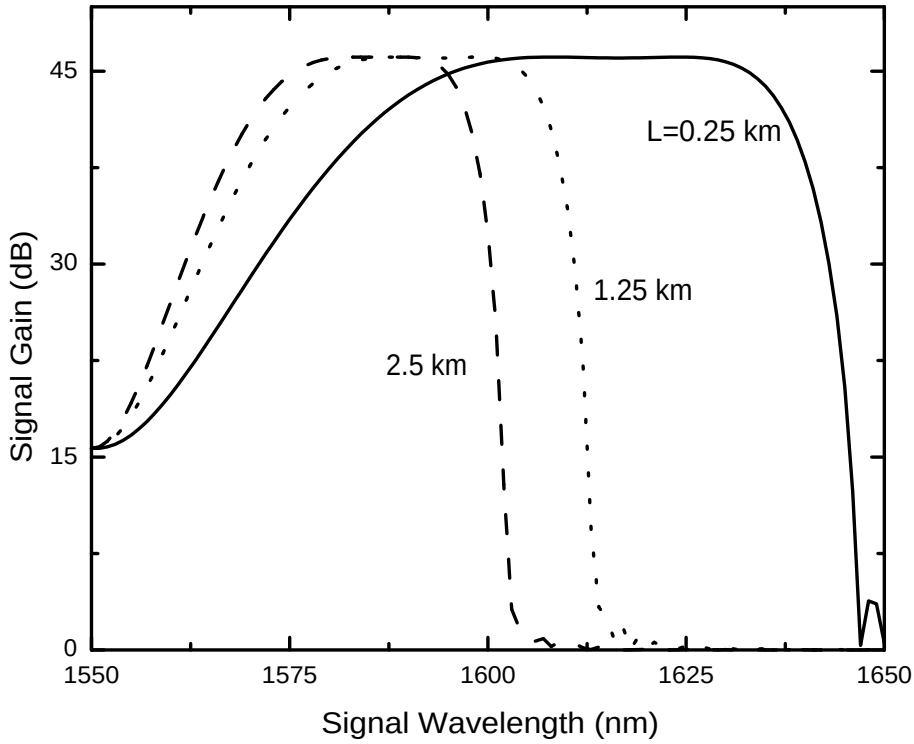

Figure 3.4: Gain spectra for single-pump FOPAs of three different lengths. The product $\gamma P_1 L = 6$ is kept constant for all curves. Other parameters are the same as those used for Figure 3.2.

lengths of fiber. The solid curve obtained for the 250-m-long fiber exhibits a 50-nm region on each side of the ZDWL over which the gain is nearly flat. Therefore, a simple rule of thumb for single-pump FOPAs is to use as high pump power as possible together with a fiber with as large a nonlinearity as possible. Since n_2 is fixed for silica fibers, the nonlinear parameter γ can be increased only by reducing the effective core area. Such fibers have become available in recent years and are called high-nonlinearity fibers (HNLFs) even though it is not the material nonlinearity n_2 that is enhanced in such fibers. Values of $\gamma \gg 10$ W^{-1}/km can be realized in such fibers [33]. Photonic crystal fibers exhibiting high values of γ have also been used to build FOPAs [34]

HNLFs have been used to make FOPAs with a large bandwidth. In a 2001 experiment, a 200-nm gain bandwidth was realized by employing Raman-assisted parametric

amplification inside a 20-m-long HNLF with $\gamma = 18$ W^{-1}/km [36]. The required pump power ($\sim$ 10 W) was large enough that the signal was also amplified by stimulated Raman scattering when its wavelength exceeded the pump wavelength. Recent advances in designing microstructure fibers also make it possible to use short fiber lengths. A net peak gain of 24.5 dB over a bandwidth of 20 nm has been realized inside a 12.5-m-long microstructure fiber with $\gamma = 24$ W^{-1}/km pumped by high-energy pulses [34]. In another 2003 experiment, a peak gain of 43 dB with 85 nm bandwidth was obtained by pumping the FOPA with pulses at a repetition rate of 20 Gb/s [37]. However, a pulse-pumped FOPA requires either synchronization between the pump and signal pulses or pumping at a repetition rate much higher than that of the signal.

Another scheme for mitigating the phase-matching problem manages fiber dispersion along the fiber length, resulting in the so-called quasi-phase matching. This can be realized either through periodic dispersion compensation [38], [39] or by carefully arranging different sections of the fiber with different dispersion properties [40]–[42]. As quasi-phase matching can be maintained along a fairly long length, continuous-wave (CW) pumps can be used and still realize considerable amount of gain. Figure 3.5 shows the experimental results for such a single-pump FOPA [43] where both the net signal gain and the net conversion efficiency at the idler wavelength are shown at several pump-power levels. At a pump power of 31.8 dBm (about 1.5 W) at 1563 nm, the FOPA provided 49-dB peak gain. It was designed using a 500-m-long HNLF ($\gamma = 11$ W^{-1}/km) with low dispersion (dispersion slope $S = 0.03$ ps/nm^2/km). The fiber was composed of three sections with ZDWLs (1556.8, 1560.3, 1561.2 nm, respectively). In another experiment that used the same technique, a single-pump FOPA produced 70 dB gain with 1.9 W of pump power [44].

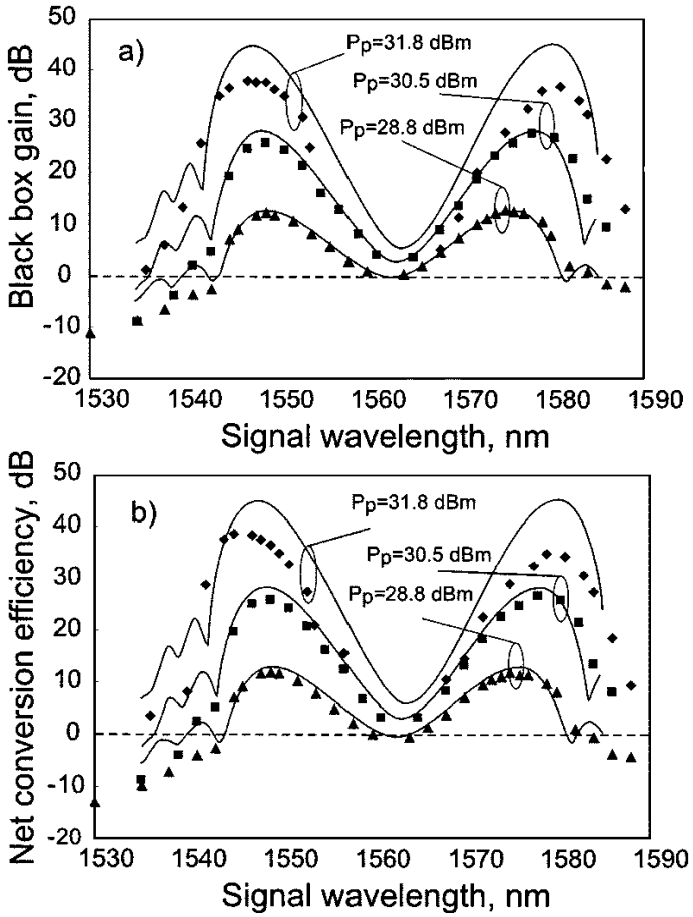

Figure 3.5: (a) Measured signal gain and (b) idler conversion efficiency for a single-pump FOPA at several pump powers. Solid curves show the theoretically expected results.

3.2 Dual-Pump Parametric Amplifiers

In the previous Section the simpler case of single-pump FOPAs is used to explain the basic features of FOPA design. This Section focuses on dual-pump FOPAs that employ the nondegenerate FWM process using two pumps with different frequencies [10]–[12], [45]–[50]. Because of the extra degrees of freedom presented by the second pump in terms of its frequency and SOP, dual-pump FOPAs have several advantages over single-pump FOPAs. The most important advantage is that they can provide relatively

flat gain over a much wider bandwidth than what is possible with single-pump FOPAs, [48], [49].

In the case of nondegenerate FWM, two distinct photons, one from each pump, are used to create the signal and idler photons as shown in Eq. (2.1). Using Eqs. (2.77) and (2.78) it can be shown that the expression for the signal gain in dual-pump FOPAs is the same as the expression (3.9) found in the case of single-pump FOPAs, [3]

$$G(\omega_3) = \left[1 + (1 + \kappa^2/4g^2)\sinh^2(gL)\right]. \tag{3.12}$$

However, in the case of dual-pump FOPAs, the expression for the parametric gain coefficient g and phase-mismatch parameter κ are slightly different:

$$g = \sqrt{(2\gamma)^2 P_1 P_2 - (\kappa/2)^2}, \tag{3.13}$$

$$\kappa = \Delta\beta + \gamma(P_1 + P_2), \tag{3.14}$$

where P_1 and P_2 are the input pump powers, assumed to remain undepleted.

Similar to the single-pump case, one can expand the linear phase mismatch $\Delta\beta = \beta(\omega_3) + \beta(\omega_4) - \beta(\omega_1) - \beta(\omega_2)$ in a Taylor series as [46]:

$$\Delta\beta = 2\sum_{m=1}^{\infty} \frac{1}{(2m)!}\left(\frac{d^{2m}\beta}{d\omega^{2m}}\right)_{\omega=\omega_c} \left[(\omega_3 - \omega_c)^{2m} - \omega_d^{2m}\right]. \tag{3.15}$$

where $\omega_c = (\omega_1 + \omega_2)/2$ is the mean frequency of the two pumps and $\omega_d = (\omega_1 - \omega_2)/2$ is the half of their frequency difference. This equation differs from the phase-mismatch term in the case of single-pump FOPA Eq. (3.10) by the last term. The ω_d term contributes only when two pumps are used and is independent of the signal and idler frequencies. This difference provides the main advantage of dual-pump FOPAs over single-pump FOPAs as the ω_d term can be used to control the phase mismatch. By properly choosing the pump wavelengths, it is possible to use this term for compensating the nonlinear phase mismatch $\gamma(P_1 + P_2)$ stemming from SPM and XPM. As a result, the total phase mismatch κ can be maintained close to zero over a quite wide spectral range after the first term is made small by balancing carefully different orders of fiber dispersion.

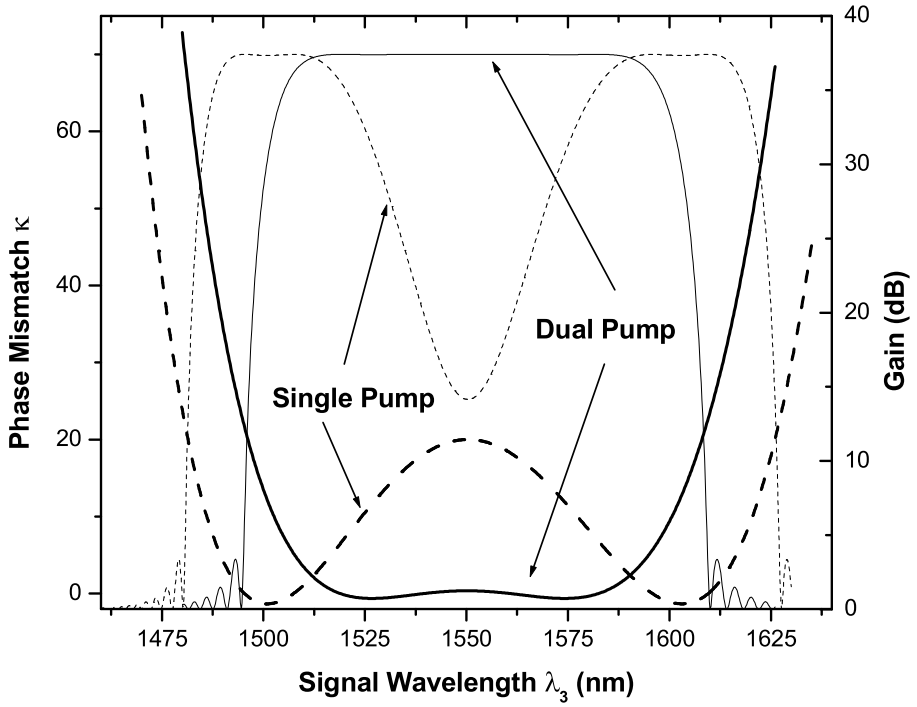

Figure 3.6: Optimized gain spectra for single-pump and dual-pump FOPAs and corresponding phase-mismatch κ. Same amount of total pump power was used in both cases.

The importance of the ω_d term can be best seen by comparing the phase-matching parameter κ for single- and dual pump FOPAs. Equation (3.10) shows that it is hard to maintain this phase-matching condition over a wide bandwidth in a single-pump FOPA. This is because $\Delta\beta \rightarrow 0$ when the signal wavelength approaches the pump wavelength, and hence $\kappa \rightarrow 2\gamma P_1$. This value of κ is quite large and results in only a quadratic growth of signal ($G = 1 + \gamma^2 P_1^2 L^2$). The net result is that the signal gain is considerably reduced in the vicinity of the pump wavelength, and the gain spectrum exhibits a dip when single-pump FOPAs are used. However, in the case of dual-pump FOPAs, by choosing the pump frequencies properly ω_d can be used to compensate for nonlinear contribution to phase mismatch. Figure 3.6 compares the phase-mismatch parameter κ for single-and dual pump FOPAs shown by thick dashed and thick solid curves, respectively. The corresponding gain spectra are shown by the thin dashed and

thin solid curves. For single-pump FOPAs, the value of κ is fixed to $2\gamma P_1$ at the pump wavelength $\lambda_1 = 1550$ nm. Therefore, the gain profile has a dip at the center (thin dashed curve) [36].

The most commonly used configuration of dual-pump FOPAs employs a relatively large wavelength difference between the two pumps for realizing flat gain over a wide spectral range. This increases the magnitude of the ω_d term so that linear phase mismatch is large enough to compensate for nonlinear phase mismatch. At the same time, the mean frequency of the two pumps ω_c is set close to the ZDWL of the fiber so that the linear phase mismatch in Eq. (3.15) is kept constant over a broad range of ω_3. Therefore, to achieve a fairly wide phase matching range, the two pump wavelengths should be located on the opposite sides of the ZDWL in a symmetric fashion, but should be reasonably far from it [10]. Figure 3.6 shows how κ can be reduced to zero over a wide wavelength range using such a scheme, resulting in a flat broadband gain spectrum. Comparing the single-pump and dual-pump cases, it can be seen that although single-pump FOPAs may provide nonuniform gain over a wider bandwidth under certain conditions, dual-pump FOPAs provide much more uniform gain in general.

The preceding discussion is based on the assumption that only the nondegenerate FWM process, $\omega_1 + \omega_2 = \omega_3 + \omega_4$, contributes to FOPA gain. However, the situation is much more complicated for dual-pump FOPAs because the degenerate FWM process associated with each intense pump, i.e. $2\omega_1 = \omega_3 + \omega_5$ and $2\omega_2 = \omega_3 + \omega_6$, always occurs simultaneously with the nondegenerate one. In fact, it turns out that the combination of degenerate and nondegenerate FWM processes can create eight other idler fields besides the one at the frequency ω_4 [5], [10]. Only four among these idlers, say at frequencies $\omega_5,\ \omega_6,\ \omega_7$, and ω_8, are significantly relevant for describing the gain spectrum of FOPA because they are related to the signal frequency through the relations:

$$2\omega_1 \rightarrow \omega_3 + \omega_5, \qquad 2\omega_2 \rightarrow \omega_3 + \omega_6, \tag{3.16}$$

$$\omega_1 + \omega_3 \rightarrow \omega_2 + \omega_7, \qquad \omega_2 + \omega_3 \rightarrow \omega_1 + \omega_8. \tag{3.17}$$

Although these degenerate and nondegenerate FWM processes look as simple as Eq. (2.1) at the first glance, they do not occur independently because energy conversion is also maintained among the following processes:

$$2\omega_1 \rightarrow \omega_4 + \omega_7, \qquad 2\omega_2 \rightarrow \omega_4 + \omega_8, \tag{3.18}$$

$$\omega_1 + \omega_2 \rightarrow \omega_5 + \omega_8, \qquad \omega_1 + \omega_2 \rightarrow \omega_6 + \omega_7, \tag{3.19}$$

$$\omega_1 + \omega_4 \rightarrow \omega_2 + \omega_5, \qquad \omega_1 + \omega_6 \rightarrow \omega_2 + \omega_4. \tag{3.20}$$

All of these processes involve at least two photons from one or both intense pumps and will occur in the same order as the process in Eq (2.1) as long as their phase matching conditions are satisfied. As a result, a complete description of the FWM processes inside dual-pump FOPA becomes quite complicated [10]. Fortunately, a detailed analysis shows that the phase matching conditions associated with these processes are quite different. When the two pumps are located symmetrically far from the ZDWL of the fiber, the ten FWM processes shown in Eqs. (3.16)–(3.20) can only occur when the signal is in the vicinity of the two pumps. Thus, they leave unaffected the central flat part of the parametric gain spectrum resulting from the process shown in Eq. (2.1) [10], which is mainly used in practice. Figure 3.7 compares the FOPA gain spectrum obtained numerically using a complete analysis that includes all five idlers model (Solid curve) with that obtained using the sole nondegenerate FWM process of Eq. (2.1). It can be seen clearly that the flat portion of the gain spectrum has its origin in the single FWM process of Eq. (2.1). The other 10 processes only affect the edges of gain spectrum and reduce the gain bandwidth by 10–20%. Thus, it can be concluded that a model based on Eq. (2.1) is sufficient to describe the performance of dual-pump FOPAs as long as the central flat gain region is used experimentally.

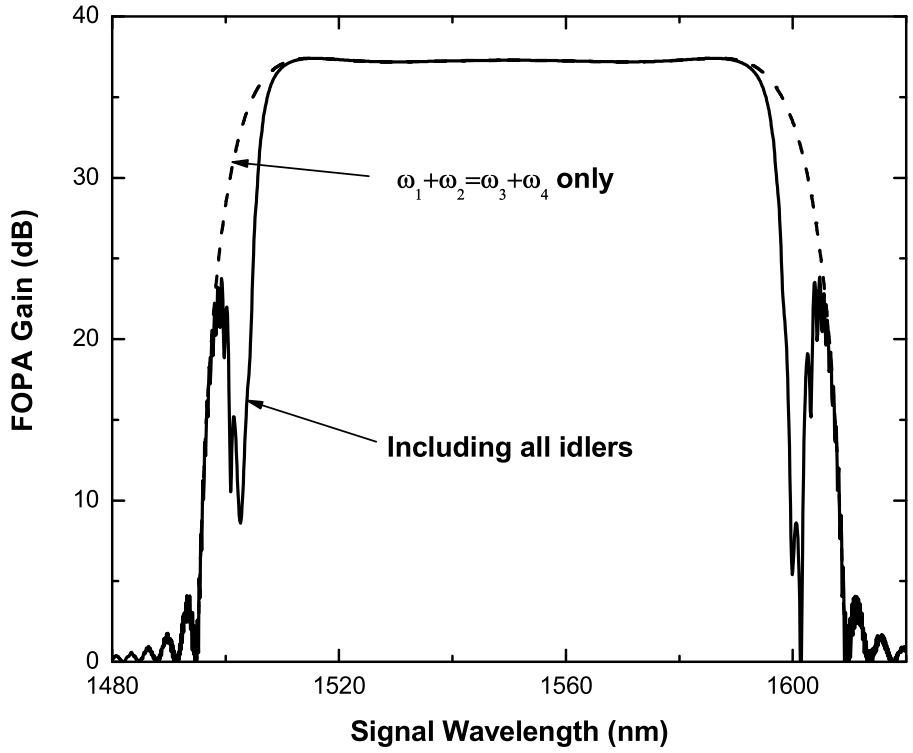

Figure 3.7: Gain spectra for a dual-pump FOPA including the contribution of all idlers (solid curve). The dotted curve shows gain spectrum when only a single idler corresponding to the dominant nondegenerate FWM process is included. The parameters used are $L = 0.5$ km, $\gamma = 10$ W^{-1}/km, $P_1 = 0.5$ W, $P_2 = 0.5$ W, $\beta_3 = 0.1$ ps^3/km, $\beta_4 = 10^{-4}$ ps^4/km, $\lambda_1 = 1502.6$ nm, $\lambda_2 = 1600.6$ nm, and $\lambda_0 = 1550$ nm.

3.3 Polarization Dependence of FOPA Gain

The FWM equations Eqs. (2.67) and (2.68) derived in Chapter 2 show that FWM has a vectorial nature. The efficiency of the FWM process depends on the state of polarization (SOP) of the pumps, signal and idler [50]. So far, the vectorial nature of the FWM process was neglected. It was assumed that all fields are launched with the same linear polarization and that they retain their input SOPs along the fiber. In general, this assumption breaks down in two respects. First, it may not be possible to control the input SOPs of the fields. For instance, in a communication system, the input SOP of

the signal varies randomly. Secondly, even if the input SOPs are fixed, they may not retain their polarization states along the fiber due to fiber irregularities. It is important to understand how FWM efficiency depends on the SOPs of the interacting fields to describe FOPA gain correctly. What is more, the polarization dependence of FWM provides another degree of freedom to design fiber-optic parametric amplifiers that may be useful for different applications.

In this Section, the vectorial nature of FWM is investigated. First, the fiber is assumed to be perfectly isotropic. In practice, this can be nearly achieved for short lengths of fiber < 10 m and it allows for investigating the vectorial nature of FWM processes itself. Second, this assumption will also be relaxed and it will be shown that FOPAs that use longer lengths of fiber exhibit a different polarization dependence.

3.3.1 Theoretical Model

The starting point is the vectorial FWM equations (2.67) and (2.68) derived in Chapter 2:

$$\frac{d|A_1\rangle}{dz} = i\beta(\omega_1)|A_1\rangle + i\vec{b}\cdot\vec{\boldsymbol{\sigma}}|A_1\rangle + i\gamma\Big[P_1+P_2+|A_2\rangle\langle A_2| - \frac{1}{3}\Big(\langle A_1|\boldsymbol{\sigma_3}|A_1\rangle + \langle A_2|\boldsymbol{\sigma_3}|A_2\rangle + \boldsymbol{\sigma_3}|A_2\rangle\langle A_2|\Big)\boldsymbol{\sigma_3}\Big]|A_1\rangle, \tag{3.21}$$

$$\frac{d|A_2\rangle}{dz} = i\beta(\omega_2)|A_2\rangle + i[\vec{b}+\vec{b}_1(\omega_2-\omega_1)]\cdot\vec{\boldsymbol{\sigma}}|A_2\rangle + i\gamma\Big[P_1+P_2+|A_1\rangle\langle A_1| - \frac{1}{3}\Big(\langle A_2|\boldsymbol{\sigma_3}|A_2\rangle + \langle A_1|\boldsymbol{\sigma_3}|A_1\rangle + \boldsymbol{\sigma_3}|A_1\rangle\langle A_1|\Big)\boldsymbol{\sigma_3}\Big]|A_1\rangle, \tag{3.22}$$

$$\begin{aligned}\frac{d|A_3\rangle}{dz} &= i\beta(\omega_3)|A_3\rangle + i[\vec{b}+\vec{b}_1(\omega_3-\omega_1)]\cdot\vec{\boldsymbol{\sigma}}|A_3\rangle \\ &+ i\gamma\Big[P_1+P_2+|A_1\rangle\langle A_1|+|A_2\rangle\langle A_2| \\ &- \frac{1}{3}\Big(\langle A_1|\boldsymbol{\sigma_3}|A_1\rangle + \langle A_2|\boldsymbol{\sigma_3}|A_2\rangle + \boldsymbol{\sigma_3}|A_1\rangle\langle A_1| + \boldsymbol{\sigma_3}|A_2\rangle\langle A_2|\Big)\boldsymbol{\sigma_3}\Big]|A_3\rangle \\ &+ i\gamma\Big[|A_1\rangle\langle A_2^*| + |A_2\rangle\langle A_1^*| - \frac{\boldsymbol{\sigma_3}}{3}\Big(|A_1\rangle\langle A_2^*| + |A_2\rangle\langle A_1^*|\Big)\boldsymbol{\sigma_3}\Big]|A_4^*\rangle,\end{aligned} \tag{3.23}$$

$$\begin{aligned}\frac{d|A_4\rangle}{dz} &= i\beta(\omega_4)|A_4\rangle + i[\vec{b}+\vec{b}_1(\omega_4-\omega_1)]\cdot\vec{\boldsymbol{\sigma}}|A_4\rangle \\ &+ i\gamma\Big[P_1+P_2+|A_1\rangle\langle A_1|+|A_2\rangle\langle A_2| \\ &- \frac{1}{3}\Big(\langle A_1|\boldsymbol{\sigma_3}|A_1\rangle + \langle A_2|\boldsymbol{\sigma_3}|A_2\rangle + \boldsymbol{\sigma_3}|A_1\rangle\langle A_1| + \boldsymbol{\sigma_3}|A_2\rangle\langle A_2|\Big)\boldsymbol{\sigma_3}\Big]|A_4\rangle \\ &+ i\gamma\Big[|A_1\rangle\langle A_2^*| + |A_2\rangle\langle A_1^*| - \frac{\boldsymbol{\sigma_3}}{3}\Big(|A_1\rangle\langle A_2^*| + |A_2\rangle\langle A_1^*|\Big)\boldsymbol{\sigma_3}\Big]|A_3^*\rangle,\end{aligned} \tag{3.24}$$

where $\beta(\omega)$ is the propagation constant, $\vec{b} = \vec{b}_0(\omega_1)$, $\vec{b}_1 = (d\vec{b}_0\ /d\omega)_{\omega=\omega_1}$, and birefringence at the frequency of the second pump, signal and idler are Taylor-expanded around the frequency of the first pump. It is assumed that pumps are much stronger than the signal and idler so that their depletion is negligible. All fields are assumed to be continuous waves, so that, the time derivatives in Eqs. (2.67) and (2.68) can be dropped. As usual, the FWM equations for single-pump FOPAs can be derived by putting $|A_2\rangle = 0$ in Eqs. (3.21) and (3.22) and replacing $|A_1\rangle$ and $|A_2\rangle$ by $|A_1\rangle/\sqrt{2}$ in the signal and idler equations (3.23) and (3.24).

Fiber birefringence is taken into account through $\vec{b}_0$ and $\vec{b}_1$. FOPA gain shows different characteristics depending on the nature of the fiber birefringence. Some fibers are manufactured so that they have a large birefringence with a fixed principal axis. FWM in highly birefringent fibers is investigated in detail in Chapter 6. In practice, even nominally isotropic fibers have small amount of birefringence. Ideally, a perfectly circular fiber, free from stress or strain should be perfectly isotropic. However, this symmetry is broken inevitably during the drawing process, leading to residual birefringence. Typically, the residual birefringence is small enough that, the beat length can be as long as 10 m. The direction of the principal axes of the residual birefringence cannot be controlled and it changes randomly along the fiber at a length scale of ~ 1 m [51]. When fibers shorter than 10 m are used, fiber birefringence can be ignored, and the fiber can be assumed to be isotropic. For fibers much longer than the correlation length of residual birefringence, effects of randomly varying birefringence cannot be ignored. Dependence of FOPA gain on the polarizations of the pumps, signal and idler is investigated in the short and long length scales separately.

3.3.2 FWM in Short Fibers

In this case, fiber birefringence is completely neglected and the fiber is assumed to be isotropic. Even though the fiber does not have any birefringence, Eqs (3.21) and (3.22) show that pump SOPs may go through nonlinear polarization rotation due to SPM and XPM. It is easier to see the nature of this rotation in the Stokes space. Equations (3.21) and (3.22) can be put in a more compact from using the following identities for the Pauli spin matrices:

$$(\vec{r}\cdot\vec{\boldsymbol{\sigma}})(\vec{k}\cdot\vec{\boldsymbol{\sigma}}) = \vec{r}\cdot\vec{k}\,\boldsymbol{\sigma_0} + i(\vec{r}\times\vec{k})\cdot\vec{\boldsymbol{\sigma}}, \tag{3.25}$$

$$|A\rangle\langle B| = \frac{1}{2}\left[\langle B|A\rangle\boldsymbol{\sigma_0} + \langle B|\vec{\boldsymbol{\sigma}}|A\rangle\cdot\vec{\boldsymbol{\sigma}}\right], \tag{3.26}$$

where $\vec{r}$ and $\vec{k}$ are arbitrary vectors with three components, and $|A\rangle$ and $|B\rangle$ are arbitrary Jones vectors. Using these identities, Eqs. (3.21) and (3.22) can be written as

$$\frac{d|A_1\rangle}{dz} = i\beta(\omega_1)\vec{P}_1 + i\gamma\Bigg\{\left(P_1+\frac{3}{2}P_2\right)\boldsymbol{\sigma_0}+\frac{1}{2}\vec{P}_2\cdot\vec{\boldsymbol{\sigma}} - \frac{1}{3}\left[\left(\vec{P}_{13}+\frac{3}{2}\vec{P}_{23}\right)\boldsymbol{\sigma_0}-\frac{1}{2}\vec{P}_2\cdot\vec{\boldsymbol{\sigma}}\right]\Bigg\}|A_1\rangle, \tag{3.27}$$

$$\frac{d|A_2\rangle}{dz} = i\beta(\omega_2)\vec{P}_2 + i\gamma\Bigg\{\left(P_2+\frac{3}{2}P_1\right)\boldsymbol{\sigma_0}+\frac{1}{2}\vec{P}_1\cdot\vec{\boldsymbol{\sigma}} - \frac{1}{3}\left[\left(\vec{P}_{23}+\frac{3}{2}\vec{P}_{13}\right)\boldsymbol{\sigma_0}-\frac{1}{2}\vec{P}_1\cdot\vec{\boldsymbol{\sigma}}\right]\Bigg\}|A_2\rangle. \tag{3.28}$$

These two pump equations become even more compact if all the fields are represented in the Stokes space: [50]:

$$\frac{d\vec{P}_1}{dz} = \frac{2\gamma}{3}\left[\vec{P}_{13}-2\vec{P}_{2\perp}\right]\times\vec{P}_1, \tag{3.29}$$

$$\frac{d\vec{P}_2}{dz} = \frac{2\gamma}{3}\left[\vec{P}_{23}-2\vec{P}_{1\perp}\right]\times\vec{P}_2, \tag{3.30}$$

where $\vec{P}_k = \langle A_k|\vec{\boldsymbol{\sigma}}|A_k\rangle$, with $k = 1$ or 2, is the Stokes vector corresponding to the kth pump field. $\vec{P}_{k3}$ is the part of the Stokes vector that is along the z axis of the Poincare sphere and $\vec{P}_{k\perp}$ is the transverse part of the Stokes vector that lies on the equatorial plane (x–y plane) of the Poincare sphere. Equations (3.29) and (3.30) show that pumps rotate around their own z-component due to SPM and rotate around the transverse component of the other field due to XPM. In general, pumps rotate in a complicated manner and it is not possible to get a closed form solution to Eqs. (3.21)–(3.24).

Equations (3.29)–(3.30) show that in the special case in which both pumps are circularly polarized, they retain their input polarization states. Another special case is when both pumps are linearly polarized, with their SOPs either parallel or orthogonal. In these cases it is possible to get a simple analytical solution to Eqs. (3.21)–(3.24) which can provide sufficient insight to the polarization-dependent nature of FWM.

To get the simple analytical solution for the signal gain it is assumed that the pump, signal and idler fields are of the form $|A_k\rangle = A_k\hat{e}_k$ with $k = 1$–4, where A_k is the scalar

amplitude and $\hat{e}_k$ is the unit Jones vector that is either linearly polarized or circularly polarized. In all these cases, the equation for the pumps can be solved easily and inserted into the signal and idler equations. The signal and idler equations then take the following canonical form after an appropriate change of variables:

$$\frac{dA_3}{dz} = \frac{i}{2}\kappa A_3 + 2r_g i\gamma A_1 A_2 A_4^*, \tag{3.31}$$

$$\frac{dA_4}{dz} = \frac{i}{2}\kappa A_4 + 2r_g i\gamma A_1 A_2 A_3^*, \tag{3.32}$$

where $\kappa = \Delta\beta + r_k\gamma(P_1 + P_2)$. The polarization dependence of FWM and the phase-matching condition is reflected in r_g and r_k which take different values for different input field SOPs. Equations (3.31) and (3.32) have the same form as the scalar FWM equations Eqs. (2.77) and (2.78) shown in Chapter 2 except that FWM strength and phase-mismatch parameters are modified. The signal gain can be calculated easily to give:

$$G = \frac{\langle A_3(L)|A_3(L)\rangle}{\langle A_3(0)|A_3(0)\rangle} = \left[1 + (1 + \kappa^2/4g^2)\sinh^2(gL)\right], \tag{3.33}$$

where $g = \sqrt{(2r_g\gamma)^2 P_1 P_2 - (\kappa/2)^2}$ and values of r_g and r_k for different pump and signal input SOPs are shown in Table (3.1) [50].

The comparison of the last two columns in Table (3.1) shows that FOPA gain depends on the overall SOP of the fields. For example, even when all fields remain parallel (first row), changing all fields from linear polarization to circular polarization reduces FWM strength by a factor of $2/3$. Comparing different rows shows that, when all fields are either linearly or circularly polarized but their relative orientations change, FWM efficiency also changes. For instance, when pumps are copolarized, changing signal polarization from the parallel to the orthogonal state reduces FWM strength by a factor of $1/3$ in the case of linear polarization and leads to no gain in the case of circular polarization. In general, FWM efficiency is maximized when all fields are parallel regardless of their individual SOPs. Note also that when linearly polarized fields interact, the nonlinear contribution to the phase-matching condition also depends on the relative orientations of the fields.

SOPs		Linear		Circular	
Pumps	Signal	r_k	r_g	r_k	r_g
$\hat{e}_1 \parallel \hat{e}_2$	$\hat{e}_3 \parallel \hat{e}_1$	1	1	$2/3$	$2/3$
$\hat{e}_1 \parallel \hat{e}_2$	$\hat{e}_3 \perp \hat{e}_1$	$-5/3$	$1/3$	$2/3$	0
$\hat{e}_1 \perp \hat{e}_2$	Arbitrary $\hat{e}_3$	1	$1/3$	$2/3$	$2/3$

Table 3.1: This table summarizes the polarization dependence of nonlinear-phase mismatch and FWM strength. The first column shows the relative orientations of the pump SOPs. The second column shows the signal SOP with respect to the pump SOPs. Values of r_k and r_g are listed for the cases when all fields are linearly polarized and circularly polarized.

3.3.3 FWM in Long Fibers

In long fibers, the effects of randomly varying residual birefringence has to be taken into account. In Eqs. (3.21)–(3.24), birefringences experienced by individual fields are Taylor-expanded around the frequency of the first pump to show explicitly that fields with different frequencies experience different amounts of birefringence, depending on their detuning from the first pump. The common birefringence term $\vec{b}$ and the term that leads to frequency-dependent birefringence $\vec{b}_1$ affect the evolution of the fields in different ways. The frequency-independent part of birefringence b which is common to all fields rotate all fields at the same rate and preserve their relative orientations. In contrast, the frequency-dependent part of the birefringence rotates the SOPs of fields with different frequencies at different rates. If the signal and idler are in the form of pulses, the PMD term leads to a polarization-dependent group velocity. However, since the frequency-independent part is much larger than the frequency-dependent birefringence term ($|\vec{b}| \gg |\vec{b}_1|(\omega_k - \omega_1)$), they affect the fields at different length scales. Therefore the impact of these two terms can be studied independently. This section focuses on

the effects of fast birefringence rotations caused by $\vec{b}$. Section 4.2 investigates PMD related effects in detail.

In the absence of nonlinearity, field SOPs go through random rotations due to randomly varying birefringence. In the Stokes space, the tip of the Stokes vectors corresponding to the SOPs of the fields perform random walks on the Poincare sphere similar to a diffusion process. It has been shown that if the axis of the residual birefringence rotates randomly on a length scale shorter than the beat length, SOPs of the fields diffuse rapidly and cover the entire surface of the Poincare sphere [52], [53]. The FWM process depends on overall SOPs of the fields and occurs on a length scale of the nonlinear length defined as $1/(\gamma\sqrt{P_1P_2})$. Inside one nonlinear length, the field SOP goes through many different polarization states on the Poincare sphere. The overall efficiency of FWM is not determined by individual SOP states the field goes through, but only by their average. Averaging Eqs. (3.21)–(3.24) over the fast SOP rotations simplifies the equations considerably [54]:

$$\frac{d|A_1\rangle}{dz} = i\beta(\omega_1)|A_1\rangle + i\gamma_e\Big(P_2 + |A_1\rangle\langle A_1| + |A_2\rangle\langle A_2|\Big)|A_1\rangle, \tag{3.34}$$

$$\begin{aligned}\frac{d|A_2\rangle}{dz} &= i\beta(\omega_2)|A_2\rangle + i\vec{b}_1(\omega_2-\omega_1)\cdot\vec{\sigma}|A_2\rangle \\ &\quad + i\gamma_e\Big(P_1 + |A_1\rangle\langle A_1| + |A_2\rangle\langle A_2|\Big)|A_2\rangle,\end{aligned} \tag{3.35}$$

$$\begin{aligned}\frac{d|A_3\rangle}{dz} &= i\beta(\omega_3)|A_3\rangle + i\vec{b}_1(\omega_3-\omega_1)\cdot\vec{\sigma}|A_3\rangle \\ &\quad + i\gamma_e\Big(P_1+P_2 + |A_1\rangle\langle A_1| + |A_2\rangle\langle A_2|\Big)|A_3\rangle \\ &\quad + i\gamma_e\Big(|A_1\rangle\langle A_2^*| + |A_2\rangle\langle A_1^*|\Big)|A_4^*\rangle,\end{aligned} \tag{3.36}$$

$$\begin{aligned}\frac{d|A_4\rangle}{dz} &= i\beta(\omega_4)|A_4\rangle + i\vec{b}_1(\omega_4-\omega_1)\cdot\vec{\sigma}|A_4\rangle \\ &\quad + i\gamma_e\Big(P_1+P_2 + |A_1\rangle\langle A_1| + |A_2\rangle\langle A_2|\Big)|A_4\rangle \\ &\quad + i\gamma_e\Big(|A_1\rangle\langle A_2^*| + |A_2\rangle\langle A_1^*|\Big)|A_3^*\rangle,\end{aligned} \tag{3.37}$$

where $\gamma_e = 8\gamma/9$.

The comparison of the averaged Eqs. (3.34)–(3.37) and Eqs. (3.21)–(3.24) shows that, as a result of fast rotations, the nonlinearity of the fiber is reduced effectively by a factor of $8/9$ [52]–[54]. What is more, the averaged equations do not depend on the overall SOPs of the fields, but only on the relative orientations of the field SOPs with respect to one another. An analytical expression for the signal gain can be obtained from the averaged Eqs. (3.34)–(3.37) in the absence of the PMD term. In practice, when the frequencies of the fields are not too far from one another, the PMD term can be neglected.

It is instructive to see the nature of pump evolution in the Stokes space. Using Eqs. (3.34) and (3.35) the equations for the evolution of pump SOPs can be written in the Stokes space as:

$$\frac{d\vec{P}_1}{dz} = \gamma_e \vec{P}_2 \times \vec{P}_1, \tag{3.38}$$

$$\frac{d\vec{P}_2}{dz} = \gamma_e \vec{P}_1 \times \vec{P}_2. \tag{3.39}$$

Equations (3.38) and (3.39) show that the pump SOPs rotate around one another. As a result, even though the direction of the pump SOP changes along the fiber, the two pumps conserve their power. Another conserved quantity is the sum of the Stokes vector of the two pumps $\vec{P}_0 = \vec{P}_1 + \vec{P}_2$. In fact, the pump SOPs rotate around the common axis along $\vec{P}_0$. This has the important consequence that the right side of the pump field in Eqs. (3.34) and (3.35) remains constant along the fiber. This can be seen by noting that

$$|A_1\rangle\langle A_1| + |A_2\rangle\langle A_2| = \frac{1}{2}\left[(P_1 + P_2)\boldsymbol{\sigma_0} + (\vec{P}_1 + \vec{P}_2)\cdot\vec{\boldsymbol{\sigma}}\right], \tag{3.40}$$

where the relation given in Eq. (3.26) is used.

As the right side of the pump fields in Eqs. (3.34) and (3.35) does not depend on z, they can be integrated easily to find the following solution for the pump fields:

$$|A_1(z)\rangle = \exp\left[i\gamma_e z\left(P_2\boldsymbol{\sigma_0} + \boldsymbol{M}_0\right)\right]|A_1(0)\rangle, \tag{3.41}$$

$$|A_2(z)\rangle = \exp\left[i\gamma_e z\left(P_1\boldsymbol{\sigma_0} + \boldsymbol{M}_0\right)\right]|A_2(0)\rangle, \tag{3.42}$$

where $M_0 = |A_1\rangle\langle A_1| + |A_2\rangle\langle A_2|$. Inserting this solution into Eqs. (3.36) and (3.37), we obtain, after a change of variables, the following signal and idler equations:

$$\frac{d|B_3\rangle}{dz} = i\kappa|B_3\rangle + i\gamma_e\Big[|A_{10}\rangle\langle A_{20}^*| + |A_{20}\rangle\langle A_{10}^*|\Big]|B_4^*\rangle \tag{3.43}$$

$$\frac{d|B_4\rangle}{dz} = i\kappa|B_4\rangle + i\gamma_e\Big[|A_{10}\rangle\langle A_{20}^*| + |A_{20}\rangle\langle A_{10}^*|\Big]|B_3^*\rangle \tag{3.44}$$

where A_{10} and A_{20} stand for the input pump fields, $\kappa = \Delta\beta + \gamma(P_1 + P_2)$, and B_3 and B_4 are related to the signal and idler fields as

$$|B_k\rangle = \exp\Big\{\frac{i}{2}\Delta\beta z - \frac{i\gamma_e z}{2}\big[(P_1+P_2) + 2M_0\big] - i\beta(\omega_k)z\Big\}|A_k\rangle, \tag{3.45}$$

with $k = 3$ or 4.

The signal and idler equations (3.43) and (3.44) can be combined to obtain the following second-order differential equation for the signal [54]:

$$\begin{aligned}\frac{d^2|B_3\rangle}{dz^2} = -\kappa^2|B_3\rangle + \gamma_e^2\Big[&P_1|A_{20}\rangle\langle A_{20}| + P_2|A_{10}\rangle\langle A_{10}| \\ &+ \langle A_{10}|A_{20}\rangle|A_{10}\rangle\langle A_{20}| + \langle A_{20}|A_{10}\rangle|A_{20}\rangle\langle A_{10}|\Big]|A_3\rangle.\end{aligned} \tag{3.46}$$

This second-order differential equation for the signal field can be put into the following simple form:

$$\frac{d^2|B_3\rangle}{dz^2} = -\kappa^2|B_3\rangle + \frac{\gamma_e^2 P_1 P_2}{4}[3 + \hat{p}_1\cdot\hat{p}_2 + (\hat{p}_1+\hat{p}_2)\cdot\vec{\sigma}]|B_3\rangle \tag{3.47}$$

where, $\hat{p}_1 = \vec{P}_1/P_1$ and $\hat{p}_2 = \vec{P}_2/P_2$ are the unit vectors along the Stokes vectors of the pumps. This equation can be solved for the signal field

$$|B_3(z)\rangle = G_{F+}|B_{3\|}\rangle + G_{F-}|B_{3\perp}\rangle, \tag{3.48}$$

where $|B_{3\|}\rangle$ and $|B_{3\perp}\rangle$ are the polarization components of the input signal that are parallel and anti-parallel to the Stokes vector $\hat{p}_0 = (\hat{p}_1+\hat{p}_2)/\sqrt{2}$. In other words, $|B_{3\|}\rangle$ and $|B_{3\perp}\rangle$ are the eigenvectors of the matrix $\hat{p}_0\cdot\vec{\sigma}$. Since $\hat{p}_0$ is a real vector, $|B_{3\|}\rangle$ and $|B_{3\perp}\rangle$ define an orthogonal basis. Furthermore, G_{F+} and G_{F-} are the gains experienced by the two polarization components of the signal field and are given by

$$G_{F\pm} = \cosh(g_\pm z) + \frac{i\kappa}{g_\pm}\sinh(g_\pm z), \tag{3.49}$$

where $g_\pm$ is defined as

$$g_\pm = \sqrt{F_\pm^2 - \kappa^2}, \qquad F_\pm = F_0[1 \pm \cos(\theta_p/2)], \tag{3.50}$$

where $F_0 = \gamma_e\sqrt{P_1P_2}$, and $\theta_p = \cos^{-1}(\hat{p}_1 \cdot \hat{p}_2)$ is the angle between the Stokes vectors of the two pumps. Combining Eqs. (3.48) and (3.49), the signal gain can be written as

$$G_3(L) = \frac{G_+ + G_-}{2} + \frac{G_+ - G_-}{2}\hat{p}_0 \cdot \hat{p}_3, \qquad G_\pm = 1 + \left[\frac{F_\pm}{g_\pm}\sinh(g_\pm L)\right]^2 \tag{3.51}$$

where $G_\pm = |G_{F\pm}|^2$ and $G_3(L) = P_3(L)/P_3(0)$.

The signal gain for single-pump FOPAs can be found following the same procedure. In the case of single-pump FOPAs, the signal gain can be found from Eqs. (3.50) and (3.51) by setting, $F_0 = \gamma_e P_1/2$, $\theta_p = 0$, $\hat{p}_0 = \hat{p}_1$ and $\kappa = \Delta\beta + 2\gamma_e P_1$.

The solution for the signal gain Eqs. (3.50) and (3.51) shows that, the signal gain does not depend on the SOPs of the individual fields but only on the relative angles between them. This is expected since the SOPs of all fields rotate on a much shorter scale than the nonlinear length. Note that the phase matching condition in this case is independent of SOPs of the fields.

As the analytical solution is available for the long-length scale, the signal gain for the cases shown in Table 3.1 can be calculated easily. When the input pumps have orthogonal polarization states in the Jones space, ($\langle A_1|A_2\rangle = 0$), the Stokes vectors corresponding to the two pumps make an angle of $\theta_p = \pi$, ($\hat{p}_1 \cdot \hat{p}_2 = -1$). In this case, $F_+ = F_- = \gamma_e\sqrt{P_1P_2}$, and therefore, $G_+ = G_-$, and $\hat{p}_0 = 0$. Equation (3.51) shows that when pumps are initially orthogonal, the signal gain becomes independent of the signal SOP. Several groups have already demonstrated that dual-pump FOPAs indeed provide polarization-independent gain when orthogonally polarized pumps are used [12], [55]–[61]. Note that single-pump FOPAs cannot produce the polarization-independent gain directly.

If the two pumps are not orthogonally polarized, $\theta_p \neq \pi$, then $F_+ > F_-$ and $G_+ > G_-$. What is more, the sum of the unit Stokes vectors of the two pumps does not vanish,

$\vec{P}_0 \neq 0$. Equation (3.51) shows that, if the unit Stokes vector of signal $\hat{p}_3$ points in the same direction as $\hat{p}_0$, it experiences the largest gain $|G_+|^2$ and if it is orthogonal to this direction in the Jones space (antiparallel in Stokes space), it experiences the minimum gain $|G_-|^2$. Physically speaking, when the pumps are not orthogonally polarized, there is a preferred SOP direction for which the signal experiences maximum gain, and this direction is along $\vec{p}_0$. When the pumps are parallel, the signal experiences maximum gain when its SOP is parallel to that of pumps, which is higher by a factor of 2 on a dB scale compared to the signal gain when the pumps are orthogonal. However, if the signal the SOP is orthogonal to SOP of copolarized pumps, the signal experiences no gain at all, i.e, $G_- = 1$.

3.4 Applications and Limitations

With their high gain over a wide spectrum, FOPAs have many practical applications. Some of these applications are discussed briefly in Section 3.4.1. Because of several practical issues, their performance has limitations. Some of these limitations are introduced in Section 3.4.2.

3.4.1 Wavelength Conversion and Other Applications

Simultaneous amplification of seven channels was realized in a 2003 experiment using a single-pump FOPA made of HNLF [6]. The experiment showed that dominant degradation stems from gain saturation and FWM-induced crosstalk among channels. In another experiment, by using two CW pumps with powers of 600 mW at 1559 nm and 200 mW at 1610 nm, a gain of more than 40-dB over a 33.8-nm bandwidth was obtained inside a 1-km-long HNLF for which $\gamma = 17$ W^{-1}/km, ZDWL = 1583.5 nm, $\beta_3 = 0.055$ ps^3/km and $\beta_4 = 2.35 \times 10^{-4}$ ps^4/km. Figure 3.8 shows the data obtained from this experiment [48]. The solid curve shows the theoretical prediction. In an-

other experiment a dual-pump FOPA produced 38-dB gain with a 1.5-dB ripple over a wavelength region of more than 47 nm [49].

As discussed earlier, all FOPAs generate one or more idler waves during signal amplification. Since each idler is a phase-conjugated replica of the signal, it carries all the information associated with a signal and thus can be used for wavelength conversion. Indeed, FOPAs can act as highly efficient wavelength converters with a wide bandwidth [8]. As early as 1998, peak conversion efficiency of 28 dB was realized over a 40-nm bandwidth (full width of the gain spectrum) using a pulsed pump [9]. More recently, transparent wavelength conversion (conversion efficiency > 0 dB) over a 24-nm bandwidth (entire pump tuning range) was realized using a single-pump FOPA made with just 115 m of HNLF [62]. In a 2006 experiment wavelength conversion was realized with simultaneous 22 dB gain over a 20 nm wide wavelength range [63]. Since the created idler is a phase conjugated replica of the signal, a FOPA can be used for dispersion compensation in a fiber-optic communication system. In a 2004 experiment, a single-pump FOPA was used for phase conjugation at mid span to compensate for dispersion and fiber losses simultaneously [17].

Several experiments used dual-pump FOPAs for wavelength conversion [11], [12], [55]–[58], [64]–[67]. Using a 2.5-km-long HNLF and pumps with 0.5 W of power, a dual-pump FOPA produced 30-dB gain while converting signal bits to the idler wavelength over a 20-nm-wide wavelength range [11]. As discussed in Section 3.2, dual-pump FOPAs can produce multiple idlers at the same time. This concept was used in an experiment in 2003 to convert the signal to three different bands simultaneously [12]. Several experiments showed that using dual-pump FOPAs with orthogonally polarized pumps, polarization-insensitive wavelength conversion can be achieved [55]–[58].

The ultrafast nature of the nonlinear response of FOPAs is also useful for many practical applications. FOPAs have been used as stable sources of pulses at high repetition rates (160 Gb/s) in long-haul transmission [68], [69]. In another experiment, a transform-limited Gaussian-shape pulse train was generated at a 40-Gb/s repetition

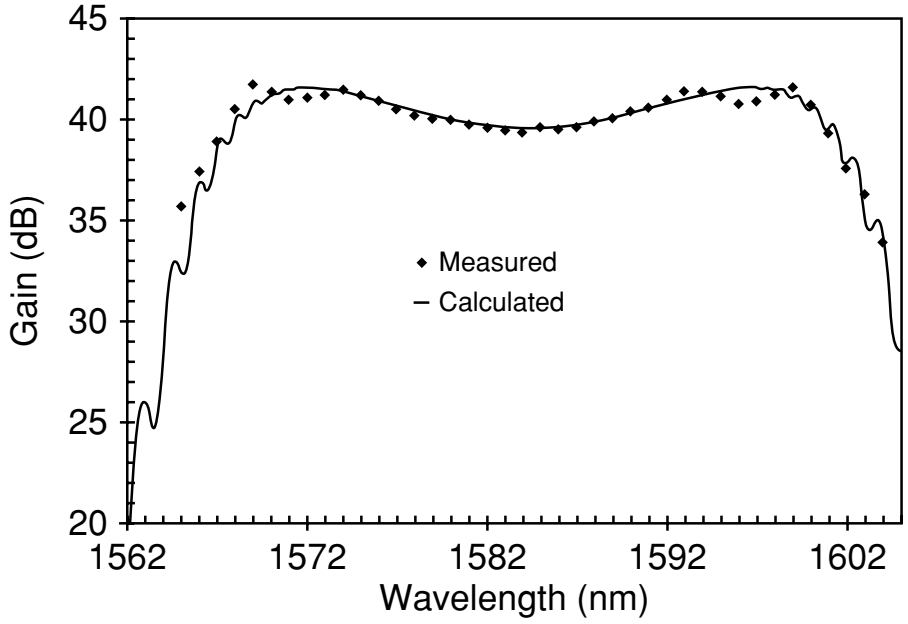

Figure 3.8: Measured (diamonds) and calculated (solid) gain spectrum as a function of signal wavelength for a dual-pump FOPA.

rate, when a weak CW signal was amplified using a FOPA whose pump power was sinusoidally modulated at 40 Gb/s [70]. Optical time-division demultiplexing from 40 Gb/s to 10 Gb/s was demonstrated [23] over a 39 nm wavelength range [24]. Another experiment used a single-pump FOPA for optical sampling at 300 Gb/s [21]. FOPAs can also be used to mitigate noise associated with an input signal when operating in the saturation regime [71]. A similar scheme can be used for all-optical signal regeneration using a higher-order idler [72], [73]. The same concept was also utilized in a dual-pump configuration [74].

FOPAs can also work in the pump-depleted region and can transfer as much as 92% of the pump power to the signal and idler fields [75]. Such FOPAs can be used to realize CW-pumped optical parametric oscillators with 30% internal conversion efficiency and a tuning range of 80 nm [76].

3.4.2 Practical Limitations

In Sections 3.1 and 3.2 the basic concepts of FOPAs were introduced after making several assumptions about FOPAs. Under such assumptions, FOPAs were predicted to provide gain bandwidths as large as 100 nm with flat gain profiles. A comparison of the predictions of the simple theory presented in Sections 3.1 and 3.2 with the experimental results discussed in Section 3.4 shows that in practice FOPAs cannot meet these expectations. For instance, the widest gain profile that has been realized so far using dual-pump FOPAs is only 47 nm wide [49], even though the simple theory of Section 3.2 predicts that it is possible to obtain 100-nm-wide gain spectrum.

In Chapter 4, I show that the imperfections of fibers do not allow for a uniform FOPA gain over a wide bandwidth, and lead to a trade off between gain uniformity and gain bandwidth. As a result, in practice, researchers have to sacrifice gain bandwidth to maintain a useful, uniform gain spectrum.

Another limitation of FOPAs that has not been discussed so far is the degradation of signal quality during amplification. In principle, FOPAs can have 3-dB noise figure which is the lowest limit for any phase-insensitive linear amplifier [18]–[20]. However, several experiments showed that, in fact, FOPAs have higher noise figures. A noise figure of 4.2 dB with a maximum gain of 27.2 dB [77] and 3.7 dB with 17-dB gain [78] have been measured for parametric amplifiers. Similarly, a noise figure of 3.8 dB with 40 dB conversion efficiency has been reported for FOPA-based wavelength converters [79] by reducing the pump noise.

In Chapter 5, I show that, because of the fast response time of FWM process and the exponential dependence of FOPA gain on the pump powers, noise associated with pumps severely distorts amplified signal. I discuss the origins of the pump noise, and the importance of walk off induced by group-velocity difference between the signal and pumps.

The discussion of Section 3.3 showed that the polarization dependence of the gain in the case of single-pump FOPAs is another limitation. In Chapter 6, I propose a simple way to achieve polarization-independent gain by using highly birefringent fibers.

A practical issue associated with dual-pump FOPAs is the Raman-induced power transfer between the two pumps [11]. As shown in Eq. (2.79), the FWM strength is proportional to $\sqrt{P_1 P_2}$ for a nondegenerate process and is maximized when the two pump powers are the same ($P_1 = P_2$). However, as the two pumps are far from each other but still within the bandwidth of the Raman-gain spectrum, stimulated Raman scattering can transfer energy from the pump of high frequency to that of low frequency. Since the two pumps cannot maintain equality in their powers along the fiber, a significant reduction occurs in the FWM efficiency even though the total power of the two pumps remains constant. To reduce this effect, the power of the high-frequency pump is chosen to be higher than that of the low-frequency pump at the input end of the fiber [48]. With this scheme, the two pump can maintain their powers close to each other over most of the fiber. Although Raman-induced pump power transfer reduces the FOPA gain by a considerable amount, it does not affect the shape of the gain spectrum since phase matching depends on the total power of the two pumps, which is conserved inside FOPA as long as the two pumps are not depleted too much.

4 Impact of Fiber Imperfections

In the previous Chapter, fibers used to make FOPAs were assumed to be free from any imperfection. However, it is difficult to realize such ideal conditions. In practice, optical fields in realistic fibers undergo random perturbations originating from imperfections within the fiber. Two such imperfections are related to random variations in the ZDWL [80] and residual birefringence along the fiber length, [51]. Both imperfections originate partly from random changes in the core size and shape. The impact of these two fiber irregularities on the FOPA gain is discussed in the following two Sections.

4.1 Fluctuations of Zero-Dispersion Wavelength

In this Section, the impact of random variations in the ZDWL of fibers is investigated for both dual-pump and single-pump FOPAs with a special attention on the uniformity of gain spectrum in the case of dual-pump FOPAs.

As seen clearly in Fig. 3.2, the gain spectrum of a FOPA is extremely sensitive to the dispersion parameters of the fiber. Changes in the ZDWL by as small as 0.1 nm change the gain spectrum considerably. Broad and flat gain spectra for dual-pump FOPAs were obtained in Section 3.2 by carefully balancing the linear and nonlinear phase mismatches, assuming that the dispersion characteristics of the fiber do not change

along the fiber. However, this is not the case in reality. Fluctuations in the core shape and size along the fiber length make the ZDWL of the fiber to change randomly. Since such perturbations typically occur during the drawing process, they are expected to have a small correlation length ($\sim$ 1 m). Long-scale variations may also cause the ZDWL to vary over length scales comparable to fiber lengths used for FOPAs [80]. In general, the ZDWL fluctuates only by a few nanometers, and the standard deviation of such fluctuations is a small fraction ($<0.1\%$) of the mean ZDWL of the fiber.

4.1.1 Numerical Simulations

In the following analysis the vector nature of the FWM process is neglected and a scalar approach is used for simplicity. The parameter space in which this simplification holds is determined in the next Section. The pump fields are much stronger than the signal and idler fields, and they are assumed to remain undepleted. This is generally the case in practice. In the case of dual-pump FOPAs, only the nondegenerate FWM process given in Eq. (2.1) is taken into account. As pointed out in Section 3.2, this process is sufficient to describe the main flat portion of the FOPA gain spectrum as long as the two pumps are located far from each other. With these simplifications, the growth of signal and idler waves is still governed by Eqs. (2.77) and (2.78). However, in the presence of random ZDWL variations along the fiber, the linear phase mismatch $\Delta\beta$ and hence κ become a random function of z; resulting in the following set of two equations:

$$\frac{dB_3}{dz} = \frac{i}{2}\kappa(z)B_3 + iFB_4^*, \tag{4.1}$$

$$\frac{dB_4}{dz} = \frac{i}{2}\kappa(z)B_4 + iFB_3^*, \tag{4.2}$$

where the FWM strength $F = 2\gamma\sqrt{P_1P_2}$ for a dual-pump FOPA and $F = \gamma P_1$ for a single-pump FOPA. The phase-mismatch parameter $\kappa(z) = \Delta\beta(\omega,z) + \gamma(P_1+P_2)$ for dual-pump FOPAs and $\kappa(z) = \Delta\beta(\omega,z) + 2\gamma P_1$ for single-pump FOPAs. The linear part of the phase mismatch $\Delta\beta$ is defined in the same way as before:

$$\Delta\beta \approx \beta_{2c}\left[(\omega_3-\omega_c)^2 - \omega_d^2\right] + \beta_{4c}\left[(\omega_3-\omega_c)^4 - \omega_d^4\right]/12, \tag{4.3}$$

where β_{2c} is defined as

$$\beta_{2c} \approx \beta_3[\omega_c - \omega_0(z)] + \beta_4[\omega_c - \omega_0(z)]^2/2, \tag{4.4}$$

$\omega_c = (\omega_1 + \omega_2)/2$ is the mean of the two pump frequencies, and $\omega_d = (\omega_1 - \omega_2)/2$ is the half of their difference. In the case of single-pump FOPA, $\omega_c = \omega_1$ and $\omega_d = 0$.

When the ZDWL is constant along the fiber, a broad gain spectrum is obtained by optimizing the FOPAs such that κ remains close to zero over a relatively broad spectral range. Random variations in the ZDWL cause β_{2c} in Eq. (4.3) to vary randomly along the fiber, and it becomes difficult to maintain $\kappa = 0$. As a result, the FOPA gain spectrum becomes considerably nonuniform even if the fiber is otherwise perfect. As FWM is sensitive to local phase mismatch, optimization of other design parameters (such as average ZDWL, pump powers and wavelengths, strength of nonlinearity, etc.) does not guarantee a uniform and wide gain spectrum when ZDWL varies randomly along the fiber even by a small amount $\sim$1 nm.

Mathematically, random ZDWL variations along the fiber render κ random and transform Eqs. (4.1) and (4.2) into two stochastic differential equations with multiplicative noise whose solution generally requires a numerical approach. To see the impact of random ZDWL fluctuations on the FOPA gain, numerical simulations are performed. FOPAs made using different fiber pieces from the same spool would exhibit different gain spectra because each corresponds to a different realization of the stochastic process. Such fiber-to-fiber variations in the gain spectra can be predicted by solving Eqs. (4.1) and (4.2) repeatedly, each time with a different random ZDWL profile. We consider a FOPA made using 500-m of high-nonlinearity fiber ($\gamma = 10$ W^{-1}/km) for which the average ZDWL is $\bar{\lambda}_0 = 1550$ nm with dispersion parameters $\beta_3 = 0.1$ ps^3/km and $\beta_4 = 10^{-4}$ ps^4/km. The dual-pump FOPA is assumed to be pumped at 1502.6 nm and 1600.6 nm with a power of 0.5 W at each wavelength. The single pump FOPA is pumped at 1550.33 nm with 1 W. Random variations of the ZDWL are modeled by dividing the fiber into a number of equal-length sections, each having a constant but

random ZDWL. In reality, the ZDWL is not constant over fixed lengths. However, when section length is short enough, it is a good approximation to fast changes. It is assumed that ZDWL fluctuations follow a Gaussian distribution with a standard deviation $\sigma_\lambda = 1$ nm and a correlation length $l_c = 5$ m. The correlation length in this model is the length over which the ZDWL is constant.

In the case of single-pump FOPAs, the scalar form of the NLS equation is solved directly rather than integrating Eqs (4.1) and (4.2) since the former method, which is more exact, turned out to be less time consuming. The scalar form of the NLS equation can be obtained from Eq. (2.54) by putting $|A\rangle = A\hat{e}$ where A is the total scalar amplitude, and $\hat{e}$ is a unit vector along a linear polarization state. By neglecting the birefringence term we get

$$\frac{\partial A}{\partial z} = -\beta_1 \frac{\partial A}{\partial t} - i\frac{\beta_2(z)}{2}\frac{\partial^2 A}{\partial t^2} - \frac{\beta_3}{6}\frac{\partial^3 A}{\partial t^3} + i\frac{\beta_4}{24}\frac{\partial^4 A}{\partial t^4} + i\gamma|A|^2 A. \tag{4.5}$$

Similar to the procedure followed in the case of dual-pump FOPAs, Eq. (4.5) is solved for each section in which the ZDWL is constant, then the resulting field is fed to the next section, which has a randomly picked ZDWL, until the end of the fiber is reached. The whole procedure is repeated for 100 different fibers all having the same average ZDWL but different ZDWL variations.

4.1.2 Numerical Results

Figure 4.1 shows the gain spectra for the dual-pump configuration for 100 realizations of the random process. The dashed curve shows the expected gain profile in the absence of ZDWL variations. It is evident that amplified signal can fluctuate over a wide range for different members of the ensemble even when $\sigma_\lambda = 1$ nm. This simulation result has two consequences. First, it is not easy to predict the gain profile based only on the average value of ZDWL of the fiber. Second, even if one goes through 100 different 1-km-length fibers chances that one of them will yield a uniform gain spectrum is very small. Such large variations in the gain spectrum would be unacceptable in practice.

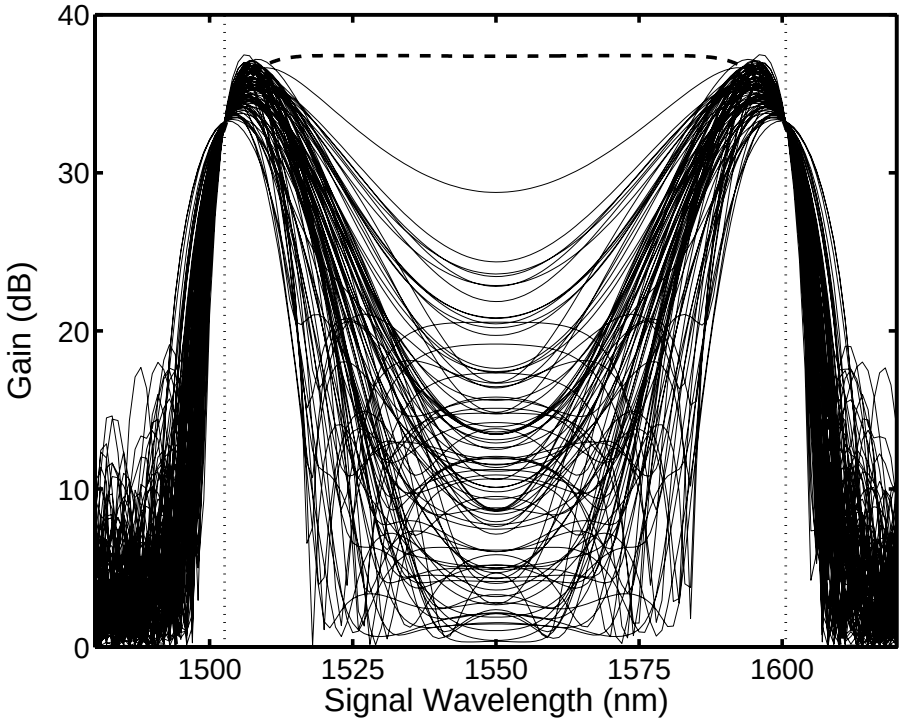

Figure 4.1: Fiber-to-fiber variations in the FOPA gain spectrum caused by random variations in ZDWL along the fiber for the pump wavelength separation of 98 nm. The dashed curve shows the gain profile in the absence of ZDWL fluctuations. Dotted vertical lines mark the locations of the pumps.

Figure 4.2 shows the result of the numerical simulations for the single-pump FOPA configuration. Each thin solid line is the gain spectrum obtained from a different fiber. The dashed line shows the optimized gain spectrum assuming that ZDWL is constant by placing the pump at 1550.32 nm. Figure 4.2 shows that fluctuation of ZDWL causes the signal gain to vary from fiber to fiber. Moreover, both the gain peak and the gain bandwidth are reduced. The portion of the gain spectrum that is farthest from the pump wavelength is the most sensitive part of the gain spectrum.

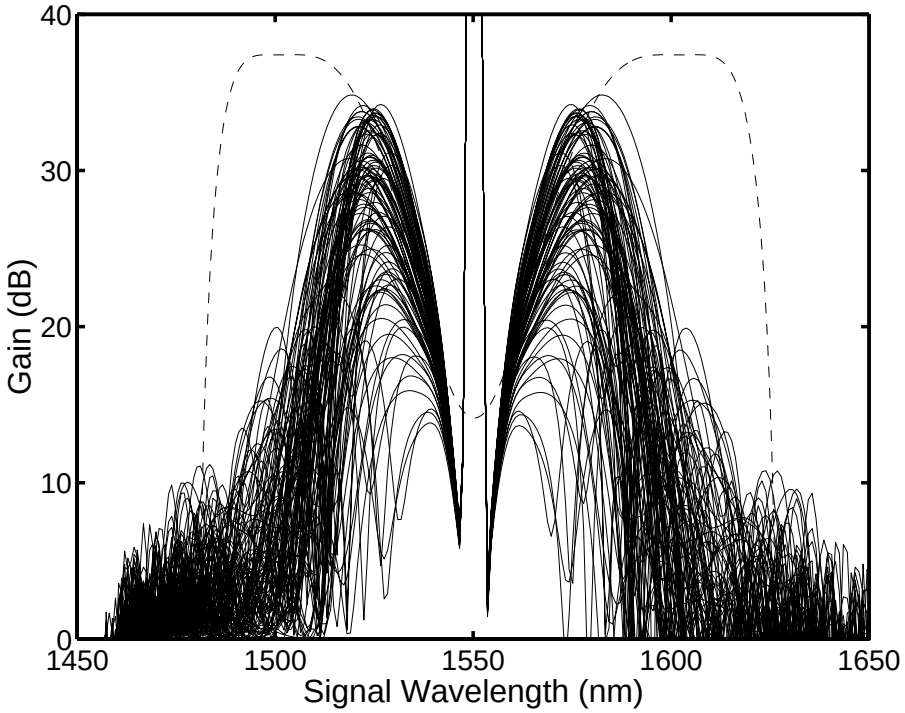

Figure 4.2: Fiber-to-fiber variations in the FOPA gain spectrum caused by random variations in ZDWL along the fiber for the single-pump FOPA. Dashed curve shows the gain profile in the absence of ZDWL fluctuations.

4.1.3 Mitigation of ZDWL Fluctuations

The important question is how FOPAs can be used in practice in spite of ZDWL variations. We have found that the impact of random ZDWL variations can be mitigated significantly by reducing the gain bandwidth. This can be achieved by reducing the wavelength separation between the two pumps and optimizing the average frequency ω_c. Figure 4.3 shows the improvement in the dual-pump case realized by changing the pump wavelengths to 1525.12 and 1575.12 nm so that the two pumps are only 50 nm apart. With this choice, the signal power fluctuates over a much reduced range. More importantly, the gain spectrum is uniform to within a few dB for each fiber over a 40-nm region between two pumps.

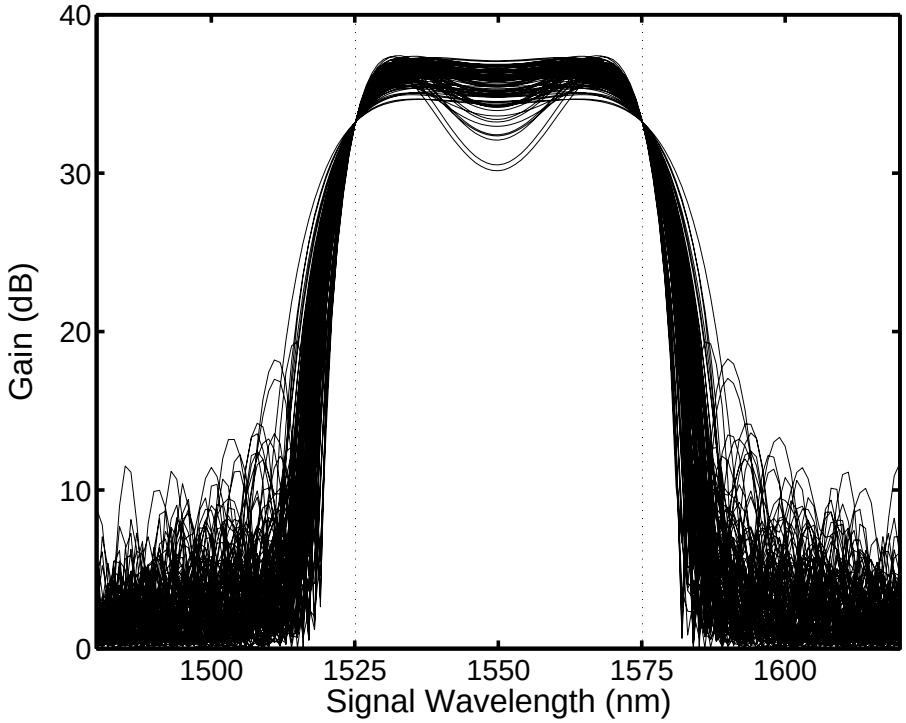

Figure 4.3: Fiber-to-fiber variations for the pump wavelength separation of 50 nm. The dotted lines show the location of the pumps.

Figure 4.4 shows the gain variations for a single-pump FOPA, when the pump wavelength is tuned from 1550.32 nm used in Fig. 4.2 to 1550.7 nm. In the absence of ZDWL fluctuations, adjusting the pump wavelength produces a narrower gain bandwidth as shown by the thick dashed line. Comparing Fig. 4.4 with Fig. 4.2 shows that when the pump wavelength is adjusted, the amount of fiber-to-fiber variations is reduced. Moreover, the gain peak is higher.

A closer look at the phase mismatch expression Eqs. (4.3) and (4.4) reveals why it is necessary to reduce the gain bandwidth to retain the gain uniformity. In these equations, ZDWL appears only through β_{2c}. When the signal wavelength is close to a pump wavelength, $\Delta\beta$ nearly vanishes regardless of the ZDWL. However, as the signal wavelength moves away, fluctuations in $\Delta\beta$ increase and become maximal when $|\omega_3 - \omega_c|$ is a maximum. Reducing the pump separation guarantees that $|\omega_3 - \omega_c|$

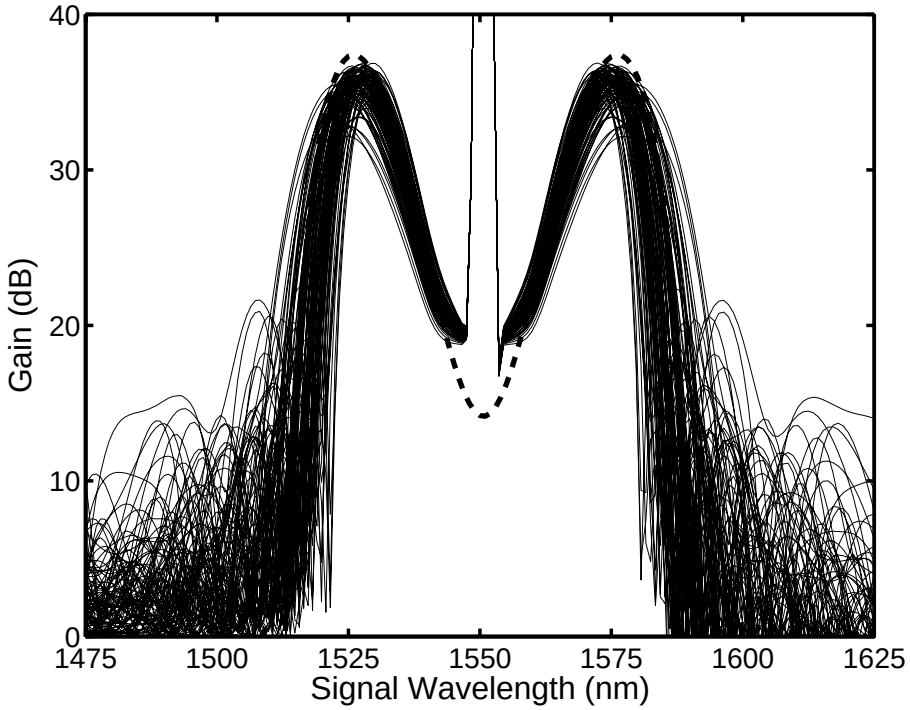

Figure 4.4: Fiber-to-fiber variations for the pump wavelength separation of 50 nm. Dotted lines show the location of the pumps.

remains small and therefore fluctuations in $\Delta\beta$ and the parametric gain can be kept below a reasonable limit. The same reasoning applies to single-pump FOPAs. However, a single-pump FOPA gain cannot be made as uniform as a dual-pump FOPA since the flat portion of the single-pump gain occurs far from the pump wavelength, and that is where the ZDWL fluctuations has the highest impact.

4.1.4 Analytical Model

A simple way to quantify the FOPA performance is to calculate the *average* gain by averaging the signal gain, $G(\omega_3) = P_3(L)/P_3(0)$, over different realizations of random ZDWL variations. Although such an "averaged" gain spectrum does not correspond to any real FOPA, it provides a good indication of the impact of ZDWL variations on FOPA performance. The average gain G_{av} can be calculated analytically when random

deviations in $\Delta\beta$ are relatively small compared with its optimum value and when the correlation length l_c is much smaller than the FOPA length [80]. In the following, the expression for G_{av} is derived and used to optimize the FOPA design. First, $\Delta\beta$ is expanded in a Taylor series as $\Delta\beta = b_a + b\delta\lambda_0$ where $b_a = \langle\Delta\beta\rangle$ and

$$b = \beta_3(2\pi c/\bar{\lambda}_0^2)[(\omega_3-\omega_c)^2-\omega_d^2]. \tag{4.6}$$

The random variable $\delta\lambda_0$ represents fluctuations in the ZDWL. It can be modeled as a Gaussian stochastic process whose first and second moments are given by [80], [82]

$$\langle\delta\lambda_0\rangle = 0, \qquad \langle\delta\lambda_0(z)\delta\lambda_0(z')\rangle = 2D_\lambda\,\delta(z-z'), \tag{4.7}$$

where $D_\lambda = \sigma_\lambda^2 l_c/2$ is the diffusion coefficient and σ_λ is the standard deviation of ZDWL fluctuations.

From Eqs. (4.1) and (4.2) the set of equations that describes the evolution of signal power can be found as

$$\frac{dP_3}{dz} = g\Gamma_i, \tag{4.8}$$

$$\frac{d\Gamma_r}{dz} = -\kappa_a\Gamma_i - b\delta\lambda_0\Gamma_i, \tag{4.9}$$

$$\frac{d\Gamma_i}{dz} = \kappa_a\Gamma_r + gP_3 - \frac{g}{2}P_3(0) + b\delta\lambda_0\Gamma_r, \tag{4.10}$$

where Γ_r and Γ_i are the real and imaginary parts of $\Gamma = B_3B_4$, $g = 4\gamma\sqrt{P_1P_2}$, and $\kappa_a = b_a + \gamma(P_1+P_2)$ represents the average phase-mismatch. Averaging Eqs. (4.8)–(4.10) over the ensemble yields

$$\frac{d\langle P_3\rangle}{dz} = g\langle\Gamma_i\rangle, \tag{4.11}$$

$$\frac{d\langle\Gamma_r\rangle}{dz} = -\kappa_a\langle\Gamma_i\rangle - b\langle\delta\lambda_0\Gamma_i\rangle, \tag{4.12}$$

$$\frac{d\langle\Gamma_i\rangle}{dz} = \kappa_a\langle\Gamma_r\rangle + g\langle P_3\rangle - \frac{g}{2}P_3(0) + b\langle\delta\lambda_0\Gamma_r\rangle. \tag{4.13}$$

In Eqs. (4.11)–(4.13), random variable $\delta\lambda_0$ and variable Γ are not statistically independent. Therefore, the averages that contain the product of these two terms cannot be

separated. In order to obtain a complete set of equations for the three average quantities of interest, $\langle P_3 \rangle$, $\langle \Gamma_r \rangle$ and $\langle \Gamma_i \rangle$, Eqs. (4.11)–(4.13) can be converted to what is known as Ito stochastic differential equations using the transformation rules explained in detail in Reference [81]. Averaging the resulting equations over ZDWL fluctuations [82], the following set of three linear equations is obtained

$$\frac{d\langle P_3 \rangle}{dz} = g\langle \Gamma_i \rangle, \tag{4.14}$$

$$\frac{d\langle \Gamma_r \rangle}{dz} = -\kappa_a \langle \Gamma_i \rangle - D_\lambda b^2 \langle \Gamma_r \rangle, \tag{4.15}$$

$$\frac{d\langle \Gamma_i \rangle}{dz} = \kappa_a \langle \Gamma_r \rangle + g\langle P_3 \rangle - \frac{g}{2} P_3(0) - D_\lambda b^2 \langle \Gamma_i \rangle. \tag{4.16}$$

The average gain $G_{av} = \langle P_3(L) \rangle / P_3(0)$ can be obtained by solving the linear equations (4.14)–(4.16) and is given by

$$G_{av} = \frac{1}{2}\left[\sum_{i=1}^{3} \frac{(g^2 + a_j a_k) e^{a_i L}}{(a_i - a_j)(a_i - a_k)} + 1 \right], \tag{4.17}$$

where $i \neq j \neq k$ and a_i are the roots of the cubic polynomial $a^3 + 2(D_\lambda b^2)a^2 + (D_\lambda^2 b^4 + \kappa_a^2 - g^2)a - D_\lambda (bg)^2$.

Figure 4.5 shows the "average" gain spectra obtained analytically (solid curves) and numerically (dashed curves). Numerical results are obtained by averaging over different realizations shown in Figs. 4.1 and 4.3. The ZDWL is assumed to follow a Gaussian distribution with $\sigma_\lambda = 1$ nm. The role of correlation length l_c is illustrated by choosing $l_c = 5$ and 50 m. In the case of a constant ZDWL (dotted curve), the gain spectrum is flat over a 80-nm bandwidth. However, variations in the ZDWL of even ± 1 nm deteriorate the flat region of the gain spectrum severely. For $l_c = 5$ m, the average gain is reduced from 38 to 18 dB in the center and varies by as much as 20 dB over the central region. For $l_c = 50$ m, a flat region reappears, but the gain is reduced from 38 to 7 dB. When $l_c = 50$ m, ZDWL fluctuations cannot be assumed to be delta-correlated. This is the reason behind the discrepancy between the analytical and numerical curves for $l_c = 50$ m.

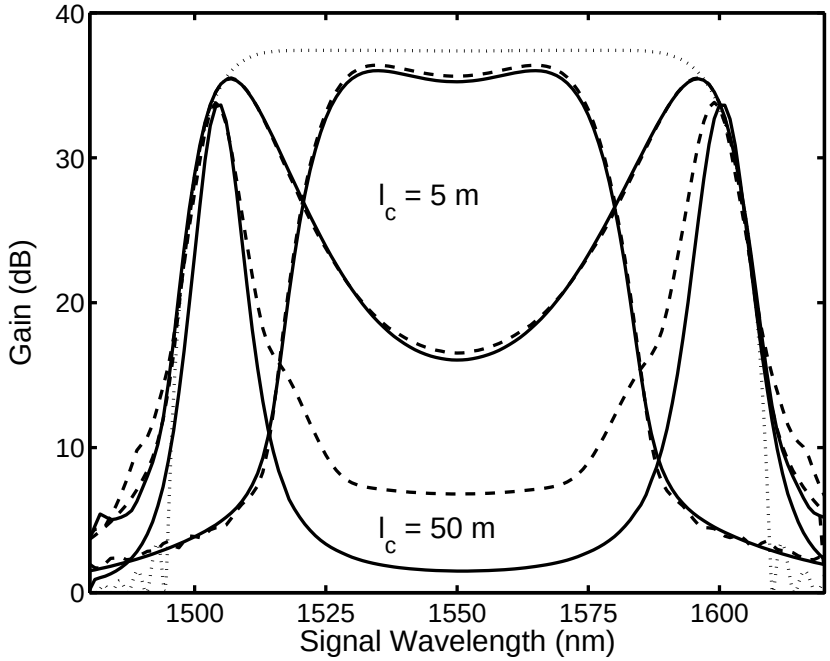

Figure 4.5: FOPA gain spectra in the case of 98-nm pump separation for two different correlation lengths $l_c = 5$ m and $l_c = 50$ m. Solid curves show the analytical prediction. Dashed curves represent an average of 100 gain spectra similar to those shown in Figs 4.1 and 4.3. The dotted curve shows the expected gain in the absence of dispersion fluctuations. The innermost curves show the average gain when pump separation is reduced to 50 nm using $\sigma_\lambda = 1$ nm and $l_c = 5$ m

The innermost solid (analytical) and dashed (numerical) curves in Fig. 4.5 show the average gain for the same FOPA when the pump separation is reduced from 98 to 50 nm. The pump wavelengths were optimized to make the gain curve as flat as possible. For this choice of pump spacing, the average gain remains nearly uniform although its bandwidth is reduced to around 40 nm and the amount of gain is reduced by about 2 dB compared with the case of a constant ZDWL. Noting from the comparison of Figs. 4.1 and 4.3 that the gain fluctuations are much smaller for 50-nm pump spacing, one arrives the conclusion that the flatness of the average gain and the variance of gain fluctuations are related, and flatness of G_{av} is a desirable design goal. This relationship is verified

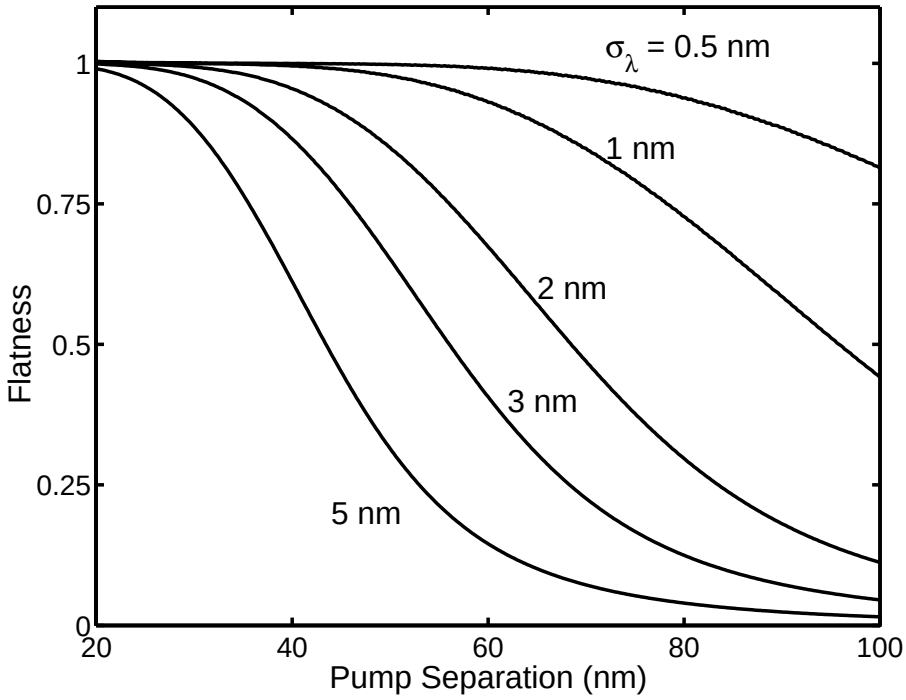

Figure 4.6: Degree of flatness plotted as a function of separation between pump wavelengths for several values of σ_λ.

through extensive numerical simulations. The main conclusion is that the effects of ZDWL variations can be mitigated significantly by reducing the pump separation in the 40–50 nm range. This conclusion is consistent with the recent experiments in which pump separation was chosen to be in this range [49], [65]. The reduced pump spacing lowers the usable FOPA bandwidth but makes its performance relatively immune to ZDWL variations.

As a further guide to dual-pump FOPA design, a measure of the flatness is introduced through a "degree of flatness" defined as $S = G_{min}/G_{max}$ where G_{min} and G_{max} are the minimum and maximum values of the average gain in the spectral region between the two pumps. Figure 4.6 shows how S varies as a function of pump-wavelength separation for different levels of ZDWL fluctuations quantified through the standard deviation σ_λ. For each point in the curves, the center pump frequency ω_c was also optimized. Because the analytical expression is valid only for $l_c \ll L$, the correlation

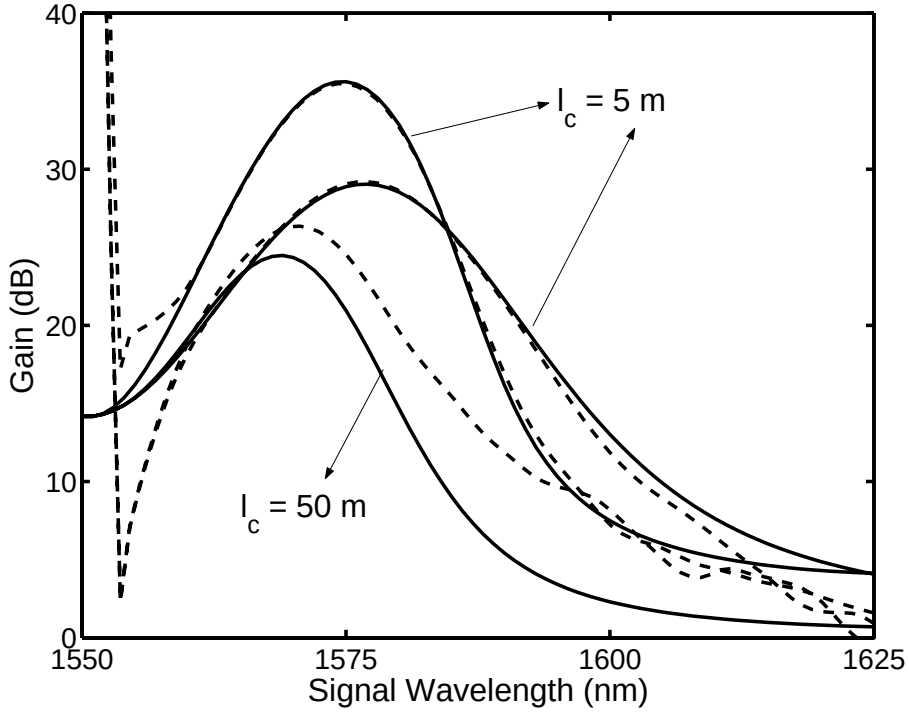

Figure 4.7: FOPA gain spectra for $\lambda_1 = 1550.33$ and $\lambda_1 = 1550.7$ nm with correlation length $l_c = 5$ m, and $\lambda_1 = 1550.33$ nm with $l_c = 50$ m. Solid curves show the analytical prediction. Dashed curves show the averages of 100 gain spectra plotted in Figs 4.2 and 4.4. Variation in ZDWL is kept at 1 nm

length was fixed at 5 m for the 500-m-long FOPA considered here; other parameters of FOPA were the same as those used in Figs. 4.1 ans 4.3. As seen in Fig. 4.6, for any value of σ_λ, it is possible to retain the flatness of the average gain spectrum as long as the pump separation is reduced below a critical value. This critical value depend on the level of ZDWL fluctuations. In particular, pump separation becomes increasingly smaller as σ_λ becomes larger to maintain the same degree of flatness. For $\sigma_\lambda = 1$ nm, the maximum tolerable pump separation is about 50 nm.

In Fig. 4.7 G_{av} for single-pump FOPAs is plotted using the analytical solution of Eq. (4.17) (solid lines) and compared to the average of different realizations obtained from Figs. 4.2 and 4.4 (dashed lines). Due to a reflection symmetry of the curves,

only one side of the gain curves is plotted. Figure 4.7 shows that the analytical result predicts the average gain very well when the correlation length is small. However, when the correlation length is large the theory overestimates the impact of ZDWL variations. Unlike the dual-pump FOPA case, it is not easy to use the average gain curve to design a FOPA that will have a relatively flat gain, unless the amount of ZDWL variations is small.

4.2 Effect of Residual Fiber Birefringence

It was shown in Section 3.3 that FWM efficiency depends on the SOPs of the interacting fields and when fibers longer than a few hundreds of meters are used, field SOPs vary randomly along the fiber length. This Section investigates how and under what conditions residual birefringence, in particular PMD, affects the gain of a dual-pump FOPA in nominally isotropic fibers.

4.2.1 Theoretical Model

The starting point is the vectorial FWM equations (2.67) and (2.68) derived in Chapter 2:

$$\frac{d|A_1\rangle}{dz} = i\beta(\omega_1)|A_1\rangle + i\vec{b}\cdot\vec{\boldsymbol{\sigma}}|A_1\rangle + i\gamma\Big[P_1+P_2+|A_2\rangle\langle A_2| - \frac{1}{3}\Big(\langle A_1|\boldsymbol{\sigma_3}|A_1\rangle + \langle A_2|\boldsymbol{\sigma_3}|A_2\rangle + \boldsymbol{\sigma_3}|A_2\rangle\langle A_2|\Big)\boldsymbol{\sigma_3}\Big]|A_1\rangle, \tag{4.18}$$

$$\frac{d|A_2\rangle}{dz} = i\beta(\omega_2)|A_2\rangle + i[\vec{b}+\vec{b}_1(\omega_2-\omega_1)]\cdot\vec{\boldsymbol{\sigma}}|A_2\rangle + i\gamma\Big[P_1+P_2+|A_1\rangle\langle A_1| - \frac{1}{3}\Big(\langle A_2|\boldsymbol{\sigma_3}|A_2\rangle + \langle A_1|\boldsymbol{\sigma_3}|A_1\rangle + \boldsymbol{\sigma_3}|A_1\rangle\langle A_1|\Big)\boldsymbol{\sigma_3}\Big]|A_1\rangle, \tag{4.19}$$

$$\begin{aligned}\frac{d|A_3\rangle}{dz} &= i\beta(\omega_3)|A_3\rangle + i[\vec{b}+\vec{b}_1(\omega_3-\omega_1)]\cdot\vec{\boldsymbol{\sigma}}|A_3\rangle \\ &+ i\gamma\Big[P_1+P_2+|A_1\rangle\langle A_1|+|A_2\rangle\langle A_2| \\ &- \frac{1}{3}\Big(\langle A_1|\boldsymbol{\sigma_3}|A_1\rangle + \langle A_2|\boldsymbol{\sigma_3}|A_2\rangle + \boldsymbol{\sigma_3}|A_1\rangle\langle A_1| + \boldsymbol{\sigma_3}|A_2\rangle\langle A_2|\Big)\boldsymbol{\sigma_3}\Big]|A_3\rangle \\ &+ i\gamma\Big[|A_1\rangle\langle A_2^*| + |A_2\rangle\langle A_1^*| - \frac{\boldsymbol{\sigma_3}}{3}\Big(|A_1\rangle\langle A_2^*| + |A_2\rangle\langle A_1^*|\Big)\boldsymbol{\sigma_3}\Big]|A_4^*\rangle,\end{aligned} \tag{4.20}$$

$$\begin{aligned}\frac{d|A_4\rangle}{dz} &= i\beta(\omega_4)|A_4\rangle + i[\vec{b}+\vec{b}_1(\omega_4-\omega_1)]\cdot\vec{\boldsymbol{\sigma}}|A_4\rangle \\ &+ i\gamma\Big[P_1+P_2+|A_1\rangle\langle A_1|+|A_2\rangle\langle A_2| \\ &- \frac{1}{3}\Big(\langle A_1|\boldsymbol{\sigma_3}|A_1\rangle + \langle A_2|\boldsymbol{\sigma_3}|A_2\rangle + \boldsymbol{\sigma_3}|A_1\rangle\langle A_1| + \boldsymbol{\sigma_3}|A_2\rangle\langle A_2|\Big)\boldsymbol{\sigma_3}\Big]|A_4\rangle \\ &+ i\gamma\Big[|A_1\rangle\langle A_2^*| + |A_2\rangle\langle A_1^*| - \frac{\boldsymbol{\sigma_3}}{3}\Big(|A_1\rangle\langle A_2^*| + |A_2\rangle\langle A_1^*|\Big)\boldsymbol{\sigma_3}\Big]|A_3^*\rangle.\end{aligned} \tag{4.21}$$

The fields are assumed to be CW so that the time dependent terms can be dropped and the birefringence parameters are defined as $\vec{b} = \vec{b}_0(\omega_1)$ and $b_1 = (d\vec{b}_0/d\omega)_{\omega=\omega_1}$. These equations constitute a set of eight scalar equations with complex coefficients, resulting in 16 real equations that need to be solved numerically.

It was shown in Section 3.3 that because of the common birefringence term $\vec{b}_0$, the SOPs of all fields rotate together on a short length scale. Because of the randomly varying birefringence axis, field SOPs perform a random walk on the surface of the Poincaré sphere. Even though this diffusion process is random, since all fields experience the same birefringence, the trajectories of the SOPs of all fields are correlated.

The PMD term, on the other hand, causes SOPs of the fields with different frequencies to rotate at different rates. In this case, trajectories of the SOPs of fields that have large frequency difference lose their correlation after some distance in the fiber. The length scale at which two fields with frequencies ω_1 and ω_2 lose their initial correlation is called the PMD diffusion length defined as [83], [84]

$$L_{\text{diff}} = \frac{3}{D_p^2(\omega_1 - \omega_2)^2}. \tag{4.22}$$

where the PMD parameter D_p is related to the variance of random variable b_1 as $D_p^2 = \langle b_1^2 \rangle l_c$ and l_c is the correlation length of the fiber birefringence. In more exact terms, L_{diff} is the length scale at which the dot product of two fields with frequencies ω_1 and ω_2 reduces by a factor of $1/e$ on the average.

In a fiber with a PMD parameter $D_p = 0.1$ ps/$\sqrt{\text{km}}$, $L_{diff} = 200$ m for two fields separated by 50 nm. Clearly, PMD induced randomization is not as fast as the frequency-independent rotations, unless the frequency difference is beyond 300 nm. It is difficult to find a case where all fields lose their correlation on a length scale much shorter than the nonlinear length. Therefore, it is not possible to average Eqs. (4.18)–(4.21) over the random rotations of SOPs of interacting fields induced by PMD as it was done in the case of frequency-independent rotations.

4.2.2 Numerical Model

In a recent study, an analytic vector theory was developed to investigate the PMD effects on FOPAs pumped at a single wavelength [85]. However, in practice dual-pump FOPAs are preferred since they provide a uniform gain over a much larger bandwidth [11], [49], [65]. Another important property of dual-pump FOPAs is that, in principle, they can eliminate the dependence of the gain on the initial SOP of the signal [12], [55]–[61]. It is difficult to extend the analytic vector theory developed for single-pump FOPAs to the case of dual-wavelength pumping because of the complexity of the problem. For this reason, numerical simulations are employed to study the impact of PMD on the

performance of such amplifiers. Two separate issues are investigated. First, how much the overall gain and its flatness are degraded because of PMD; second, whether it is possible to make FOPAs in such a way that the signal gain is independent of the signal SOP.

For numerical simulations we divide the fiber into many sections such that the amount of birefringence and the direction of principal axes are fixed in each section but vary from section to section. Each section was taken to be 5 m long. As the correlation length of birefringence fluctuations is typically $\sim$1 m, our numerical results should mimic the expected behavior. In each fiber section Eqs. (4.18)–(4.21) are solved. The fiber and pump parameters are the same as those used to produce Fig. 4.1. More specifically, we consider a 500-m-long high-nonlinearity fiber with $\gamma = 10$ W^{-1}/km pumped with two lasers, each providing 0.5 W of power. The fiber is assumed to have its zero-dispersion-wavelength at $\lambda_0 = 1.55$ μm with $\beta_3 = 0.1$ ps^3/km and $\beta_4 = 10^{-4}$ ps^4/km. The initial SOP of all fields is chosen to be linear and parallel. The pump wavelengths are chosen to obtain the most uniform gain profile in the absence of PMD and have values $\lambda_1 = 1600.6$ nm and $\lambda_2 = 1502.6$ nm.

Three parameters are enough to characterize random birefringence of the fiber leading to first-order PMD effects, namely, birefringence b of each section, the correlation length l_c and the PMD parameter D_p of the fiber. b is assumed to follow Gaussian statistics with zero mean and a standard deviation of 0.4 m^{-1} ($\delta n \approx 10^{-7}$). The random variable b_1 also follows Gaussian statistics which is determined through the PMD parameter D_p. The correlation length is equal to the length of each section ($l_c = 5$ m).

4.2.3 Results and Discussion

First, numerical simulations are used to investigate the degree to which the gain spectrum of a FOPA is degraded by PMD. For this purpose, Eqs. (4.18)–(4.21) are solved and the FOPA gain G is calculated for three different values of D_p by varying the signal

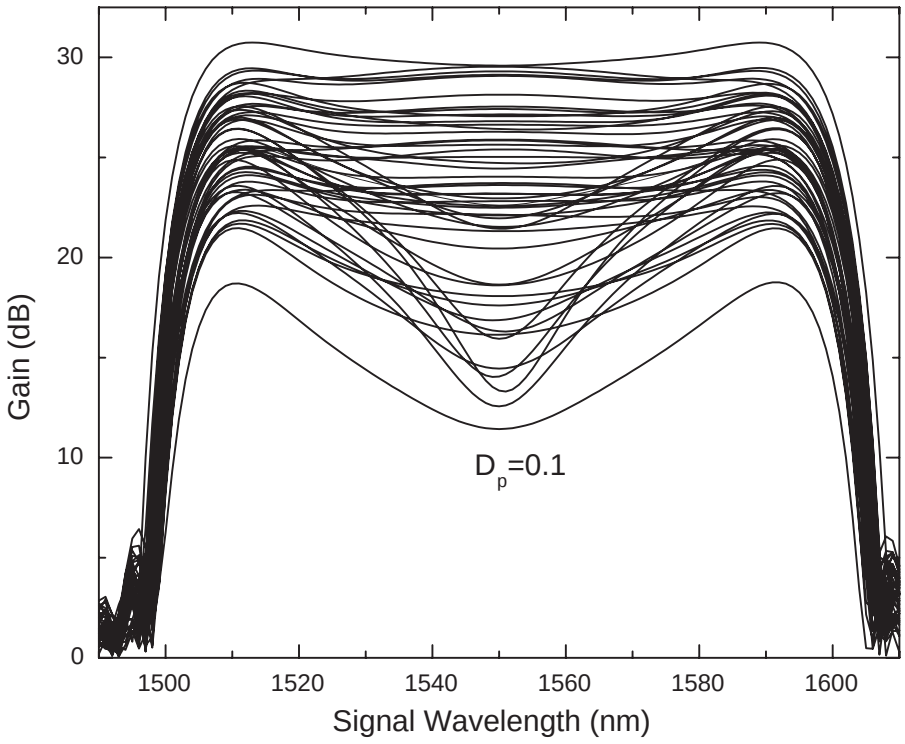

Figure 4.8: Changes in gain spectra with birefringence fluctuations for a dual-pump FOPA for $D_p = 0.1$ ps/$\sqrt{\text{km}}$. Other parameters are given in the text. Both pumps and signal are copolarized initially. Each curve corresponds to a different fiber or the same fiber measured at different times.

wavelength in the range 1.5-1.6 μm. Because of PMD, G varies over a wide range for each realization of the stochastic process. Figure 4.8 shows the range of gain fluctuations for $D_p = 0.1$ ps/$\sqrt{\text{km}}$. Variations from one gain curve to the other can be seen as fiber-to-fiber variations. They can also be the results of measurements taken at different times using the same fiber since fiber birefringence fluctuates in time, although on a long time scale of the order of minutes [86].

The average gain is found after averaging over 50 realizations shown in Fig. 4.8, for each set of parameters. The results are shown in Fig. 4.9. The ideal case of an isotropic fiber is also shown for comparison (solid curve). PMD reduces the average gain considerably and degrades the flatness of the gain spectrum appreciably for $D_p >$

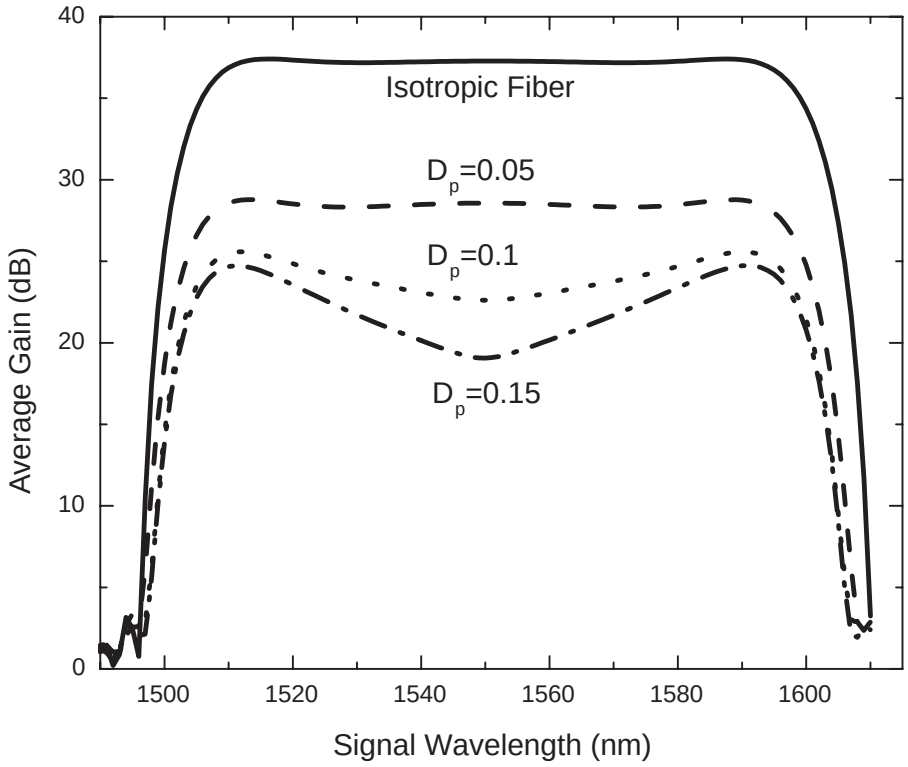

Figure 4.9: Average gain spectra for three values of PMD parameters for the same parameter values used in Fig. 4.8. Solid curve shows for comparison the no-PMD case

0.1 ps/$\sqrt{\text{km}}$. For a relatively low-PMD fiber with $D_p = 0.05$ ps/$\sqrt{\text{km}}$, the average gain is reduced by 10 dB but the spectrum remains relatively flat.

For the parameter values used in Fig. 4.9, the frequency-independent changes in the SOP (caused by b_0) can be predicted by using Eqs. (3.49) and (3.50). Comparison of FWM strength listed in Table. 3.1 and FWM strength predicted by Eq. (3.50) shows that gain is expected to reduce from its peak value of 37 dB in the absence of birefringence to 33 dB when there is only frequency-independent birefringence. Any further reduction from 33 dB represents the contribution of the frequency-dependent rotations on the Poincaré sphere and can be attributed to PMD, because of which the four fields no longer retain the initial parallel configuration of their SOPs. The larger the PMD

parameter and the larger the difference between the frequencies of two fields, the faster their SOPs deviate from each other.

For $D_p = 0.05$ ps/$\sqrt{\text{km}}$, the diffusion length for the two pumps is $L_{\text{diff}} \sim 200$ m but it reduces to 50 m for $D_p = 0.1$ ps/$\sqrt{\text{km}}$. The reason why the gain spectrum remains relatively flat in Fig. 4.9 for low PMD values is that the four fields keep their original parallel configuration for a considerable portion of the fiber. For larger values of D_p, a dip begins to form at the center of the gain spectrum. This dip can also be understood from the above argument. Since the center of the spectrum corresponds to a signal frequency that is the farthest from both pumps, the signal loses its correlation with both pumps faster and thus experiences less gain. The dip becomes deeper as D_p increases. The diffusion length L_{diff} for the signal is 780, 200, and 90 m for D_p = 0.05, 0.1, and 0.15 ps/$\sqrt{\text{km}}$, respectively. In short, the gain spectrum retain its flatness whenever the diffusion length is larger than the fiber length. For large values of D_p, the diffusion length becomes considerably shorter than the fiber length, and the spectrum degrades.

The average gain shown in Fig. 4.9 does not quantify the PMD effects completely. It is well known that PMD can fluctuate with time for any fiber depending on the environmental conditions [51], [86]. Such fluctuations will translate into signal fluctuations because the FOPA will amplify the signal by different amounts. To quantify the PMD-induced fluctuation in the signal power, Fig. 4.10 shows the ratio $\sigma/\langle G\rangle$ (both expressed in dB units) as a function of signal wavelength, where σ is the standard deviation of gain fluctuations. Although the fluctuation level is only 10% for $D_p = 0.05$ ps/$\sqrt{\text{km}}$ (± 3 dB from the average gain shown in Fig. 4.9), it exceeds 30% for $D_p = 0.15$ ps/$\sqrt{\text{km}}$ for some signal wavelengths. Such large fluctuations are unacceptable for practical applications of FOPAs.

In Figs. 4.8 to 4.10 the input SOP of the signal was kept fixed. In many system applications, it is not possible to control the SOP of the incoming signal. Since the FWM efficiency depends on the relative orientations among two pumps and the signal, fluctuations in the input signal SOP become another source of noise through polarization-

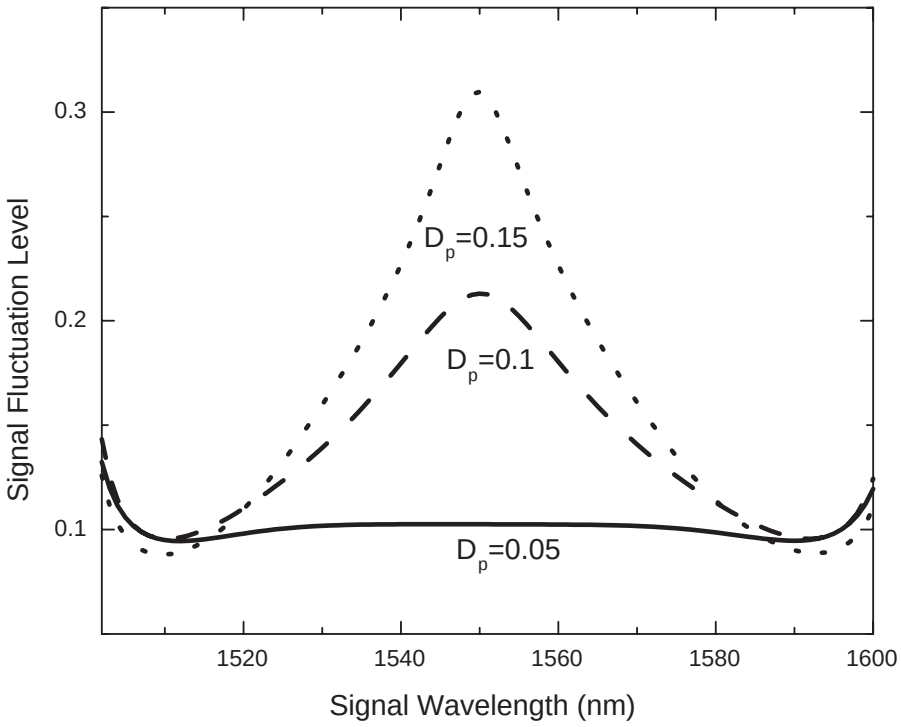

Figure 4.10: $\sigma/\langle G\rangle$ as a function of signal wavelength for three different PMD parameter values used in Fig. 2. Both σ and $\langle G\rangle$ are expressed in dB units.

dependent gain (PDG). In the case of dual-wavelength pumping, the use of linearly but orthogonally polarized pumps with equal powers can eliminate this problem. However, this scheme relies critically on the assumption that once the two pumps are launched into the fiber, they maintain their orthogonality. As discussed earlier, PMD rotates the pump SOPs at different rates such that they no longer stay orthogonal. Thus, eventually gain would depend on the input SOP of the signal, as also observed experimentally [12].

Figure 4.11 shows the results of numerical simulations for the same FOPA used for Figs. 4.8–4.10 but the pumps are now orthogonally (and linearly) polarized and $D_p = 0.1$ ps/$\sqrt{\text{km}}$. The initial SOP of the signal is linear but makes an angle of $\theta = 0, 45,$ and 90^0 from the pump at the shorter wavelength. For comparison, the gain expected in the absence of PMD effects is also included (dotted curve). For certain signal wavelengths, PDG can be as much as 12 dB, where PDG equals the dif-

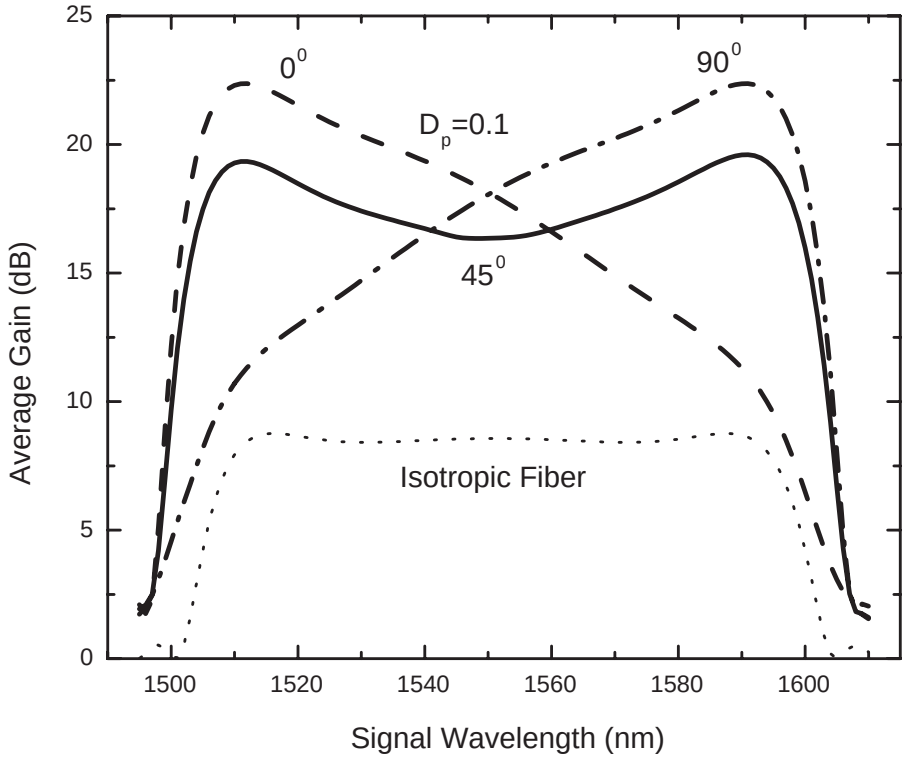

Figure 4.11: Average gain versus signal wavelength for three different initial linear SOP of the signal for $D_p = 0.1$ ps/$\sqrt{\text{km}}$; θ represents the angle in between the linear SOPS of signal and shorter-wavelength pump. The other pump is orthogonally polarized. Dotted curve shows for comparison the no-PMD case.

ference between the maximum and minimum gains as the input signal SOP is varied. The largest PDG occurs for signals close to the pumps in wavelength. The results in Fig. 4.11 agree well with a recent experiment [12]. The reason for the largest PDG to occur close to pump wavelengths can be understood in physical terms as follows. The signal with a wavelength close to one pump remains aligned with that pump but decorrelates with the other pump rapidly because of a large frequency difference. Hence, signal can see only the averaged effect of the farther pump but experiences the highest or smallest gain depending on if it started parallel or orthogonal to the closer pump. This also explains why for $\theta = 0$ gain peaks close to the pump at a shorter wavelength

and decreases as it gets closer in wavelength to the other pump. Noting that the FWM efficiency is minimum when the pumps are orthogonal, it is not surprising that the gain is minimum in the case of isotropic fiber. PMD can make the pumps nonorthogonal (and even parallel occasionally) and thus increases the gain, as seen in Fig 4.11.

4.3 Conclusions

This Section showed that fiber imperfections such as randomly varying ZDWL and PMD induced by residual birefringence constitute a major limiting factor for modern FOPAs. In particular, because of these irregularities in fibers, FOPAs cannot produce wide and uniform gain spectra.

In Section 4.1 the impact of randomly varying ZDWL on the performance of both single- and dual-pump FOPAs is investigated. It is shown that the signal gain can vary considerably from FOPA to FOPA even though all of them are made using fibers with the same zero-dispersion wavelength on average. Gain spectrum becomes highly nonuniform for a given FOPA because of such dispersion fluctuations. This problem can be solved to a large extent by reducing wavelength separation between the two pumps but at the expense of a reduced gain bandwidth. The analytical theory developed in this section shows that the maximum tolerable pump separation depends on the level of ZDWL variations within the fiber and is about 50 nm for a standard deviation of 1 nm. This explains why in most recent dual-pump FOPA experiments, pumps were kept 40 to 50 nm apart [49], [65].

In Section 4.2, the effects of PMD on dual-pump parametric amplifiers are investigated numerically. It is found that PMD induces large fluctuations in the signal power. The average gain itself is reduced by more than 10 dB even for a relatively small value of 0.05 ps/$\sqrt{\text{km}}$ for the PMD parameter. For larger values of the PMD parameter, the gain spectrum begins to distort and loses its flatness. It is also shown that PDG cannot be eliminated by using orthogonally polarized pumps and can exceed 12 dB for

$D_p = 0.1$ ps/$\sqrt{\text{km}}$. The diffusion length L_{diff} is an important design parameter. To evade the adverse effects of PMD, L_{diff} should be kept comparable to or larger than the fiber length. For a given fiber PMD, this can be achieved by keeping the pump wavelengths closer. Hence, similar to the random ZDWL variations, random residual birefringence also limits the achievable flat gain bandwidth. These results are in agreement with a recent experiment [12].

5 Pump-Induced Degradations

In Chapter 4, the effects of fiber irregularities on the FOPA performance were investigated. Effects of randomly varying ZDWL and fluctuating residual fiber birefringence were studied in the context of their impact on the FOPA gain bandwidth and gain uniformity. An equally important performance criterion for amplifiers is that they do not add too much excess noise on the amplified signal and idler fields. The excess noise is defined as the portion of the noise that is added on top of the minimum amount of noise required by quantum mechanics.

In the linear regime in which amplifier gain depends linearly on the input signal power, the minimum noise figure required by quantum mechanics depends on whether or not the amplifier gain is a function of the signal phase. Using phase-insensitive amplifiers, one cannot achieve a noise figure of less than 3 dB in the high-gain limit. However, phase-sensitive amplifiers can amplify the signal without decreasing the signal-to-noise ratio (SNR); hence they can have a 0-dB noise figure.

One may ask what the origin of 3-dB noise figure is in the case of phase-insensitive amplifiers. The answer is that the additional noise is required to prevent the violation of the Heisenberg uncertainty principle [87]. According to this principle, the real and imaginary parts of the complex amplitude of the electric field, also known as the two quadratures of the electric field, cannot be measured with arbitrary precision simulta-

neously. A phase-insensitive amplifier cannot distinguish the two quadratures, and thus amplifies them by the same amount. At the high gain limit, the two quadratures of the electric field becomes classical, and they can be measured simultaneously. The noise that leads to the 3-dB noise figure is added so that the measurement still has the same amount of uncertainty even after the fields become classical. This noise is not required when the amplifier is operated in the phase-sensitive regime since such amplifiers can amplify one quadrature while inducing loss in the other quadrature. In this case the uncertainty principle is not violated. FOPAs can operate in both phase-sensitive and phase-insensitive modes. If there is no idler at the input of the fiber, signal gain becomes independent of the phases of the input fields, and the FOPA becomes phase insensitive. A FOPA becomes phase sensitive if both the signal and idler are launched at the input.

In order for FOPAs to become practical, it is important that FOPAs do not deteriorate the SNR beyond what is dictated by the quantum limit. Therefore, it is important to identify the mechanisms through which the signal and idler SNRs may deteriorate during amplification inside a FOPA and to find methods to mitigate them. One such noise source is the perturbations associated with the pumps.

5.1 Preparation of High-Power Pumps

As discussed in Chapter 3 in detail, FOPAs require high pump power so that FWM can occur in shorter fibers resulting in a wider gain bandwidth. What is more, the pump wavelengths have to be tunable since to achieve a uniform and wide-gain bandwidth, pump frequencies have to be fine-tuned with respect to the ZDWL of the fiber. Preparation of pumps that satisfy these criteria requires multiple stages and numerous components. Figure 5.1 shows the complexity of a typical experimental setup used to make a dual-pump FOPA [48]. Single-pump FOPAs are similar except that only one pump is used.

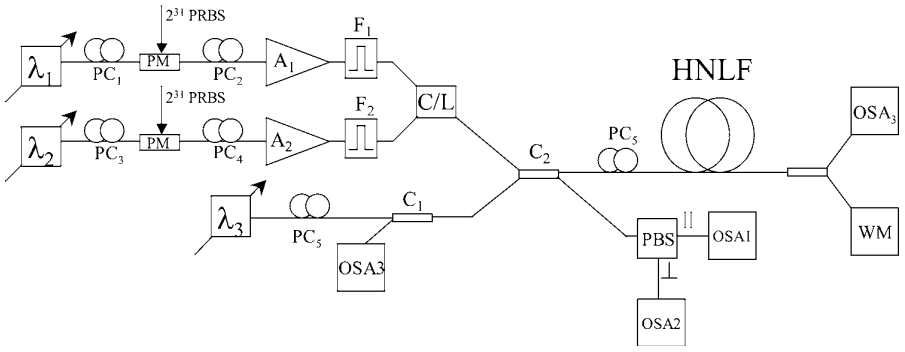

Figure 5.1: A dual-pump FOPA setup. The external cavity tunable semiconductor lasers are labeled as λ_1, λ_2 and λ_3, PC stands for polarization controller, PM is phase modulator, booster amplifiers are labeled as A_1 and A_2, F_1 and F_2 are tunable filters, OSA stands for optical spectrum analyzer and WM is for wavelength meter.

To ensure tunability, tunable external-cavity semiconductor lasers are used as CW seeds. Such sources can provide very high quality beams with a large tuning range and a narrow bandwidth but they are not powerful enough. To boost the output power to the required levels, the seed is passed through a preamplifier and a booster erbium-doped fiber amplifier (EDFA). EDFAs are commonly used as most FOPAs are built around the communication band. Amplification is done in multiple stages to increase the SNR of the pump. The amplified-spontaneous emission (ASE) noise added by the EDFAs is reduced by placing tunable optical filters (F_1 and F_2) after them. The amplified pump fields and signal field are mixed at the second coupler C_2 and launched together into the HNLF where FWM takes place. After propagating through the fiber, the pump fields are filtered. The amplified signal and idler are analyzed using an optical spectrum analyzers.

The residual ASE noise passing through the bandwidth of tunable filters, causes fluctuations in the pump power. During the FWM process, these fluctuations are transferred to the signal and idler. Since the signal (or idler) gain depends exponentially on pump powers, fluctuations transferred to the signal and idler are expected to be much higher. Note that the fast response time of the FWM process, which makes FOPAs

useful for many important applications, also helps transferring noise from the pumps to the signal efficiently. Several groups have suggested that the noise associated with the pumps is one of the dominant sources of signal SNR degradation [8], [77]–[79], [88]–[91]. Section 5.2 extends the earlier works to the case of dual-pump FOPAs and shows that the group-velocity difference between the signal and pumps has to be taken into account to determine the noise transfer correctly [92].

ASE noise added by the EDFAs is not the only source of pump perturbation. After boosting the pump power and filtering the ASE noise as much as possible, the pumps are still not ready to be launched into the fiber, because the amount of pump power that can be launched into the fiber is limited by stimulated Brillouin scattering (SBS). SBS, another third-order nonlinear process, is three orders of magnitude more efficient than the FWM process [3]. Because SBS has a narrow gain spectrum (bandwidth $<$100 MHz), it is possible to increase the SBS threshold beyond the required level of pump power by broadening the spectrum of the pumps to beyond 1 GHz. In practice, the pump spectra are broadened by modulating pump phases either sinusoidally [44] at several fixed frequencies or randomly using a pseudo-random bit pattern at bit rates of 3–10 Gb/s [48]. Even though pump-phase modulation is deterministic and cannot be considered as noise in the strict sense, it can lower the signal and idler SNR through several different mechanisms [31], [64]–[67], [93]–[97]. Sections 5.3 and 5.4 introduce two new mechanisms through which pump-phase modulation degrades the signal SNR.

5.2 Pump-Noise Transfer: Walk-off Effects

The noise-transfer problem has been studied for single-pump FOPAs [8], [90], [91]. However, these calculations ignored the walk-off effects caused by the group-velocity mismatch among the pumps, signal and idler. In this Section, it is shown that such walk-off effects have a major impact on the *relative intensity noise* (RIN) transfer. In particular, they can improve the optical SNR of the amplified signal and that of the

idler. Moreover, the analysis is extended to the case of dual-pump FOPAs as they have several advantages.

To estimate when walk-off effects become important, two time scales are introduced. First one is the coherence time τ_c of pump noise. It is related inversely to the bandwidth B_o of the optical filter used to reduce the ASE added by EDFAs. The second time scale is the walk-off delay τ_w between the signal and pumps caused by the group-velocity mismatch. This time delay can be written as

$$\tau_w = \frac{\beta_3 L}{2}|(\omega_1 - \omega_0)^2 - (\omega_3 - \omega_0)^2| \approx \frac{\beta_3 L}{2}|(\omega_1 - \omega_3)(\omega_2 - \omega_3)|, \tag{5.1}$$

where ω_0 is the zero-dispersion frequency of the fiber, β_3 is its third-order dispersion at ZDWL, and L is its length. Also, ω_1 and ω_2 are the pump frequencies and ω_3 is the signal frequency as usual. As the pumps are located almost symmetrically around the ZDWL, so are the signal and idler. Therefore, the two pumps travel at the same group velocity, and the signal and idler travel together. Hence, it is enough to consider group-velocity mismatch between one of the pumps and signal only. When $\tau_w \ll \tau_c$, averaging produced by the walk off becomes negligible. However, when τ_w is comparable to or larger than the coherence time τ_c, the signal can experience different pump powers along the fiber, resulting in an averaging over pump fluctuations.

The preceding discussion suggests that an increase in τ_w helps in reducing the FOPA noise. To increase τ_w, both β_3 and L in Eq. (5.1) should be as large as possible. Historically, these two parameters are always minimized as they limit the gain bandwidth. However as discussed in Chapter 4, the main factors limiting gain bandwidth are fiber imperfections related to random variations in the zero-dispersion wavelength [82] or/and in the residual birefringence of the fiber [84]. For instance, even if one reduces fiber length by using the so-called highly nonlinear fibers, it is not possible to increase the gain bandwidth beyond 50 nm because of fiber imperfections [48], [49]. From the standpoint of RIN transfer, the fiber length should be optimized so that it is large enough to allow the averaging of pump noise but still small enough that it does not become a limiting factor for the gain bandwidth.

5.2.1 Theoretical Model

The validity of these physical arguments is tested through extensive numerical simulations. It is found that RIN transfer in a FOPA is indeed reduced considerably when walk-off effects are included. In numerical simulations, the scalar the FWM equations, that are derived from the vectorial FWM Eqs. (2.67) and (2.68) of Chapter 2, are solved using the split-step Fourier method:

$$\frac{\partial A_1}{\partial z}+\frac{1}{v_{g1}}\frac{\partial A_1}{\partial t}+\frac{i\,d_1}{2}\frac{\partial^2 A_1}{\partial t^2}=i\beta(\omega_1)A_1+i\gamma(|A_1|^2+2|A_2|^2)A_1, \tag{5.2}$$

$$\frac{\partial A_2}{\partial z}+\frac{1}{v_{g2}}\frac{\partial A_2}{\partial t}+\frac{i\,d_2}{2}\frac{\partial^2 A_2}{\partial t^2}=i\beta(\omega_2)A_2+i\gamma(|A_2|^2+2|A_1|^2)A_2, \tag{5.3}$$

$$\frac{\partial A_3}{\partial z}+\frac{1}{v_{g3}}\frac{\partial A_3}{\partial t}+\frac{i\,d_3}{2}\frac{\partial^2 A_3}{\partial t^2}=i\beta(\omega_3)A_3+2i\gamma(|A_1|^2+|A_2|^2)A_3+2i\gamma A_1A_2A_4^*, \tag{5.4}$$

$$\frac{\partial A_4}{\partial z}+\frac{1}{v_{g4}}\frac{\partial A_4}{\partial t}+\frac{i\,d_4}{2}\frac{\partial^2 A_4}{\partial t^2}=i\beta(\omega_4)A_4+2i\gamma(|A_1|^2+|A_2|^2)A_4+2i\gamma A_1A_2A_3^*, \tag{5.5}$$

where $|A_k\rangle = A_k\hat{x}$, $k = 1$–4 are the two pump, signal, and idler fields, all linearly polarized along the x axis. $\beta(\omega_k) = \omega_k n(\omega_k)/c$ is the propagation constant, $v_{gk} = 1/\beta_1(\omega_k)$ is the group velocity, $d_k = \beta_2(\omega_k)$ is the group-velocity dispersion at the frequency of the field A_k, and $n(\omega)$ is the refractive index of the fiber. It is assumed that the pump frequencies are close enough ($|\omega_1 - \omega_2| \sim 50$ nm) that the effects of PMD induced by residual birefringence and ZDWL fluctuations can be neglected.

The pumps are assumed to be relatively noise-free before they are amplified by a factor of G_p by an EDFA. The ASE added by the EDFAs has a spectral density of $S_{ASE} = n_{sp}(\hbar\omega)(G_p - 1)$ for the pump at frequency ω, where n_{sp} is the population inversion factor [28]. The pumps are assumed to be filtered using filters with a 1-nm effective bandwidth. To calculate RIN spectra, Eqs. (5.2) through (5.5) are solved repeatedly for different ASE-noise seeds, and an ensemble average over 1000 realizations is performed numerically. The following definitions for the signal RIN, pump RIN, and

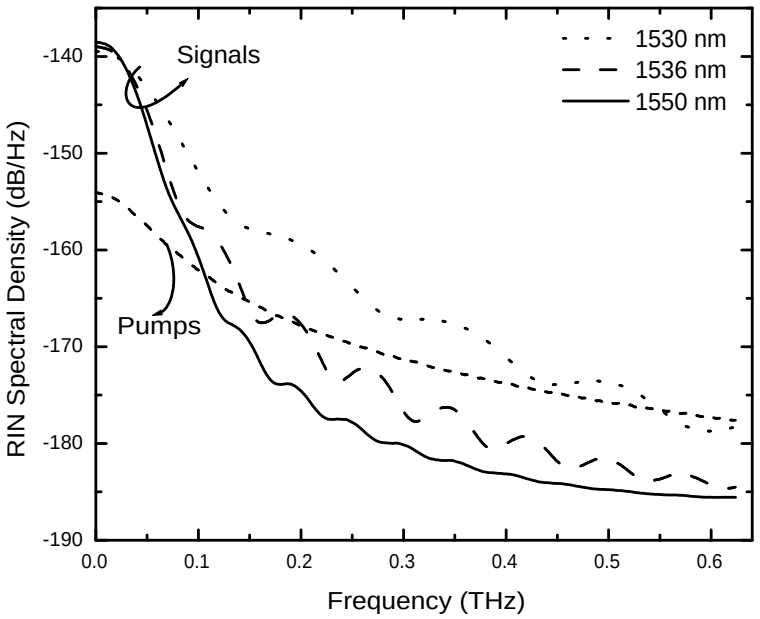

Figure 5.2: RIN spectral density as a function of noise frequency at signal wavelengths of 1530 (dotted), 1536 (dashed) and 1550 nm (solid). The short-dashed curve shows for comparison the pump RIN spectrum. The FOPA parameters used are given in the text.

the RIN enhancement factor F_r are used [28]:

$$\mathrm{RIN}_p(\omega,0) = \frac{1}{\langle P_1\rangle^2}\int_{-\infty}^{\infty}\langle \delta P_1(t)\delta P_1(t+\tau)\rangle \exp(-i\omega\tau)d\tau, \tag{5.6}$$

$$\mathrm{RIN}_s(\omega,L) = \frac{1}{\langle P_3\rangle^2}\int_{-\infty}^{\infty}\langle \delta P_3(t)\delta P_3(t+\tau)\rangle \exp(-i\omega\tau)d\tau, \tag{5.7}$$

$$F_r(\omega) = \mathrm{RIN}_s(\omega,L)/\mathrm{RIN}_p(\omega,0), \tag{5.8}$$

where $P_m = |A_m|^2$, $\delta P_m = P_m - \langle P_m\rangle$, and $\langle\cdots\rangle$ denotes ensemble averaging.

5.2.2 Results and Discussion

Figure 5.2 shows the signal RIN spectra at three signal wavelengths of 1530, 1536 and 1550 nm. The short-dashed curve shows, for comparison, the pump RIN (identical for both pumps). In all cases, a 1-km-long, highly nonlinear fiber with parameters $\lambda_0 = 1550$ nm, $\beta_3 = 0.1$ ps^3/km, $\beta_4 = 0.8 \times 10^{-4}$ ps^4/km, and $\gamma = 4.2$ W^{-1}km^{-1} were used. A lower value of γ is used to obtain 30 dB gain as the analysis ignores dispersion and fast birefringence fluctuation. The input signal is assumed to be noise-free with 10 μW of power. The pumps are located at 1525.28 and 1575.28 nm and have 0.5 W of average power after they are amplified by 27 dB by an EDFA with $n_{sp} = 1.5$. Figure 5.2 shows that the signal RIN is enhanced by 15 dB at low frequencies. However, the enhancement is reduced considerably for large frequencies, and for some frequencies, the signal RIN is even less than the pump RIN. This is because of the averaging of high-frequency noise by the walk-off effects. Because such effects are larger for signal wavelengths that are detuned farther from the pumps, the RIN spectrum is narrower and the RIN is reduced significantly when the signal wavelength is 1550 nm (solid curve).

Figure 5.3 shows the RIN enhancement factor as a function of noise frequency under the conditions of Fig. 5.2. The horizontal line on top shows for comparison the expected behavior when the walk-off effects are ignored. In the no-walk-off case, the signal RIN is 35 times larger than the pump RIN for all frequencies. When the walk-off effects are taken into account, RIN enhancement is reduced as the frequency increases and becomes nearly zero for frequencies beyond 200 GHz or so. The inset of Fig. 5.3 shows the RMS spectral width σ_R of the RIN spectrum as a function of signal wavelength by solid squares. The solid-curve fit in this inset is obtained by assuming that $\sigma_R = C/\tau_w$ where C is a fitting parameter. The good agreement reveals that the RMS width of the signal RIN is inversely proportional to the walk-off-induced delay τ_w. Signal wavelengths that are farthest from each pump have the smallest RIN because τ_w is largest for them.

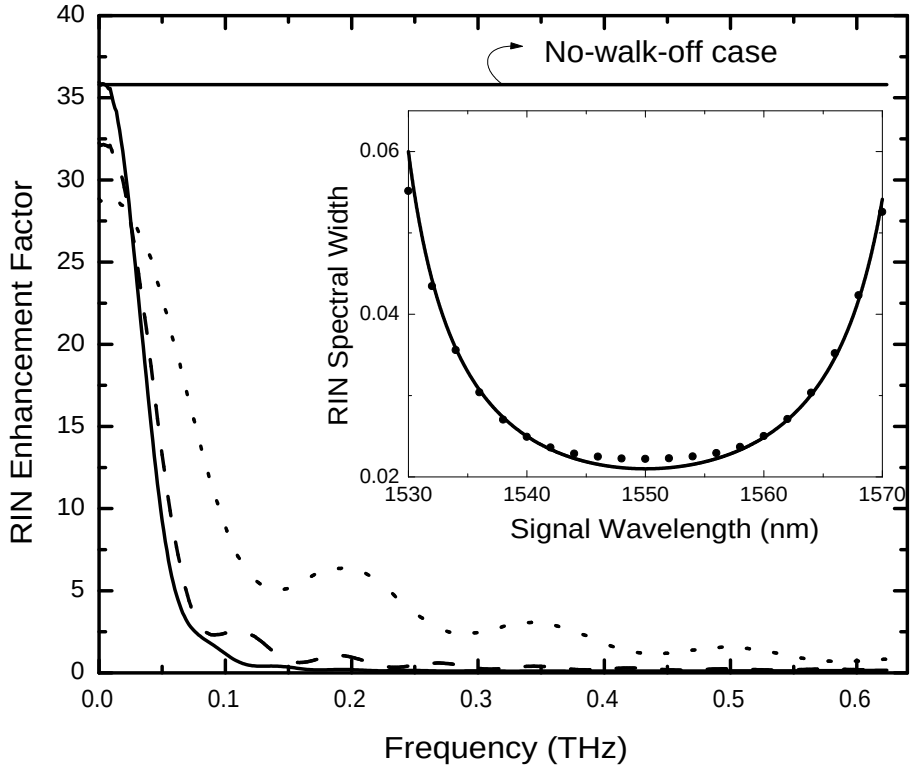

Figure 5.3: RIN enhancement factor F_r calculated for the same three signal wavelengths as in Fig. 5.2. The horizontal line shows the no-walk-off case. The inset shows the numerically calculated RMS width σ_R of the signal RIN spectrum as a function of signal wavelength (squares). The solid curve shows the fit assuming that σ_R scales inversely with the walk-off parameter τ_w.

The main effect of RIN transfer is to reduce the SNR of the amplified signal. It is expected that the SNR depends on the bandwidth of the optical filters used to reduce ASE noise. Figure 5.4 shows the optical SNR as a function of filter bandwidth for FOPA lengths of 0.5, 1 and 2 km at a fixed signal wavelength of 1555 nm. To make a meaningful comparison, the amount and the bandwidth of the FOPA gain are kept constant by keeping the product $\gamma(P_1P_2)^{1/2}L$ constant through changes in γ and by adjusting pump wavelengths by < 0.1 nm. In all cases, the amplified signal is degraded severely (SNR < 18 dB) because of RIN transfer. The best SNR is realized for the

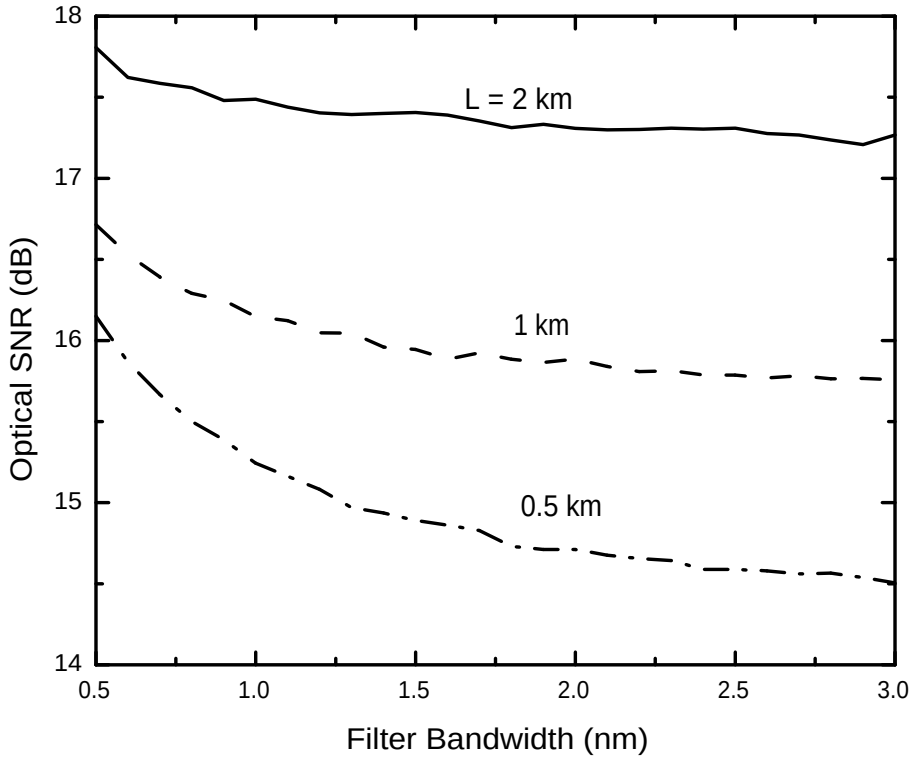

Figure 5.4: Optical SNR as a function of filter bandwidth for FOPA lengths of 0.5, 1 and 2 km. Signal is at 1555 nm. All other parameters are identical to those used for Fig. 5.2.

longest FOPA, for which SNR exceeds 17 dB and degrades only by < 0.5 dB even if filter bandwidth increases from 0.5 to 3 nm. This is easily understood from Fig. 5.4 showing that the width of RIN spectrum is determined by the inverse of the walk-off parameter. When the FOPA length is relatively short and the amount of walk off is reduced, the SNR is not only smaller but it also degrades considerably with increasing filter bandwidth. The electrical SNR of the signal, on the other hand, would not be degraded as much as the optical SNR because of a much lower bandwidth of electrical filters. In the case of a fiber with a smaller $\beta_3 \approx 0.05$ ps^2/nm, walk-off effects will be reduced by 50 %. Ideally, it is possible to increase signal and idler SNR arbitrarily by reducing the filter bandwidth. However, filter bandwidth cannot be reduced arbitrarily

because when filters with narrow bandwidths are used, they induce dispersion on the phase modulated pumps, and distort the pump power profile significantly [93].

5.3 Impact of Pump-Phase Modulation

Pump-phase modulation can affect both dual- and single-pump FOPAs in several ways. As pump phases are modulated, the instantaneous frequencies of pumps become time dependent. As discussed at the end of Section 2.7, when FOPAs are operated in the phase-insensitive mode, an idler frequency is created from the vacuum with the frequency that satisfies energy conservation. Since a FWM process requires that energy conservation among the interacting fields has to be satisfied instantaneously, $\omega_4(t) = 2\omega_1(t) - \omega_3$, the idler field is also created with time-dependent instantaneous frequency. Effectively, this causes broadening of the idler spectrum twice as much as the pump spectral broadening [31], [64]–[67].

Pump-phase modulation also affects the signal and idler gain by making the phase-matching condition time-dependent. This can be noticed easily from the expression for the phase-mismatch parameter given in Section 3.1 in Eqs. (3.8)–(3.11). As κ is a function of the pump frequency, and as pump frequency changes in time, the phase-mismatch becomes time-dependent, and hence the gain varies in time [95], [97].

These problems can be mitigated using dual-pump FOPAs and by modulating the pump phases in opposition, i.e., keeping the sum of pump phases $\phi_1(t) + \phi_2(t)$ constant at all times. In this case, $\omega_1(t) + \omega_2(t)$ also remains a constant and idler broadening can be prevented [31], [64]–[67]. As discussed in Section 3.2, the phase-mismatch parameter κ in the case of dual-pump FOPAs depends critically on the mean of the pump frequencies Eq. (3.15). When the pump phases are modulated in opposition, the mean of the pump frequencies also remains constant. As a result FOPA gain is not affected appreciably by pump-phase modulation [97].

In dual-pump FOPAs, modulating pump phases in opposition is preferred to avoid broadening of idler spectrum. However, pumps experience a relatively large dispersion inside the fiber if they are located far from the ZDWL of the fiber. As a result, during propagation inside the FOPA, phase modulation (PM) is converted into amplitude modulation (AM) through the group-velocity dispersion. Because the FOPA gain depends exponentially on the pump powers, even small changes in pump powers can cause large variations in the signal and idler powers. Such distortions of the signal and idler appear as noise when pseudo-random bit patterns are used. The SNR at the output end is then used to quantify the FOPA performance.

5.3.1 Theoretical Model

Equations governing the evolution of the pumps, signal, and idler fields can be obtained from Eqs. (5.2)–(5.5) based on the same assumptions used in the previous Section. In this case, the pumps are assumed to be free from ASE noise added by EDFAs, and time dependence of the pumps originate from the phase modulation. Equations (5.2) and (5.3) show that fiber dispersion distorts the pump fields through PM-to-AM conversion. In general, Eqs. (5.2)–(5.5) cannot be solved analytically when dispersive effects are included. However, it is possible to obtain an approximate solution with some simplifications justified for most practical dual-pump FOPA configurations. First, new variables B_k and B_j are introduced with the transformations

$$A_k = B_k \exp(i\beta(\omega_k)z + i\gamma\psi_k - i\phi_{3-k}), \tag{5.9}$$

$$A_j = B_j \exp[i(\beta(\omega_j) - \Delta\beta/2)z + 3i\gamma\psi_0/2], \tag{5.10}$$

where, $k = 1$, 2, and $j = 3$, 4. Working in a reference frame moving with the signal group velocity and introducing $\tau = t - \beta_1(\omega_3)z$ as a new time variable, Eqs. (5.2)–(5.5)

can be written as

$$\frac{\partial B_1}{\partial z} = -\delta_{13}\frac{\partial B_1}{\partial \tau} - \frac{i}{2}d_1\frac{\partial^2 B_1}{\partial \tau^2} + \gamma\left(\frac{d_1}{2}F(B_1,\psi_1) - i\delta_{13}B_1\frac{\partial \psi_1}{\partial \tau}\right), \tag{5.11}$$

$$\frac{\partial B_2}{\partial z} = -\delta_{13}\frac{\partial B_2}{\partial \tau} - \frac{i}{2}d_2\frac{\partial^2 B_2}{\partial \tau^2} + \gamma\left(\frac{d_2}{2}F(B_2,\psi_2) - i\delta_{13}B_2\frac{\partial \psi_2}{\partial \tau}\right), \tag{5.12}$$

$$\frac{\partial B_3}{\partial z} = \frac{i}{2}\kappa(z)B_3 + 2i\gamma(P_1P_2)^{1/2}B_4^* - \frac{i}{2}d_3\frac{\partial^2 B_3}{\partial \tau^2} + \gamma\frac{3d_3}{4}F(B_3,\psi_0), \tag{5.13}$$

$$\frac{\partial B_4}{\partial z} = \frac{i}{2}\kappa(z)B_4 + 2i\gamma(P_1P_2)^{1/2}B_3^* - \frac{i}{2}d_4\frac{\partial^2 B_4}{\partial \tau^2} + \gamma\frac{3d_4}{4}F(B_4,\psi_0), \tag{5.14}$$

where the function $F(B,\psi)$ is defined as $F(B,\psi) = 2B'\psi' + B\psi'' + i\gamma B(\psi')^2$, with the prime standing for a derivative with respect to τ. Only a single group-velocity mismatch parameter $\delta_{13} = \beta_1(\omega_1) - \beta_1(\omega_3)$ appears in these equations because the two pumps as well as the signal and idler pair are located almost symmetrically around the zero-dispersion wavelength [$\beta_1(\omega_1) \approx \beta_1(\omega_2)$, $\beta_1(\omega_3) \approx \beta_1(\omega_4)$].

Other quantities appearing in Eqs. (5.11) and (5.14) are defined as

$$\psi_k = \int_0^z [P_k(z') + 2P_{3-k}(z')]\,dz' \qquad \psi_0 = \int_0^z [P_1(z') + P_2(z')]\,dz', \tag{5.15}$$

$$\kappa(P_1,P_2) = \Delta\beta + \gamma[P_1(z) + P_2(z)], \qquad \Delta\beta = \beta(\omega_3) + \beta(\omega_4) - \beta(\omega_1) - \beta(\omega_2). \tag{5.16}$$

Physically, ψ_k and ψ_0 represent the nonlinear phase shifts imposed on the four fields through self- and cross-phase modulations. The parameter κ governs the total phase mismatch. Its linear part $\Delta\beta$ represents the contribution of fiber dispersion, as usual. Its nonlinear part $\gamma(P_1 + P_2)$ plays an important role because it makes κ to vary along the FOPA length if the pump powers become z-dependent.

In Eqs. (5.11) and (5.12) the functions $F(B_1,\psi_1)$ and $F(B_2,\psi_2)$ involve derivatives of the nonlinear phase shifts. These terms have their origin in the PM-to-AM conversion process discussed earlier. Physically speaking, the pump PM has to be converted to AM by dispersion of the fiber before nonlinearity of the fiber becomes important. However, the dispersion length for phase-modulated pumps is much longer (> 10 km) compared with typical FOPA lengths (< 2 km). Therefore, to a good approximation, the last

two terms in Eqs. (5.11) and (5.12) can be neglected as long as AM does not become more than 10% of initial pump powers. With this simplification, Eqs. (5.11) and (5.12) become linear equations and can be solved easily to obtain

$$B_k(z,\tau) = \int_{-\infty}^{\infty} \tilde{B}_k(0,\omega)\exp[id_k\omega^2/2 - i\omega(\tau-\delta_{13}z)]\,d\omega, \tag{5.17}$$

where $\tilde{B}_k(0,\omega)$ is the spectrum of the phase-modulated pumps at the input end of the FOPA, with $k = 1$ or 2.

A closed form solution for the pump power may be difficult to get from Eq. (5.17). However, when $|d_k|\Delta\omega_k z \ll 1$, it can be approximated to the first order as

$$P_k(z,\tau) = P_k(0)[1 + d_k z(\partial^2\phi_k(\tau)/\partial\tau^2)]. \tag{5.18}$$

where $\Delta\omega_k$ is the pump spectral bandwidth induced by PM modulation [98].

As the pumps are symmetrically positioned on opposite sides of the ZDWL, they experience the same magnitude of dispersion with opposite signs, $d_1 \approx -d_2$. What is more, $\partial^2\phi_1(\tau)/\partial\tau^2 \approx -\partial^2\phi_2(\tau)/\partial\tau^2$ since the pump phases are modulated in opposition. As a result, the amplitude modulation of the pumps is roughly same, even though their phases are modulated in opposition. In other words, powers of both pump rise and fall together. If the pump phases are modulated in the same way, i.e, $\phi_1(t) = \phi_2(t)$, the amplitude modulation induced on the pumps would have opposite direction; in the sense that when power of one pump increases the other decreases and vice versa. This would mitigate the impact of pump power variation, however, as discussed earlier, this would lead to idler spectral broadening as well as gain fluctuations.

The signal and idler equations (5.13) and (5.14) can now be tackled. As discussed earlier, the last term in the equation can be neglected. In practice, the effects of dispersion on signal and idler fields can also be ignored and one can set $d_3 = d_4 = 0$ in this equation. With these well-justified approximations, the signal and idler equations (5.13) and (5.14) can be written in the matrix form as

$$\frac{\partial}{\partial z}\begin{bmatrix} B_3(z) \\ B_4^*(z) \end{bmatrix} = \frac{i}{2}\begin{bmatrix} \kappa(P_1,P_2) & 4\gamma\sqrt{P_1(z)P_2(z)} \\ -4\gamma\sqrt{P_1(z)P_2(z)} & -\kappa(P_1,P_2) \end{bmatrix}\begin{bmatrix} B_3(z) \\ B_4^*(z) \end{bmatrix}. \tag{5.19}$$

This equation is easily solved when the pump powers remain constant along the fiber and leads to the simple solution given in Eqs. (3.12)– (3.15). However, because of PM-to-AM conversion, the pump powers become z-dependent, and in general it is not possible to integrate Eq. (5.19) analytically.

It turns out that an approximate solution can be obtained for Eq. (5.19). In practice, FOPAs are operated such that the phase-matching condition is satisfied for the average pump powers, i.e., $\kappa(\langle P_1\rangle, \langle P_2\rangle) \approx 0$. Under such conditions, $\kappa(P_1, P_2) = \gamma(\delta P_1 + \delta P_2)$, where $\delta P_k(z) = P_k(z) - \langle P_k\rangle$ and angle brackets denote time averaging. If $\delta P_k \ll P_k$, the diagonal terms of the evolution matrix in Eq. (5.19) become negligible compared with the off-diagonal terms. In physical terms, small variations in pump powers are transferred to signal and idler through changes in the FWM strength rather than through phase mismatch. With this simplification, Eq. (5.19) can be integrated to obtain the following approximate solution for the signal and idler fields:

$$B_3(L) = B_3(0)\cosh(\bar{g}L), \qquad B_4(L) = iB_3^*(0)\sinh(\bar{g}L), \tag{5.20}$$

where L is the FOPA length. The average gain $\bar{g}$ is defined as

$$\bar{g} = \frac{2\gamma}{L}\int_0^L [P_1(z, \tau - \delta_{13}z)P_2(z, \tau - \delta_{13}z)]^{1/2}\, dz, \tag{5.21}$$

where the pump power $P_k = |B_k|^2$ for $k = 1, 2$ is obtained from Eq. (5.18) for a given pump PM scheme.

5.3.2 Results and Discussion

Equation (5.21) has a simple physical interpretation. The PM-to-AM conversion process makes pump powers to vary with time in a pseudorandom fashion. These time-dependent fluctuations in pump powers get transferred to the signal and idler through the four-wave mixing process, and the net parametric gain is determined by the length-averaged quantity $\bar{g}$ in Eq. (5.21). Note that the signal and idler interact with different temporal regions of the pumps at different locations of the fiber because of the walk-off

effects induced by group-velocity mismatch. As a result, Eq. (5.21) can also be seen as a temporal averaging that reduces the extent of signal and idler fluctuations if the walk-off between the signal and the pumps is large enough.

To make further progress, a specific shape for PM profile has to be assumed. If the *nonreturn-to-zero* (NRZ) format is employed, the phase remains constant except near the leading and trailing edges. To get a closed form solution, it is assumed that the leading edges follow a raised-cosine shape, i.e., $\phi(\tau) = \pi[1-\cos(\pi\tau/T_r)]/2$ where $0 < \tau < T_r$. Using Eqs. (5.18) and (5.21) with $T_w \equiv \delta_{13}L$, the following expression is obtained for $\bar{g}(\tau)$ near each leading edge:

$$\bar{g} = 2\gamma\sqrt{P_1(0)P_2(0)}\Big[L + \frac{\pi\beta_{21}L^2}{T_w^2}\left(\cos[\frac{\pi}{T_r}(\tau - T_w)] - \cos[\frac{\pi}{T_r}\tau] - \frac{\pi T_w}{T_r}\sin[\frac{\pi}{T_r}(\tau - T_w)]\right)\Big]. \tag{5.22}$$

A similar approach is used to find $\bar{g}$ near the trailing edges. In the absence of walk-off effects ($T_w \Rightarrow 0$), changes in $\bar{g}$ scales with fiber length as L^2 and with rise time as T_r^{-2}.

To test validity of the approximate solution in Eq. (5.20), a number of numerical simulations are performed for a FOPA using realistic parameters and the results are compared with the analytical expressions. To make the PM profile realistic, filtered "rect" functions are used to simulate the NRZ bit stream. A 1-km-long fiber with its zero-dispersion wavelength at 1556 nm and $\gamma = 10$ W^{-1}/km is considered. Other fiber parameters, taken from [99], are $\beta_3 = 0.049$ ps^3/km (dispersion slope = 0.03 ps/nm^2/km), and $\beta_4 = -5.810^{-5}$ ps^4/km. The two pumps are located at 1531 and 1581 nm and are launched with 150 mW of power at the input end. The signal is launched with 0.1 μW of power at 1557 nm. With these parameters, the FOPA provides a gain of 20 dB in the spectral region located between the two pump wavelengths.

In the numerical simulations phases were modulated using a pseudorandom bit stream of NRZ pulses at a bit rate of 10 Gb/s. Figure 5.5(a) shows the modulated phase profile of one of the pumps for a duration of 6 bits. Figure 5.5(b) shows how $P_1/\langle P_1\rangle$ (or $P_2/\langle P_2\rangle$) varies as a function of time after propagation through the fiber.

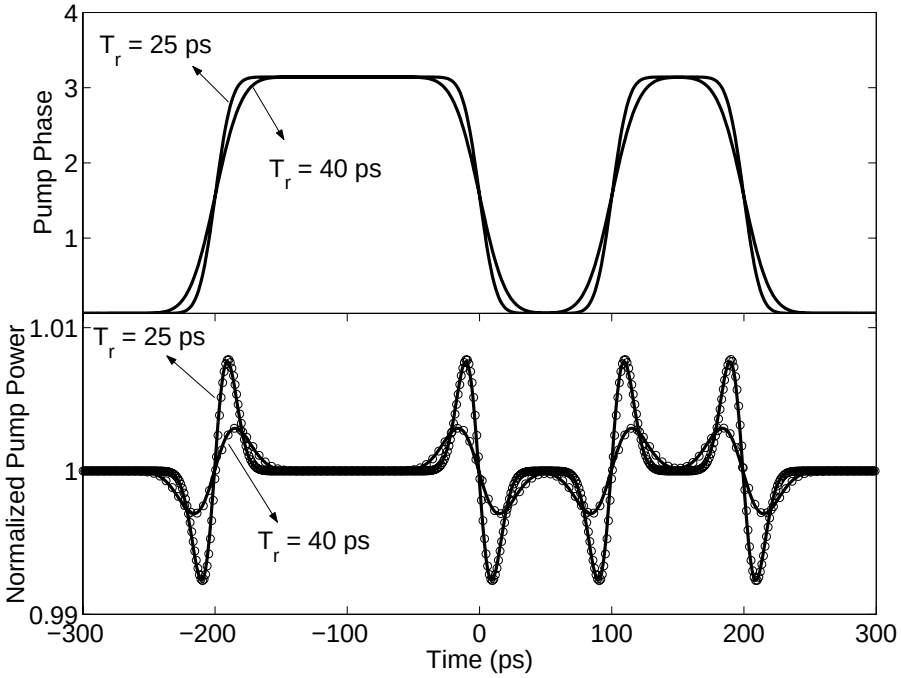

Figure 5.5: (a) Modulated pump phase over a duration of 6 bits at 10 Gb/s. (b) Normalized pump power as a function of time. Numerical results (circles) are also shown for comparison.

Solid lines represent the analytical predictions and circles show the numerical results. The effect of different rise times is shown by using $T_r = 25$ and 40 ps. The rise time T_r is defined as the time during which pump phases change from 10 to 90% of their peak value. It is clear from Fig. 5.5 that pump powers are distorted at the locations where pump phases change rapidly. A shorter rise time ($T_r = 25$ ps) increases the level of distortion significantly.

Figure 5.6 shows temporal variations in the normalized signal power $P_3/\langle P_3\rangle$ after amplification in the same time window used for Fig. 5.5. Similar variations occur at the idler wavelength. Comparison of Figs. 5.5(b) and 5.6 shows that variations in the signal power follow pump variations and are enhanced considerably by the FWM process. The agreement between the analytical theory and numerical simulations is excellent.

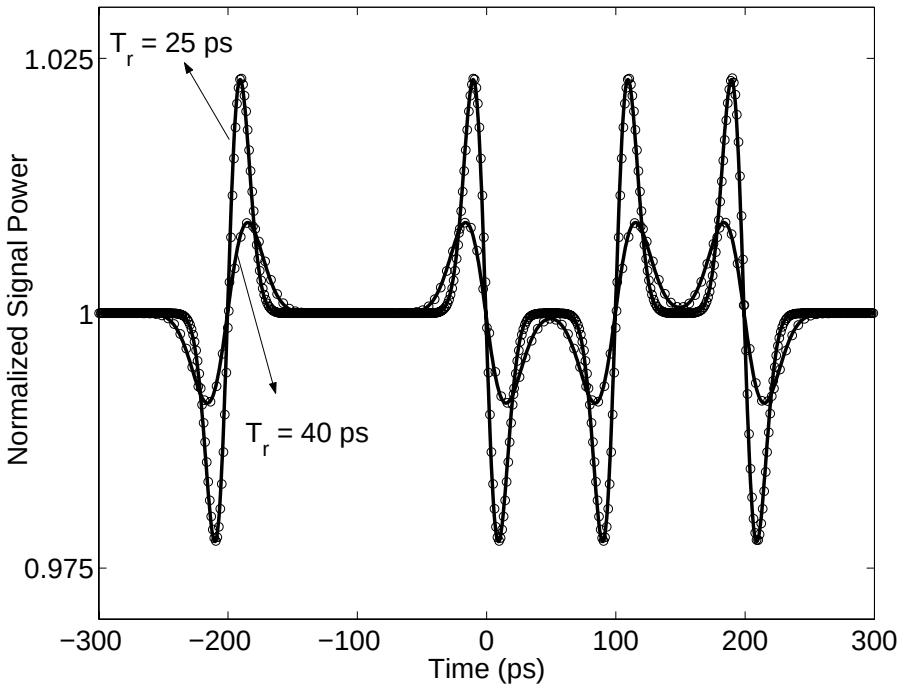

Figure 5.6: Normalized signal power as a function of time at the FOPA output.

In most cases, the curves are indistinguishable, justifying the approximations made in deriving Eq. (5.21).

To quantify the extent of degradation induced by PM-to-AM conversion, signal SNR defined as $\langle P_3 \rangle / \sigma_3$ is used where $\sigma_3^2 = \langle (P_3(t) - \langle P_3 \rangle)^2 \rangle$ is the variance of signal fluctuations. Figure 5.7 shows the signal SNR as a function of bit rate for different rise times. The SNR values obtained in the absence of walk-off effects ($\delta_{13} = 0$) are shown by dashed lines for comparison. FOPA parameters are the same as those used for Fig. 5.5. Clearly, signal SNR decreases rapidly as the bit rate of PM is increased. The SNR also depends on rise time and it becomes < 23 dB even for a relatively small gain of 20 dB, if NRZ pulses with a short rise time ($T_r \leq 25$ ps) are employed. The situation is worse for FOPAs with higher gains; a 40 dB gain will reduce the SNR below 20 dB.

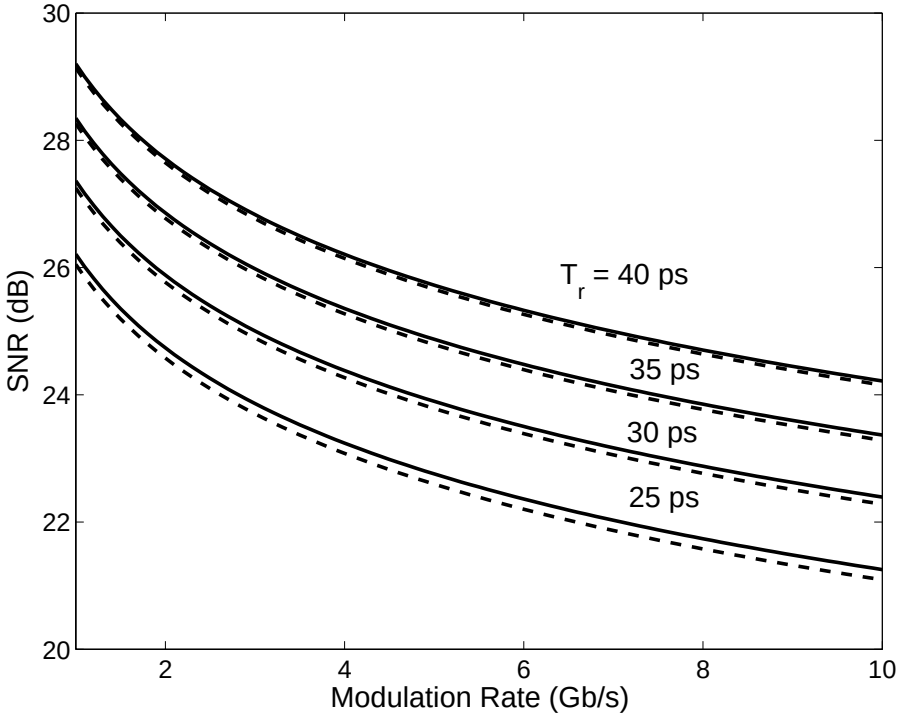

Figure 5.7: Signal SNR as a function of PM bit rate for $T_r = 25$ to 40 ps. Dashed curves show the SNR without the walk-off effects.

5.4 Impact of Component PMD and PDL

In Section 5.3, it is shown that the pump-phase modulation degrades the signal and idler SNR because it is converted to amplitude modulation by fiber dispersion. The fiber is not the only component that can convert pump-phase modulation to amplitude modulation. As it is discussed in Section 5.1, after pump phases are modulated, pumps have to go through numerous components before they enter the fiber. As a result, pump-phase modulation can be converted to amplitude modulation, as well as SOP modulation, before the pumps even enter the fiber.

This Section introduces a new mechanism through which polarization-mode dispersion (PMD) and polarization-dependent loss (PDL) associated with various optical components distort the pump fields and thus degrade the amplified signal and

idler beams at the FOPA output. Dispersion-like distortion of a time-dependent signal through PMD and PDL has been studied before in the context of telecommunication systems [100] and erbium-doped fiber amplifiers [101].

In simplest terms, PMD has its origins in the dependence of birefringence-induced phase shifts on frequency. PMD rotates the state of polarization (SOP) of optical fields with different frequencies at different rates. Equivalently, the two polarization components of a pulse travel with different group velocities such that the pulse disperses in time [51], [83], [100]–[102]. An optical component with PDL attenuates the two polarization components of a field by different amounts [100]. The combination of PMD and PDL affects both the power and the SOP of an optical field. Their combined impact is aggravated further by the fact that the birefringence magnitude as well as the orientation of the principal axes of some optical components may vary in time because of environmental changes [51], [86]. As a result, it may not be possible to arrange these components to minimize the PMD and PDL effects without using complex feedback mechanisms.

Consequences of PMD and PDL for a FOPA are two-fold. First, the SOPs of the pumps do not remain constant in time. Because the gain of the FOPA depends on the SOPs of its pumps, the gain also varies in time. Second, the pump powers are clipped by the components exhibiting PDL, causing them to vary in time. Even though such changes in the pump SOPs and powers are relatively small, they affect the FOPA gain significantly because this gain depends exponentially on the powers and SOPs of the pumps. In the absence of pump-phase modulation, such variations in the pump SOP and power would be only as fast as random variations in the PMD and PDL of the optical components (on the time scale of a few minutes to hours) [86]. However, as pump phases are modulated to suppress SBS, PMD and PDL can lead to signal fluctuation on a time scale ~ 1 ns. Physically speaking, the instantaneous frequencies of the pumps vary in time at the rates at which pump phases are modulated. As the pumps pass through a component with PMD, their SOPs become time dependent on the same

scale because PMD rotates different frequency components of pumps at different rates. A PDL component following the PMD component attenuates the pump by different amounts at different times. As a result, the pumps entering the FOPA have, in practice, SOPs and powers that change with time at the rate of phase modulation.

In Section 5.4.1 the concept of effective PMD and PDL vectors are introduced. An expression for the pump powers at the input end of the FOPA in terms of the effective PMD and PDL vectors are derived in Section 5.4.2. This expression is used in Section 5.4.3 to find the FOPA gain in terms of the effective PMD and PDL vectors. Section 5.4.4 focuses on temporal changes in the signal power produced by PMD and PDL when pump phases are modulated. In Section 5.4.5, a simple solution is proposed for minimizing the impact of PMD and PDL on the FOPA performance.

5.4.1 Effective PMD and PDL Vectors

In the frequency domain, the action of an optical component exhibiting PMD on an optical field at frequency ω can be described in the Jones space as [100]

$$|A_{out}(\omega)\rangle = \boldsymbol{U}(\omega)|A_{in}(\omega)\rangle, \qquad \boldsymbol{U}(\omega) = e^{-\frac{i}{2}\omega\vec{b}(\omega)\cdot\vec{\sigma}} \tag{5.23}$$

where the vector $\vec{b}(\omega) = [b_1(\omega), b_2(\omega), b_3(\omega)]$ is the PMD vector of the optical component in the Stokes space and $\vec{\sigma} = [\sigma_1, \sigma_2, \sigma_3]$ is the Pauli spin vector with components as defined in Eq. (2.40) [3] Note that $\vec{b}\cdot\vec{\sigma}$, defined as $b_1\sigma_1 + b_2\sigma_2 + b_3\sigma_3$, is a 2×2 matrix. The PMD vector $\vec{b}(\omega)$ is, in general, frequency dependent; the first term in the expansion of $\vec{b}(\omega)$ is conventionally referred to as the first-order PMD. The PMD vector points in the direction of the fast axis in the Stokes space. Its magnitude b provides the relative delay between the polarization components of the field that are parallel and anti-parallel to the PMD vector.

The transfer matrix $\boldsymbol{T}$ of a component exhibiting PDL is not unitary. The optical field after passing through such a component can be written as [100]

$$|A_{out}(\omega)\rangle = \boldsymbol{T}|A_{in}(\omega)\rangle, \qquad \boldsymbol{T} = e^{-\mu}e^{\vec{\mu}\cdot\vec{\sigma}} \tag{5.24}$$

where $\vec{\mu}$ is the PDL vector with magnitude μ. In this representation of the PDL matrix, the polarization component of a field that is parallel to $\vec{\mu}$ experiences no loss but the anti-parallel component is attenuated by $\exp(-2\mu)$. Such a PDL component is said to have a PDL of $10\log_{10}[\exp(4\mu)]$ in decibel units [100]. Some components used to prepare FOPA pumps may also exhibit polarization-dependent gain (such as erbium-doped fiber amplifiers [101]). Their effect is equivalent to that of a polarization-independent gain followed by a PDL component.

In general an optical component may exhibit some degree of PMD and PDL at the same time. Calculating the total transfer matrix of a large number of such components becomes quite complicated. However, noting that any matrix $\boldsymbol{M}$ can be decomposed into a unitary matrix and a positive Hermitian matrix in the form $\boldsymbol{M} = \boldsymbol{T}\boldsymbol{U}$, modelling of such a system can be simplified without loss of generality. More specifically, one can assume that the pump passes through only two components, the first one having only PMD with a transfer matrix $\boldsymbol{U}$ and the second one having only PDL with a transfer matrix $\boldsymbol{T}$ [100]. In addition, it can be assumed that all polarization-independent changes on the pumps, such as phase modulation and amplification, occur before the PMD and PDL components. Note that the PMD and PDL represented by the matrices $\boldsymbol{U}$ and $\boldsymbol{T}$ are not the same as the PMD and PDL vectors of any individual component, or a simple combination of those [100].

5.4.2 Stokes Vector of the Pump After PMD and PDL

Distortion of the pump field after going through the components that have PMD and PDL can be calculated using the concept of effective PMD and PDL vectors introduced in the previous Section. The following well-known identities related to the Pauli spin

vector are used in the rest of the derivation [102]:

$$(\vec{r}\cdot\vec{\sigma})(\vec{k}\cdot\vec{\sigma}) = \vec{r}\cdot\vec{k}\,\sigma_0 + i(\vec{r}\times\vec{k})\cdot\vec{\sigma} \quad (5.25)$$

$$(\vec{r}\cdot\vec{\sigma})\vec{\sigma}(\vec{r}\cdot\vec{\sigma}) = 2\vec{r}(\vec{r}\cdot\vec{\sigma}) - r^2\vec{\sigma} \quad (5.26)$$

$$e^{\vec{r}\cdot\vec{\sigma}} = \cosh(r)\,\sigma_0 + \sinh(r)\tilde{r}\cdot\vec{\sigma} \quad (5.27)$$

where $\vec{r}$ and $\vec{k}$ are complex valued vectors with $r^2 = \vec{r}\cdot\vec{r}$ and $\tilde{r} = \vec{r}/r$.

The pump field before entering the PMD and PDL components has the form

$$|A_{in}(t)\rangle = \sqrt{P}e^{i\phi(t)}|a_{in}\rangle \quad (5.28)$$

where P is the pump power after amplification, $\phi(t)$ is the phase modulation imposed on the pump, and $|a_{in}\rangle$ is the unit Jones vector of the pump. Using Eqs. (5.23) and (5.24) the pump field after the PMD and PDL components can be expressed as follows

$$|A_{out}(\omega)\rangle = \boldsymbol{T}\,\boldsymbol{U}(\omega)|A_{in}(\omega)\rangle. \quad (5.29)$$

By substituting Eqs. (5.23), (5.24) and (5.28) in Eq. (5.29) and taking the Fourier transform, the output pump field in time domain is found to be

$$|A_{out}(t)\rangle = e^{-\mu}e^{\vec{\mu}\cdot\vec{\sigma}}\frac{\sqrt{P}}{2\pi}\int_{-\infty}^{\infty}d\omega\exp\Big[-\frac{i}{2}\omega\vec{b}\cdot\vec{\sigma} - i\omega t\Big] \int_{-\infty}^{\infty}dt'\exp[i\phi(t') + i\omega t']|a_{in}\rangle, \quad (5.30)$$

where the PDL element is assumed to be independent of pump frequency. Using Eq. (5.27) and changing the order of integration, Eq. (5.30) becomes

$$|A_{out}(t)\rangle = e^{-\mu}e^{\vec{\mu}\cdot\vec{\sigma}}\frac{\sqrt{P}}{2\pi}\int_{-\infty}^{\infty}dt'\,e^{i\phi(t')}\int_{-\infty}^{\infty}d\omega\,e^{-i\omega(t-t')} \times\Big[\cos(\omega b/2) - i\sin(\omega b/2)\hat{b}\cdot\vec{\sigma}\Big]|a_{in}\rangle. \quad (5.31)$$

The integrations in Eq. (5.31) can be performed analytically. By using Eq. (5.27), the resulting expression can be written as

$$|A_{out}(t)\rangle = e^{-\mu}\sqrt{P}\exp\Big(\frac{i}{2}[\phi(t+b/2)+\phi(t-b/2)]\Big) \times e^{\vec{\mu}\cdot\vec{\sigma}}e^{-\frac{i}{2}\theta(t)\hat{b}\cdot\vec{\sigma}}|a_{in}\rangle, \quad (5.32)$$

where $\theta(t) = \phi(t+b/2) - \phi(t-b/2)$. The Stokes vector of the pump, defined as $\vec{P}_{out} = \langle A_{out}|\vec{\sigma}|A_{out}\rangle$, becomes

$$\vec{P}_{out}(t) = P e^{-2\mu} \langle a_{in}| e^{\frac{i}{2}\theta\hat{b}\cdot\vec{\sigma}} e^{\vec{\mu}\cdot\vec{\sigma}}\, \vec{\sigma}\, e^{\vec{\mu}\cdot\vec{\sigma}} e^{-\frac{i}{2}\theta\hat{b}\cdot\vec{\sigma}} |a_{in}\rangle. \tag{5.33}$$

To proceed further, the following relation that can be derived from Eqs. (5.25)–(5.27) is used:

$$\begin{aligned} e^{\vec{r}^*\cdot\vec{\sigma}}\, \vec{\sigma}\, e^{\vec{r}\cdot\vec{\sigma}} &= [\tilde{r}(\tilde{r}^*\cdot\vec{\sigma}) + \tilde{r}^*(\tilde{r}\cdot\vec{\sigma}) + i\tilde{r}\times\tilde{r}^*]\,|\sinh(r)|^2 + \vec{\alpha}_R \\ &+ (|\cosh(r)|^2 - (\tilde{r}\cdot\tilde{r}^*)|\sinh(r)|^2 - \vec{\alpha}_I\times)\vec{\sigma} \end{aligned} \tag{5.34}$$

where $\vec{\alpha}_R + i\,\vec{\alpha}_I = 2\cosh(r^*)\sinh(r)\tilde{r}$. With this relation, Eq. (5.33) becomes

$$\vec{P}_{out}(t) = P e^{-2\mu} \left\{ \sinh(2\mu)\hat{\mu} + \left[1 + 2\sinh^2(\mu)\hat{\mu}\hat{\mu}\right] R(\theta)\hat{p} \right\} \tag{5.35}$$

where $R(\theta) = e^{\frac{i}{2}\theta\hat{b}\cdot\vec{\sigma}}\vec{\sigma}\, e^{-\frac{i}{2}\theta\hat{b}\cdot\vec{\sigma}}$, and $\hat{p} = \langle a_{in}|\vec{\sigma}|a_{in}\rangle$ is the unit Stokes vector of the input pump. $R(\theta)$ represents rotation of the SOP of the pump around the direction of the PMD vector by an angle θ and using Eq. (5.34) it can also be expressed as

$$R(\theta) = \cos\theta + (1-\cos\theta)\hat{b}\hat{b} + \sin\theta\hat{b}\times, \tag{5.36}$$

where the projection operator $\hat{b}\hat{b}$ and the cross-product operator $\hat{b}\times$ are defined as [102]

$$\hat{b}\hat{b} = \begin{pmatrix} b_1b_1 & b_1b_2 & b_1b_3 \\ b_2b_1 & b_2b_2 & b_2b_3 \\ b_3b_1 & b_3b_2 & b_3b_3 \end{pmatrix}, \quad \hat{b}\times = \begin{pmatrix} 0 & -b_3 & b_2 \\ b_3 & 0 & -b_1 \\ -b_2 & b_1 & 0 \end{pmatrix}. \tag{5.37}$$

It follows from Eq. (5.35) that the pump SOP becomes time-dependent after the PMD component. The PDL component makes the pump power also time dependent. Since the amount of PMD is much smaller than the duration of a pump-phase modulation cycle, one can expand $\phi(t\pm b/2)$ in a Taylor series and retain terms up to first-order in b. In this case, $\theta(t)$ can be approximated as

$$\theta(t) \approx b\frac{\partial\phi(t)}{\partial t}. \tag{5.38}$$

Therefore, distortions are expected in time intervals during which pump phase changes rapidly.

The power changes induced on the pump depend not only on the amounts of PMD and PDL but also on the relative orientations of the PMD and PDL vectors with respect to the pump SOP. For instance, if the input SOP of the pump is parallel to the PMD vector ($\hat{p} \parallel \hat{b}$), it is not affected by PMD. Similarly, if the PDL vector points in the same direction ($\hat{p} \parallel \hat{b} \parallel \hat{\mu}$), pump power remains unaffected. It is clear from the rotation matrix $R(\theta)$ that, for a given θ, the maximum SOP rotation occurs when the PMD vector and the input pump SOP are orthogonal ($\hat{b} \perp \hat{p}$). In this case, the last term in $R(\theta)$ contributes most because it represents the projection of the pump SOP on the axis that is perpendicular to both the PMD vector and the pump SOP. In the same manner, when the PDL vector is perpendicular to both the PMD vector and the input pump SOP ($\hat{b} \perp \hat{p}$ and $\pm\hat{\mu} \parallel \hat{b} \times \hat{p}$), the variations in the pump power are maximized.

In general, the directions of the three vectors, $\hat{p}$, $\hat{b}$, and $\hat{\mu}$, do not remain fixed in time and rotate randomly on a slow time scale. What is more, some components can have both PMD and PDL at the same time making it impossible to control them independently. Therefore it is not possible to adjust the components so that a minimum amount of distortion is guaranteed. In practice, one observes that pump power distortions can vary over a wide range. In the worst case scenario, the three vectors $\hat{p}$, $\hat{b}$, and $\hat{\mu}$ are mutually orthogonal, and Eq. (5.35) reduces to

$$\vec{P}_{out}(t) = P e^{-2\mu} \left\{ [\sinh(2\mu) \pm \cosh(2\mu) \sin(\theta)]\, \hat{\mu} + \cos(\theta)\hat{p} \right\}. \tag{5.39}$$

Moreover, in FOPAs that use dual pumps, the distortions on the two pumps occur independently and their contribution can add constructively or destructively.

To study how much the pump field is affected by PMD and PDL in a realistic system, it is assumed that the pump is modulated using a pseudo-random bit sequence in the nonreturn-to-zero format [48]. The use of the following functional form

$$\phi(t) = \frac{\pi}{2} \left\{ \mathrm{erf}\left[c_0(2t + T_0)/T_r\right] - \mathrm{erf}\left[c_0(2t - T_0)/T_r\right] \right\} \tag{5.40}$$

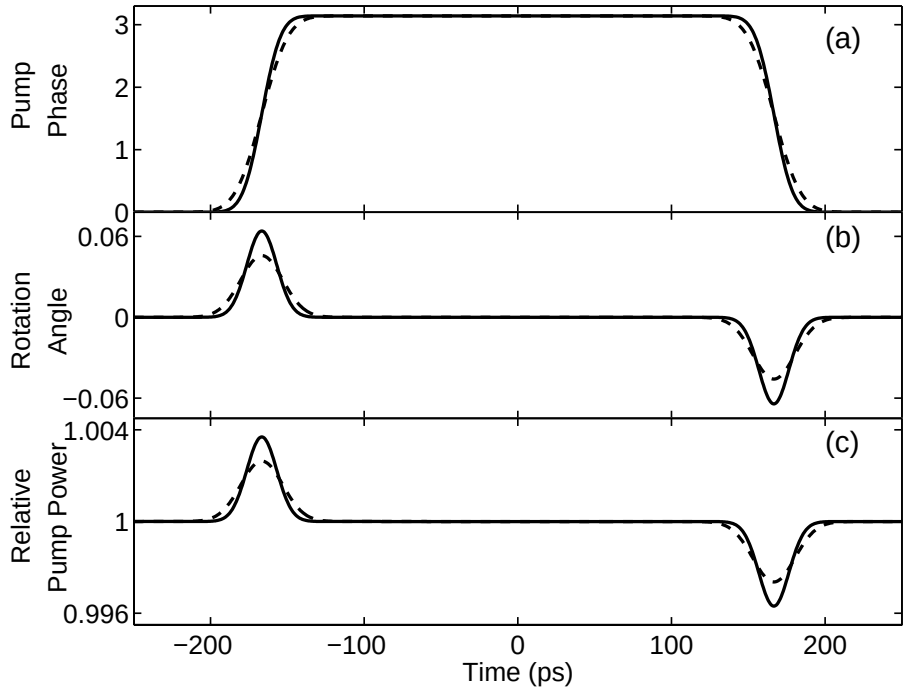

Figure 5.8: (a) Pump-phase variations over a 500-ps window centered on a single bit at 3 Gb/s. Variations of pump SOP (b) and pump power (c) for rise times of 25 ps (solid) and 35 ps (dashed) with 0.5 ps of PMD and 0.5 dB of PDL.

allows us an easy way to adjust the full-width at half maximum and the rise time of the pulses by choosing T_0 and T_r appropriately. Here $\mathrm{erf}(x)$ stands for the error function, and $c_0 \approx 0.9$ guarantees that T_r is the duration in which the pump phase increases from 10% to 90% of its maximum. Using Eqs. (5.38) and (5.40) the rotation angle is given by

$$\theta(t) \approx \frac{2c_0\sqrt{\pi}b}{T_r}\Big\{\exp\Big[-c_0^2(2t+T_0)/T_r^2\Big] - \exp\Big[-c_0^2(2t-T_0)/T_r^2\Big]\Big\}. \qquad (5.41)$$

This equation shows that the faster the pump phase is modulated and the larger the PMD is, the larger the pump SOP rotation will be.

In recent experiments, pump phase has been modulated at bit rates ranging from 2 to 10 Gb/s [61], [65]. Rise times are quoted rarely, but a rise time of 30 ps was used in [61]. Realistic values for PMD and PDL magnitudes are also needed. However, since

these values can vary over a wide range in practice, they are varied over a realistic range. As an example, Figure 5.8 is drawn for a PMD of 0.5 ps and a PDL of 0.5 dB. Part (a) shows pump-phase variations from Eq. (5.40) for an isolated 1 bit at a bit rate of 3 Gb/s ($T_0 = 333$ ps). The solid and dashed curves in part (b) show $\theta(t)$ for rise times of 25 and 35 ps, respectively. It is assumed that the PMD vector is perpendicular to the input pump SOP, resulting in the maximum rotation. At locations where the pump phase changes rapidly, $\theta = 2.6^\circ$ for $T_r = 35$ ps and increases to $\theta = 3.6^\circ$ when the rise time is reduced to 25 ps. Fig. 5.8(c) shows relative changes in the pump power for a PDL of 0.5 dB for the same two rise times, assuming that the PDL vector is perpendicular to both $\hat{b}$ and $\hat{p}$. In this configuration, the pump power varies by less than 0.5%. Even though a 0.5% change sounds small, it can affect the FOPA performance as discussed in next Section.

5.4.3 Polarization Dependence of FOPA Gain

The preceding discussion is quite general, and it can be used for both single- and dual-pump FOPAs. This Section focuses on a practical, dual-pump FOPA configuration in which the two pumps are linearly as well as orthogonally polarized. Such FOPAs can provide a relatively large gain bandwidth that is nearly insensitive to signal SOP [55]–[61] as long as pump polarizations remain perfectly orthogonal.

In Section 5.4.1, it is shown that the SOPs and powers of the two pumps change during time intervals their phase changes rapidly. The important question is how the signal gain changes when the pumps experience PMD and PDL before entering the FOPA. As the SOPs of the input pumps are not fixed, vectorial FWM equations have to be used. Since most FOPAs use long lengths of fiber, the expression for the signal gain obtained in Section 3.3.3 can be used assuming that the pump wavelengths are close enough to allow for ignoring PMD effects. In this case the signal gain is given by

Eqs. (3.50) and (3.51) as

$$G_3(L) = \frac{G_+ + G_-}{2} + \frac{G_+ - G_-}{2}\hat{p}_0 \cdot \hat{p}_3, \qquad G_\pm = 1 + \left[\frac{F_\pm}{g_\pm}\sinh(g_\pm L)\right]^2 \tag{5.42}$$

where

$$g_\pm = \sqrt{F_\pm^2 - \kappa^2}, \qquad F_\pm = \gamma_e\sqrt{P_1 P_2}[1 \pm \cos(\theta_p/2)]. \tag{5.43}$$

According to Eqs. (5.42) and (5.43), if the pump powers or pump SOPs change, the signal gain is also affected. In fact, even if pump powers and SOP change slightly, the impact on the signal can be quite large because of the presence of the $\sinh(g_\pm L)$ in Eq. (5.43). To illustrate the impact of PMD and PDL on the signal and idlers, consider a FOPA designed using a 1-km-long highly nonlinear fiber ($\gamma_e = 15$ W^{-1}km^{-1}) having its zero-dispersion wavelength at 1583.5 nm. The third-and fourth-order dispersion parameters at this wavelength are $\beta_3 = 0.055$ ps^3/km and $\beta_4 = 2.35 \times 10^{-4}$ ps^4/km. These fiber parameters correspond to an actual configuration used experimentally [48]. The two pumps are orthogonally polarized initially and are launched with 260 mW of power at wavelengths of 1559 and 1609 nm.

Figure 5.9 shows the signal gain G_3 as a function of signal frequency predicted by Eq. (5.42) for such a FOPA. As shown by the solid curve, in the absence of the PMD and PDL effects, the FOPA produces a uniform gain of 28 dB in the central spectral region between the two pumps. Dependence of signal gain on the relative orientations of input pumps is shown by the dotted and the dashed curves for which $\theta_p = 180^\circ \pm 2.5^\circ$. In each case, the vertical bars show the extent of gain variations when pump powers are changed artificially by $\pm 1\%$. The main point to note is that the signal can change by > 1 dB with relatively small changes in pump powers and small deviations from perfect orthogonality of the pump SOPs. It should be stressed that even though Figure 5.9 shows only the signal gain, the same behavior occurs for the idler beam because FWM generates signal and idler photons in pairs. In the following, the focus is on signal amplification but the conclusions apply for other FOPA applications related to phase conjugation or wavelength conversion.

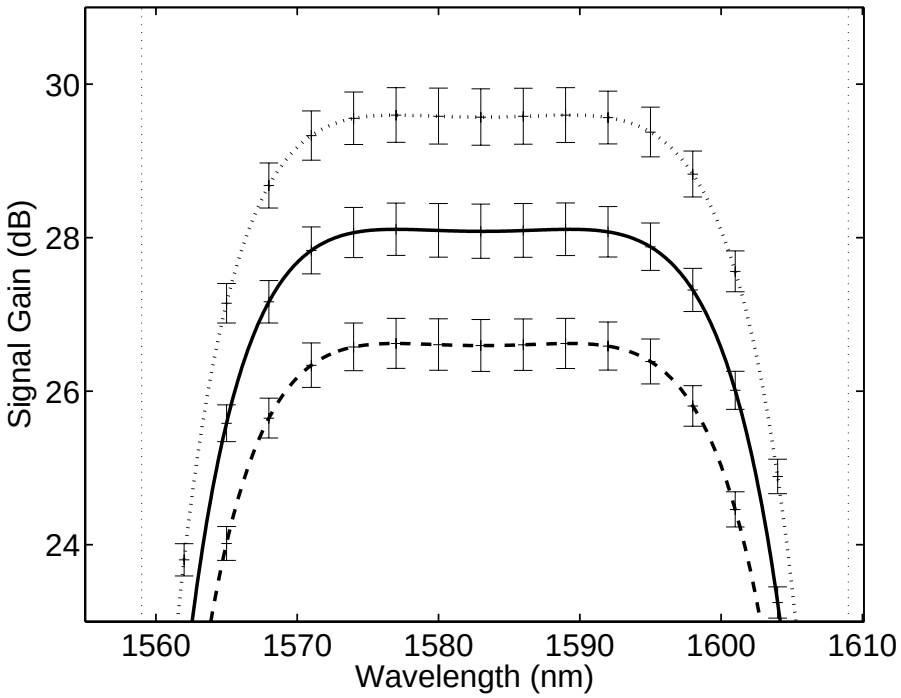

Figure 5.9: FOPA gain as a function of signal wavelength when two pumps are orthogonally polarized ($\theta = \pi$, solid curve). The dotted and dashed curves show the cases when pump SOPs make an angle of 177.5° and 182.5°, respectively. In each case, vertical bars show the extent of gain variations when pump powers vary by 1%.

5.4.4 Temporal Variations in Amplified Signal

Now, temporal changes in the signal power produced by PMD and PDL can be calculated when pump phases are modulated to suppress SBS. Figure 5.10 shows the amplified signal power (normalized to its time-averaged value) over the same time interval used for Fig. 5.8. As discussed in Section 5.4.1, the relative orientations of the pump SOPs with respect to the PMD and PDL vectors determines how much the signal is distorted. To illustrate this point, parts (a)–(c) of Fig. 5.10 correspond to different orientations of the PMD and PDL vectors. In Fig. 5.10a, the pumps are linearly and orthogonally polarized such that $\hat{p}_1 = [1,0,0]$ and $\hat{p}_2 = [-1,0,0]$. The PMD and PDL vectors affecting the first pump are $\hat{b}_1 = [0,0,1]$ and $\hat{\mu}_1 = [0,1,0]$. These vectors for

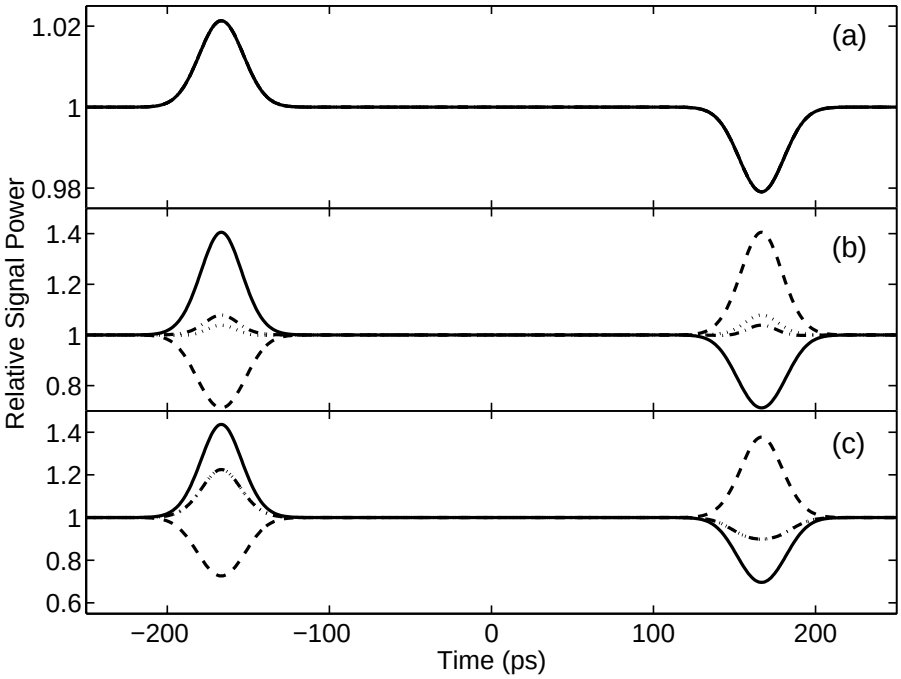

Figure 5.10: Time dependence of the relative signal power at the FOPA output for three different orientations of the pump SOP vector, PMD vector, and PDL vector. In parts (b) and (c) different curves are for different signal SOPs discussed in the text.

the second pump are oriented such that $\hat{b}_2 = [0,0,-1]$ and $\hat{\mu}_2 = [0,-1,0]$. The magnitudes of PMD and PDL are 0.5 ps and 0.5 dB, respectively, for both pumps. Since pumps pass through the PMD components pointing in the opposite directions and their phases are modulated in opposition, both pumps are rotated in the same direction. In this situation, the pumps preserve their orthogonality throughout the FOPA length. The PDL vectors are oriented such that the two pumps have the same power profile (similar to that shown in Fig. 5.8). Therefore, signal distortions in Fig. 5.10a are solely due to pump power variations. Moreover, as the pumps maintain their orthogonality, distortions are the same for all input signal SOPs, i.e, such a FOPA does not exhibit any polarization-dependent gain (PDG).

In Fig. 5.10b, the PMD vector affecting the second pump is changed to $\hat{b}_2 = [0,0,1]$ so that pumps rotate in opposite directions and lose their orthogonality. Also, pump

powers are affected by PDL such that their total power is nearly time-independent. As a result, distortions in Fig. 5.10b originate mostly from variations in the pump SOPs. In the time interval where pump phases change rapidly, the pump SOPs deviate from orthogonality, and the signal gain depends on the input signal SOP as well as the pump SOPs. The solid, dashed, dotted and dashed-dotted curves in Fig. 5.10b correspond to the four choices of signal SOPs governed by $\hat{p}_3 = [0,1,0]$, $[0,-1,0]$, $[1,0,0]$ and $[0,0,1]$, respectively. For certain signal SOPs, signal power can fluctuate more than 65%, indicating severe degradation of the FOPA performance caused by the PMD effects.

In Fig. 5.10c, both the PMD and PDL vectors affecting the second pump are taken to be the same as those that affect the first pump. In this configuration, pump SOPs rotate in opposition but pump powers change in unison. The contributions of pump power variations adds to the distortion caused by pump-polarization variations at the rising edge of the phase modulation profile but is subtracted from it at the falling edge. As a result, the magnitude of signal distortion at the rising edge is even larger than that shown in Fig. 5.10b. In all cases in Fig. 5.10, the pump SOP, PMD and PDL vectors are chosen to be mutually orthogonal for both pumps, resulting in maximum pump distortion. However, the distortion of the two pumps may add up or mitigate the effects of each other, albeit in an uncontrollable manner. Moreover, since the directions of the PMD and PDL vectors may change with time, signal distortions may fluctuate in time, taking on shapes similar to those shown in Fig. 5.10 or their combinations. In practice, PMD and PDL effects would appear as noise and lower the signal-to-noise ratio.

A comparison of Fig. 5.10a and Fig. 5.10b shows that for a given amount of PMD, deviations from orthogonality of the pump SOPs are more harmful than pump-power distortions caused by the combination of PMD and PDL. Even though the pump SOPs as well as pump powers affect the FOPA gain exponentially by modifying $F_{\pm}$ in Eq. (5.43), the nonorthogonality of the pump SOPs affects this quantity directly through θ_p and is thus more harmful. It is important to stress that Fig. 5.10 focuses

on the cases in which the PMD and PDL vectors are oriented such that they cause the largest degradation of the pump. In practice these vectors can align from time to time in such a way that the signal is relatively unaffected.

Unlike FOPAs with orthogonal pumps, when pump SOPs are parallel, their rotation becomes less of a problem. Signal degradation in this situation is mainly due to pump power variations which, as seen in Fig. 5.10a, are quite small ($< 2\%$).

5.4.5 A Practical Solution

Since the nonorthogonality of two pumps caused by PMD and PDL is detrimental to the FOPA performance, it would help if their SOPs are made perfectly orthogonal before the pumps enter the fiber. This can be enforced in practice by placing good-quality polarizers at the input end of the FOPA. Even though these polarizers would cause some power distortion, it is shown in this section that they improve the signal quality drastically at the FOPA output. Their use thus constitutes a simple practical solution to the PMD- and PDL-induced degradation of FOPAs.

Figure 5.11 shows how much signal distortion can be mitigated by using polarizers. This Figure is drawn under conditions identical to those used for Fig. 5.10 except for the use of polarizers. Polarizers are adjusted so that their maximum transmission axes are parallel to the input SOPs of the pumps with a 30-dB extinction ratio. A comparison of Figs. 5.10 and 5.11 shows that polarizers help in reducing signal distortion in all cases. In some cases, signal-power variations are reduced from more than 65% to less than 3%. The residual distortion is related to the finite extinction ratio of the polarizers used, and a small amount of distortion is induced by the polarizers themselves. Figure 5.11b shows that the FOPA exhibits some PDG because different signal SOPs are affected differently. This is a sign that pumps still have polarization components that are not orthogonal. If polarizers with an extinction ratio of 50 dB are used, the distortion reduces to below 1% for all input signal SOPs. Polarizers also help reducing the signal

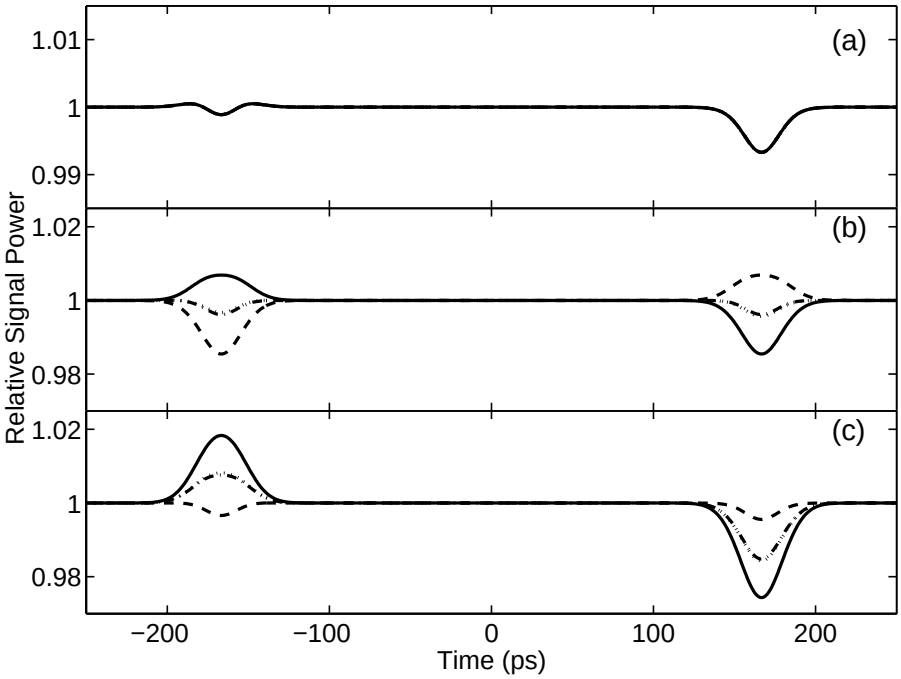

Figure 5.11: Same as Fig. 5.10 except, polarizers with 30-dB extinction ratio are used before two pumps enter the FOPA.

distortion in Fig. 5.10c where variations in both the pump power and pump SOPs affect the signal. In this case, if polarizers with >50 dB extinction ratio are used, PDG totally disappears and Fig. 5.11c reduces to Fig. 4a for all input signal SOPs.

From a practical perspective, one is interested in knowing how much signal quality is degraded by the PMD and PDL effects. For this purpose, the standard deviation of signal fluctuations is calculated by using $\sigma_3 = \left[\langle P_3^2\rangle - \langle P_3\rangle^2\right]$, where the angle brackets denote time averaging over a single bit duration. In Fig. 5.12, the relative distortion, $\sigma_3/\langle P_3\rangle$, is plotted as a function of PMD for several values of the average FOPA gain G_3 when the relevant vectors are adjusted to give the maximum distortion. The PDL magnitude is taken to be 0.5 dB in all cases. The rise time is taken to be 35 ps. Polarizers are used in Fig. 5.12b to demonstrate how much they help in improving the signal quality. Figure 5.12 shows that signal distortion increases with PMD as well as with G_3. Polarizers reduce the impact of PMD and PDL induced distortions to a large extent. For

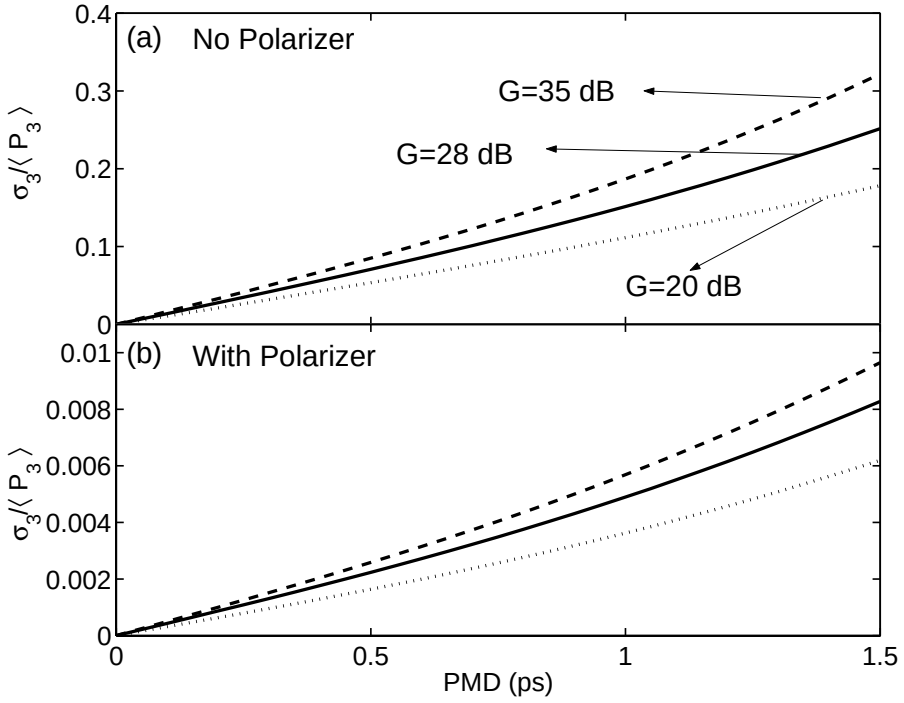

Figure 5.12: Noise-to-signal ratio plotted as a function of PMD, assuming a PDL of 0.5 dB for both pumps. Notice the dramatic improvement in the case (b) in which polarizers with 30-dB extinction ratio are used.

example, for a 1-ps PMD and a 28-dB FOPA gain, the output noise level is reduced from 15% to 0.5% when polarizers are used at the input end of the FOPA. Note that $\langle P_3 \rangle / \sigma_3$ is not related directly to signal-to-noise ratio since only the worst case distortion is taken into account.

5.5 Conclusions

In conclusion, noise associated with pumps is a major source of signal degradation. If FOPAs are not designed properly they can reduce signal SNR severely.

In Section 5.2 it is shown that the walk-off effects can be beneficial in designing low-noise FOPAs when the primary source of noise is the ASE added by EDFAs used

to amplify pumps. How much pump noise is transferred to the signal depends on the FOPA length and the bandwidth of the pump filter. Numerical simulations show that FOPA length plays a significant role, and the SNR is lower for shorter fiber lengths. From the standpoint of RIN transfer, it is better to use a longer fiber. In practice, the FOPA length should be optimized to balance the conflicting requirement of a high bandwidth and a low RIN.

Section 5.3 showed that PM-to-AM conversion of pumps lowers the SNR of both the amplified and wavelength-converted signals when dual-pump FOPAs are employed. The problem can be solved to some extent by optimizing the bit rate and the rise time of the bit stream used for pump PM. One should choose PM parameters such that the desired level of SBS suppression is achieved without inducing large variations in the signal and idler powers. The length of the FOPA is also an important design parameter since it determines both the extent of PM-to-AM conversion and the walk-off effects.

It is shown in Section 5.4 that PMD and PDL associated with various optical components affect the quality of pump beams even before they enter a FOPA, and this in turn may produce relatively large changes in the signal and idler powers at the FOPA output. The magnitude of such changes depends on the relative SOPs of the two pumps. In particular, predicted changes are relatively large for orthogonally polarized pumps, but they become negligible for copolarized pumps. A simple solution is proposed to mitigate the impact of PMD and PDL. It is shown that the use of high-quality polarizers just before the input end of the fiber can improve the performance of a dual-pump parametric amplifier dramatically.

6 Polarization-Independent Single-Pump FOPAs

It is discussed in Chapter 3 that dual-pump FOPAs have several advantages compared to single-pump FOPAs. For instance, dual-pump FOPAs can provide a more uniform gain, they can be made to be insensitive to signal polarization using orthogonally polarized pumps, and they are more robust to pump-phase modulation. However, the single-pump configuration remains attractive because of its relative simplicity [6]–[17], [43].

6.1 Review of Existing Techniques

A major drawback of the single-pump configuration is that the efficiency of the underlying FWM process depends critically on the relative polarization states of the pump and signal. Several schemes have been proposed to solve this problem. However these schemes require additional optical components whose use increases the complexity of the FOPA design.

One of the most commonly used schemes employs a polarization-diversity loop [103]–[106]. In this approach, the pump beam is split into its orthogonally polarized components with equal amount of powers, which counterpropagate inside a Sagnac loop. When the signal enters the loop, it is also split into its orthogonally polarized components, each of which copropagates with the identically polarized pump. The

two polarization components of the signal are then recombined after the polarization-diversity loop. Such polarization-diversity loops have been used for optical sampling at 80 Gb/s with a residual polarization dependence of only 0.7 dB [104]. By using a polarization-maintaining HNLF inside such a loop, the wavelengths of 32 channels, each operating at 10 Gb/s, were converted simultaneously with a polarization dependence of only 0.2 dB [105]. A polarization-maintaining, highly birefringent fiber was used in this experiment to make sure that pump, signal and idler fields remain copolarized during the propagation and are not affected by PMD induced by residual birefringence.

In a recent experiment a slightly more complicated method was used [63]. In this scheme, the pump is linearly polarized at a fixed axis and signal is launched with arbitrary polarization. After propagating in the fiber once, the pump field is reflected back into the fiber using a fiber-brag-grating mirror. Signal and idler are also reflected back into the fiber after their SOPs are rotated by 90 degrees using a Faraday rotator. In this scheme, each polarization component of the signal field experiences gain from a copolarized pump either in the forward or backward propagation. This scheme is analogous to the polarization-diversity loop scheme in the sense that polarization components of signal and idler are amplified by the same amount at different stages. Even though this scheme is slightly more difficult to implement, it makes use of whole pump power, whereas in the polarization diversity loop scheme, the signal is amplified by half of the pump power. Other application-dependent schemes require more complicated setups and they work only when pump field is pulsed [23], [107].

This Chapter proposes a relatively simple scheme that requires only a highly birefringent fiber for FWM. In this scheme, the pump beam is polarized at 45° from the slow (or fast) axis of the fiber, while the signal polarization can vary over the entire Poincaré sphere. Under such conditions, the pump power is divided equally between the two principal axes of the fiber. The vector theory of FWM is used to show that, under these conditions, each pump component amplifies only the copolarized signal com-

ponent because the orthogonal FWM process is not phase-matched because of large birefringence. The results of this Chapter show that gain variations with respect to signal SOP can be reduced to <0.1 dB with the proposed scheme.

6.2 Theoretical Model

FWM in highly birefringent fibers have been investigated in the context of single- [108] and dual-pump FOPAs [109]. It has been shown that, in highly birefringent fibers, birefringence also affects the phase-matching condition. The phase-matching condition for different FWM processes depends on fiber birefringence in different ways. It is shown below that such dependence on fiber birefringence can be used to eliminate unwanted FWM processes in a certain wavelength region where polarization-independent parametric gain can be achieved.

The vectorial form of FWM equations for a single-pump FOPA using a highly birefringent fiber can be obtained from the vectorial FWM equations (2.67)–(2.68) derived for dual-pump FOPAs in Section 2.6, by setting the second pump field to zero $|A_2\rangle = 0$ in the pump equation (2.67) and replacing both $|A_1\rangle$ and $|A_2\rangle$ by $|A_1\rangle/\sqrt{2}$ in the signal and idler equations (2.68) :

$$\frac{d|A_1\rangle}{dz} = i\beta(\omega_1)|A_1\rangle + ib\boldsymbol{\sigma_1}|A_1\rangle + i\gamma\left[P_1 - \frac{1}{3}\langle A_1|\boldsymbol{\sigma_3}|A_1\rangle\boldsymbol{\sigma_3}\right]|A_1\rangle, \tag{6.1}$$

$$\begin{aligned}\frac{d|A_3\rangle}{dz} &= i\beta(\omega_3)|A_3\rangle + i[b + b_1(\omega_3-\omega_1)]\boldsymbol{\sigma_1}|A_3\rangle \\ &\quad + i\gamma\left[P_1 + |A_1\rangle\langle A_1| - \frac{1}{3}\Big(\langle A_1|\boldsymbol{\sigma_3}|A_1\rangle\boldsymbol{\sigma_3} + \boldsymbol{\sigma_3}|A_1\rangle\langle A_1|\boldsymbol{\sigma_3}\Big)\right]|A_3\rangle \\ &\quad + i\gamma\left[|A_1\rangle\langle A_1^*| - \frac{1}{3}\boldsymbol{\sigma_3}|A_1\rangle\langle A_1^*|\boldsymbol{\sigma_3}\right]|A_4^*\rangle,\end{aligned} \tag{6.2}$$

$$\begin{aligned}\frac{d|A_4\rangle}{dz} &= i\beta(\omega_4)|A_3\rangle + i[b + b_1(\omega_4-\omega_1)]\boldsymbol{\sigma_1}|A_4\rangle \\ &\quad + i\gamma\left[P_1 + |A_1\rangle\langle A_1| - \frac{1}{3}\Big(\langle A_1|\boldsymbol{\sigma_3}|A_1\rangle\boldsymbol{\sigma_3} + \boldsymbol{\sigma_3}|A_1\rangle\langle A_1|\boldsymbol{\sigma_3}\Big)\right]|A_4\rangle \\ &\quad + i\gamma\left[|A_1\rangle\langle A_1^*| - \frac{1}{3}\boldsymbol{\sigma_3}|A_1\rangle\langle A_1^*|\boldsymbol{\sigma_3}\right]|A_3^*\rangle,\end{aligned} \tag{6.3}$$

where $\beta(\omega) = \omega(n_x + n_y)/(2c)$ is the average propagation constant, n_x and n_y are the effective mode indices along the slow and fast axes, respectively. The two birefringence parameters are defined as $b = \delta n \omega_1/c$ and $b_1 = \delta n/c$, where $\delta n = n_x - n_y$ is assumed to have negligible frequency dependence. The term b_1 is the PMD term and it is responsible for frequency-dependent birefringence. Unlike the random birefringence and PMD terms discussed in Sections 3.3 and 4.2, and the effective PMD term introduced in Section 5.4, birefringence in highly birefringent fibers discussed in this Section is much larger and has a fixed direction. To stress this difference, the effect of the PMD term will be discussed in the context of differential-group velocity difference (DGD) defined as $\Delta\tau = b_1 L$. In physical terms, DGD represents the relative delay between the two polarization components of a field propagating along the fast and slow axes. The fiber is assumed to have a linear birefringence, and the equations are written in the linear SOP basis. Therefore, birefringence is expressed in terms of the $\boldsymbol{\sigma_1}$ matrix.

Equation (6.1) shows that the pump polarization changes because of fiber birefringence as well as SPM-induced coupling between the two polarization components of the pump. Fiber birefringence and nonlinear birefringence rotate the pump SOP around different axes which leads to a complicated motion. To see the nature of this evolution it is instructive to write the equation for the evolution of individual polarization components of the pump field as

$$\frac{du_1}{dz} = i\gamma\left(|u_1|^2 + \frac{2}{3}|v_1|^2\right)u_1 + \frac{i\gamma}{3}v_1^2 u_1^* e^{-i4\pi z/L_B} \tag{6.4}$$

$$\frac{dv_1}{dz} = i\gamma\left(|v_1|^2 + \frac{2}{3}|u_1|^2\right)v_1 + \frac{i\gamma}{3}u_1^2 v_1^* e^{i4\pi z/L_B} \tag{6.5}$$

where, $L_B = 2\pi/b$ is the beat length, and a change of variables is introduced through

$$|A_1\rangle = \begin{pmatrix} u_1 e^{ibz/2} \\ v_1 e^{-ibz/2} \end{pmatrix} e^{i\beta(\omega_1)z}. \tag{6.6}$$

The first two terms on the right hand side of Eqs. (6.4) and (6.5) can be called SPM and XPM terms. These terms only contribute to the phase and do not change the power

contained in that component. However, the last terms are called the coherent coupling terms and they can transfer energy between the two polarization components of the pumps. This can be seen by calculating the evolution of the power in each polarization component as follows

$$\frac{d|u_1|^2}{dz} = -\frac{2\gamma}{3}\mathrm{Im}\left\{(v_1 u_1^*)^2 e^{-i4\pi z/L_B}\right\} \tag{6.7}$$

$$\frac{d|v_1|^2}{dz} = -\frac{2\gamma}{3}\mathrm{Im}\left\{(v_1^* u_1)^2 e^{i4\pi z/L_B}\right\}. \tag{6.8}$$

In general, $v_1 u_1^*$ is not real and the two polarization components exchange energy. However, when the beat length ($L_B = 2\pi/b$) of the fiber is much shorter than the nonlinear length [$L_{\mathrm{NL}} = (\gamma P_1)^{-1}$], the coherent coupling term can be neglected. As a result, in highly birefringent fibers, the pump powers in the fast and slow axis retain their power along the fiber length. Ignoring the last term in Eqs. (6.4) and (6.5), these equations can be solved to give

$$|A_1(z)\rangle = \exp\left[i\beta(\omega_1)z + i(bz/2)\sigma_1 + \frac{i\gamma z}{6}\left(5\langle A_1|A_1\rangle + \langle A_1|\sigma_1|A_1\rangle\sigma_1\right)\right]|A_1(0)\rangle. \tag{6.9}$$

To see the origin of various FWM processes explicitly, a simple change of variables is introduced for the signal and idler fields as

$$\begin{pmatrix} u_k \\ v_k \end{pmatrix} = \exp\left[\frac{iz}{2}[b + b_1(\omega_k - \omega_1)]\sigma_1 + \frac{2i}{3}\gamma z\left(2\langle A_1|A_1\rangle + \langle A_1|\sigma_1|A_1\rangle\sigma_1\right)\right]|A_k\rangle \tag{6.10}$$

where u_k and v_k ($k = 3$ or 4) are the polarization components along the fast and slow axes. Using Eq. (6.10) and the solution given in Eq. (6.9) in Eq. (6.2) and (6.3), the

individual polarization components of the signal and idler are found to evolve as

$$\frac{du_3}{dz} = i\gamma\Big(u_1^2u_4^* + \frac{1}{3}v_1^2u_4^*e^{-i4\pi z/L_B} + \frac{2}{3}u_1v_1v_4^*e^{i(\Delta\tau\Delta\omega)z/L}\Big)e^{-i\kappa z} + \frac{2i\gamma}{3}u_1v_1^*v_3e^{i(\Delta\tau\Delta\omega)z/L} + \frac{2i\gamma}{3}u_1^*v_1v_3e^{-i4\pi z/L_B}, \tag{6.11}$$

$$\frac{dv_3}{dz} = i\gamma\Big(v_1^2v_4^* + \frac{1}{3}u_1^2v_4^*e^{-i4\pi z/L_B} + \frac{2}{3}v_1u_1v_4^*e^{-i(\Delta\tau\Delta\omega)z/L}\Big)e^{-i\kappa z} + \frac{2i\gamma}{3}v_1u_1^*u_3e^{-i(\Delta\tau\Delta\omega)z/L} + \frac{2i\gamma}{3}v_1^*u_1u_3e^{-i4\pi z/L_B}, \tag{6.12}$$

$$\frac{du_4}{dz} = i\gamma\Big(u_1^2u_3^* + \frac{1}{3}v_1^2u_3^*e^{-i4\pi z/L_B} + \frac{2}{3}u_1v_1v_3^*e^{-i(\Delta\tau\Delta\omega)z/L}\Big)e^{-i\kappa z} + \frac{2i\gamma}{3}u_1v_1^*v_4e^{i(-\Delta\tau\Delta\omega)z/L} + \frac{2i\gamma}{3}u_1^*v_1v_4e^{-i4\pi z/L_B}, \tag{6.13}$$

$$\frac{dv_4}{dz} = i\gamma\Big(v_1^2v_3^* + \frac{1}{3}u_1^2v_3^*e^{-i4\pi z/L_B} + \frac{2}{3}v_1u_1v_3^*e^{i(\Delta\tau\Delta\omega)z/L}\Big)e^{-i\kappa z} + \frac{2i\gamma}{3}v_1u_1^*u_4e^{i(\Delta\tau\Delta\omega)z/L} + \frac{2i\gamma}{3}v_1^*u_1u_4e^{-i4\pi z/L_B}, \tag{6.14}$$

where $\Delta\omega = \omega_3 - \omega_1$, $\kappa = \Delta\beta + \gamma P_1$ is the phase-mismatch parameter and the quantity $\Delta\beta = 2\sum_{m=1}^{\infty}\beta_{2m}\Delta\omega^{2m}/(2m!)$ is its linear part originating from fiber dispersion, as usual. In deriving Eqs. (6.11)–(6.14), pump powers along the two principal axes are chosen to be equal at the input end, i.e., $|u_1|^2 = |v_1|^2 = P_1/2$.

6.3 Competing FWM Processes

Different nonlinear processes can be identified easily in Eqs. (6.11)–(6.14). The first three terms in the parentheses are the FWM terms; they transfer energy from the pump to the signal and idler as long as the phases associated with these terms do not vary considerably over one nonlinear length. The first FWM term couples the pump, signal and idler components copolarized along the same axis. Since each component of the signal is amplified independently by the same amount, this term yields polarization-insensitive gain. Its phase-matching condition, $\kappa = 0$, is independent of fiber birefringence and leads to relatively broad gain bandwidth in the vicinity of the pump frequency. This FWM process is the one that is considered in Section 3.1 in the scalar FWM case,

where all fields are assumed to have the same linear polarization. It would provide the dominant contribution and make the signal gain polarization-independent if one ensures that this FWM process is the only phase-matched process, in the frequency region of interest.

The second FWM term transfers energy from the pump to the copolarized signal and idler components that are orthogonally polarized to the pump. This FWM process can be separated into two parts. One that transfers energy from v_1 to u_3 and u_4, as described by the second term in Eq. (6.11) and the second term in Eq. (6.13) and the other that transfers energy from u_1 to v_3 and v_4 as described by the second terms of Eqs. (6.12) and (6.14). The phase-matching condition for these two processes become, $\kappa \pm 4\pi/L_B = 0$, respectively. Clearly, the phase-matching condition depends heavily on fiber birefringence and cannot be satisfied in the vicinity of the pump frequency where the first FWM process is phase-matched, i.e, $\kappa \approx 0$.

The third FWM term involves both polarization components of the pump at the same time, and energy is transferred from them to the signal and idler components that are orthogonally polarized. Such a FWM process leads to polarization-dependent gain. The phase-matching condition for this process, $\kappa \pm (\Delta\omega\Delta\tau/L) = 0$, depends on birefringence through the DGD $\Delta\tau$. The plus and minus signs depend on whether the signal is on the fast or the slow axis assuming $\omega_3 > \omega_1$. These FWM processes can also be nearly eliminated by choosing a fiber with birefringence large enough that $\delta n \gg \gamma P_1 c/\Delta\omega$.

The last two terms in Eq. (6.11) involve only the pump and the signal, and they lead to polarization-dependent XPM. Combined with other FWM processes, these terms can also contribute to polarization-dependent gain by transferring energy from one component of the signal to the other one. However, when the fiber has large DGD, these terms cannot be phase-matched. For the same reason, it is possible to realize polarization-insensitive XPM in a highly birefringent fiber [110].

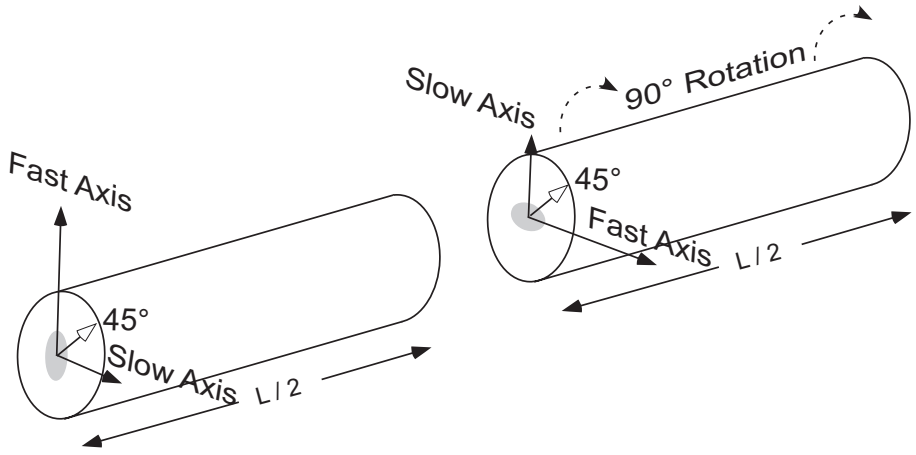

Figure 6.1: Schematic of the proposed scheme. A linearly polarized pump is launched at 45° from each principal axis. The second half of the fiber is rotated by 90° and spliced to the first half.

When DGD is large, the only process that satisfies phase matching in the vicinity of the pump frequency is the first FWM term. Retaining only this term in Eqs. (6.11)–(6.14), following the standard procedure used in Chapter 3 the signal gain is found to be

$$G(\omega_3) = 1 + \frac{\sinh^2(gL/2)}{(gL_{\rm NL})^2}, \qquad g = \sqrt{(\gamma P_1)^2 - \kappa^2}. \tag{6.15}$$

6.4 Proposed Scheme and Results

One issue remains to be addressed. Because of a large DGD needed for polarization-insensitive gain, two polarization components of the signal (and idler) would split in the time domain and would not remain synchronous at the output end. This may not be desirable in practice, especially when the signal is in the form of pulses. However, in practice, this problem can be solved with a simple trick. The basic idea is shown in Fig. 6.1 and consists of cutting the birefringent fiber in half, rotating the second half by 90° so that its slow and fast axes are reversed, and splicing it back to the first half. In the second section, the signal still experiences polarization-insensitive gain (because

the pump is still oriented at 45° with respect to the principal axes), but the DGD induced in the first section is completely compensated inside this section. Of course, one can also employ a pre- or post-compensation scheme in which the DGD is compensated, before or after the FOPA, by sending the signal (and idler) pulses through an unpumped birefringent fiber that has the same magnitude of DGD but its principal axes are rotated by 90° from the FOPA fiber.

To test the validity of all the assumptions that are used to obtain the simple analytical expression given in Eq. (6.15), the coupled-nonlinear Schrödinger equation (2.54) derived in Section 2.5 is solved numerically, using the split-step Fourier-transform method. The FOPA parameters used in the simulations correspond to a realistic, highly nonlinear fiber and are $L = 1$ km, $\gamma = 17$ W^{-1}km^{-1}, $\beta_3 = 0.055$ ps^3/km, and $\beta_4 = 2.35 \times 10^{-4}$ ps^4/km. The zero-dispersion wavelength of the fiber is at 1583.5 nm and its birefringence $\delta n = 10^{-6}$ corresponds to a beat length of 1.5 m. Birefringence is kept low intentionally so that residual effects of unwanted FWM processes are visible. The pump is in the form of quasi-CW pulses with a peak power of 320 mW at a wavelength of 1583.7 nm.

Figure 6.2 shows the FOPA gain as a function of signal wavelength. The central peak is at the location of the pump. The solid and dotted curves show the maximum and the minimum gain occurring when the signal polarization is parallel or perpendicular to the pump polarization, respectively. The signal gain lies in between these two curves for other polarization states. The dashed curve shows, for comparison, the signal gain predicted by Eq. (6.15). Clearly, a nearly polarization-independent gain is achieved even for a fiber birefringence as low as $\delta n = 10^{-6}$.

The inset in Figure 6.2 shows that a small amount of polarization dependence remains in the form of small-scale ripples. Its magnitude can be quantified through a quantity, called the polarization-dependent gain (PDG) and defined as the ratio of the maximum to the minimum signal gain, as the input signal SOP is varied. As seen in the inset, PDG remains below 0.5 dB across the gain peak. To study the dependence of

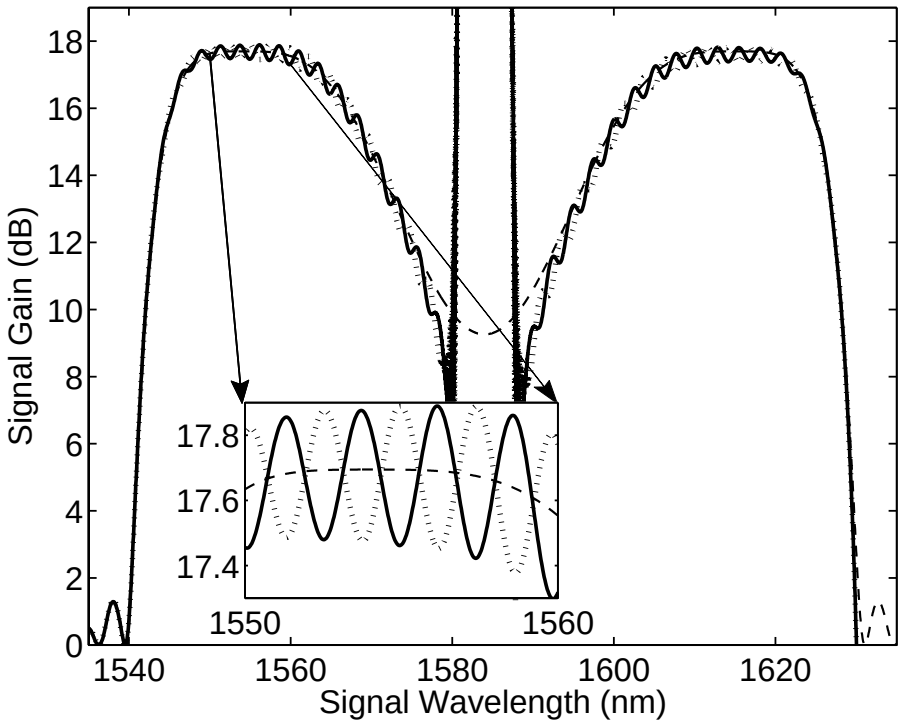

Figure 6.2: Signal gain as a function of wavelength. The solid and dotted curves correspond to signal polarizations that are parallel and orthogonal to the pump, respectively. The dashed curve shows the gain predicted by Eq. (6.15). The inset shows the gain on a magnified scale.

PDG on birefringence, δn is varied from 10^{-6} to 2×10^{-5}. Further inspection shows that the amplitude of the ripples (hence PDG) decreases and their frequency increases as the fiber birefringence is increased. Figure 6.3 shows PDG as a function of fiber birefringence. The upper curve corresponds to the same FOPA pumped with 500 mW of pump power, producing 30 dB peak gain. It is found that PDG scales inversely with fiber birefringence (on a dB scale) and reduces to $<$0.05 dB when fiber birefringence exceeds 10^{-5}. The solid curves show the fit obtained using an inverse dependence of PDG on δn.

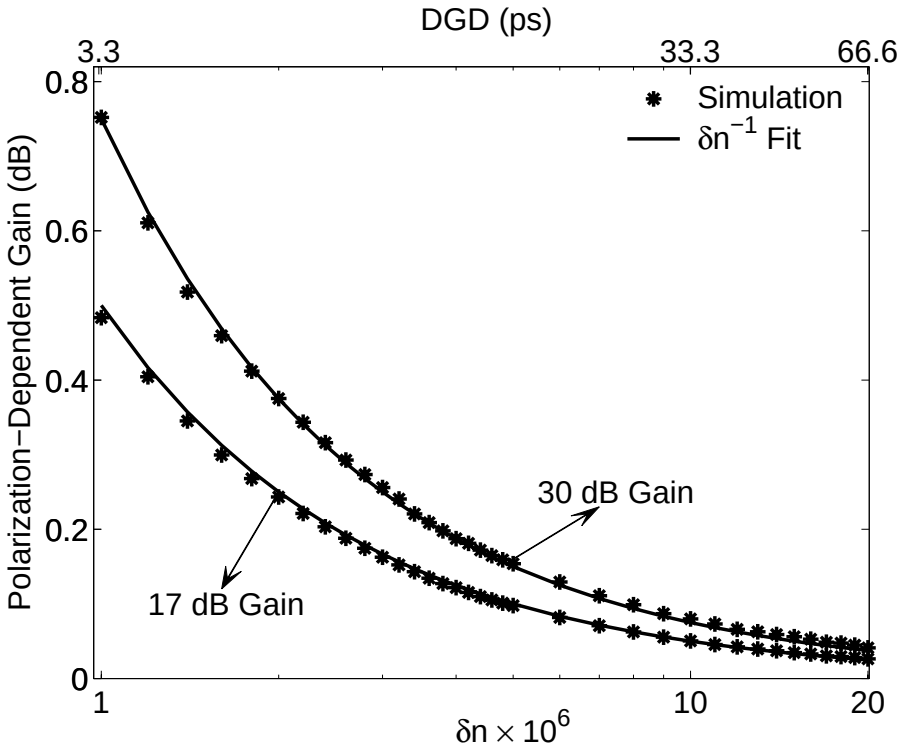

Figure 6.3: Polarization-dependent gain as a function of fiber birefringence for two values of peak gain. The top scale shows the corresponding differential group delay. The solid curves show a fit based on the inverse dependence of PDG on δn.

6.5 Conclusions

In conclusion, this Chapter presented a novel and simple scheme for making single-pump FOPAs exhibiting negligible (<0.1 dB) amount of PDG. Since this scheme makes use of a birefringent fiber, it is not affected by randomly varying residual birefringence and resulting PMD [12], [84], [85]. This scheme has the advantage of simplicity and makes use of only a birefringent fiber.

Bibliography

[1] J. A. Armstrong, N. Bloembergen, J. Ducuing, and P. S. Pershan, "Interactions between light waves in a nonlinear dielectric," Phys. Rev. **127**, 1918–1939 (1962).

[2] R. W. Boyd, *Nonlinear Optics* (Academic Press, San Diego, 1992).

[3] G. P. Agrawal, *Nonlinear Fiber Optics*, 3rd ed. (Academic Press, San Diego, 2001).

[4] R. H. Stolen, J. E. Bjorkholm, and A. Ashkin, "Phase-matched three-wave mixing in silica fiber optical waveguides," Appl. Phys. Lett. **24** 308–310 (1974).

[5] J. Hansryd, P. A. Andrekson, M. Westlund, J. Li, and P. O. Hedekvist, "Fiber-based optical parametric amplifiers and their applications," IEEE J. Sel. Top. Quantum Electron. **8**, 506–520, (2002).

[6] T. Torounidis, H. Sunnerud, P. O. Hedekvist, and P. A. Andrekson, "Amplification of WDM signals in Fiber-Based optical parametric amplifiers," IEEE Photon. Technol. Lett. **15**, 1061–1063 (2003).

[7] G. Kalogerakis, M. E. Marhic, K. K. Y. Wong, L. G. Kazovsky, "Transmission of optical communication signals by distributed parametric amplification," J. Lightwave Technol. **23**, 2945–2953 (2005).

[8] M. N. Islam and Ö. Boyraz, "Fiber parametric amplifiers for wavelength band conversion," IEEE. J. Sel. Top. Quantum Electron. **8**, 527–537 (2002).

[9] G. A. Nowak, Y. Hao, T. J. Xia, M. N. Islam and D. Nolan, "Low-power high-efficiency wavelength conversion based on modulational instability in high-nonlinearity fiber," Opt. Lett. **23**, 936–938 (1998).

[10] C. J. McKinstrie, S. Radic and A. R. Chraplyvy, "Parametric amplifiers driven by two pump waves," IEEE J. Sel. Top. Quantum Electron. **8**, 538–547 (2002).

[11] S. Radic, C. J. McKinstrie, A. R. Chraplyvy, G. Raybon, J. C. Centanni, C. G. Jorgensen, K. Brar and C. Headley, "Continuous-wave parametric gain synthesis using nondegenerate pump four-wave mixing," IEEE Photon. Technol. Lett. **14**, 1406–1408 (2002).

[12] S. Radic and C. J. McKinstrie, "Two-pump fiber parametric amplifiers," Opt. Fiber. Technol. **9**, 7–23 (2003).

[13] A. Yariv, D. Fekete, and D. M. Pepper, "Compensation for channel dispersion by nonlinear optical phase conjugation," Opt. Lett. **4**, 52–54 (1979).

[14] S. Watanabe and M. Shirasaki, "Exact compensation for both chromatic dispersion and Kerr effect in a transmission fiber using optical phase conjugation," J. Lightwave Technol. **14**, 243–248 (1996).

[15] J. Santhanam and G. P. Agrawal, "Reduced timing jitter in dispersion-managed lightwave systems through parametric amplification," J. Opt. Soc. Am. B **20**, 284–291 (2003).

[16] C. J. McKinstrie, S. Radic, and C. Xie, "Reduction of soliton phase jitter by in-line phase conjugation," Opt. Lett. **28**, 1519–1561 (2003).

[17] J. M. C. Boggio, A. Guimarães, F.A. Callegari, J. D. Marconi, M. L. Rocha, M. R. X. deBarros, and H. L. Fragnito, "Parametric amplifier for mid-span phase conjugation with simultaneous compensation of fiber loss and chromatic dispersion at 10 Gb/s," Microwave and Optical Technology Letters, **42**, 503–504 (2004).

[18] J. A. Levenson, I. Abram, T. Rivera, and P. Grangier, "Reduction of quantum noise in optical parametric amplification," J. Opt. Soc. Am. B **10**, 2233–2238 (1993).

[19] I. H. Deutsch and I. Abram, "Reduction of quantum noise in soliton propagation by phase-sensitive amplification," J. Opt. Soc. Am. B **11**, 2303–2313 (1994).

[20] W. Imajuku, A. Takada, and Y. Yamabayashi, "Inline coherent optical amplifier with noise figure lower than 3 dB quantum limit," Electron. Lett. **36**, 63–64 (2000).

[21] J. Li, J. Hansryd, P. O. Hedekvist, P. A. Andrekson, and S. N. Knudsen, "300-Gb/s eye-diagram measurement by optical sampling using fiber-based parametric amplification," IEEE Photon. Technol. Lett. **13**, 987–989 (2001).

[22] P. A. Andrekson, N. A. Olsson, J. R. Simpson, T. Tanbun-Ek, R. A. Logan, M. Haner, "16 Gb/s all optical demultiplexing using four-wave mixing," Electron. Lett. **27**, 922–924 (1991)

[23] T. Sakamoto, K. Seo, K. Taira, N,. S. Moon, K. Kikuchi, "Polarization-insensitive all-optical time-division demultiplexing using a fiber four-wave mixer with a peak-holding optical phase-locked loop," IEEE Photon. Technol. Lett. **16** 563–565 (2004).

[24] J. Hansryd and P. A. Andrekson, "O-TDM demultiplexer with 40-dB gain based on a fiber optical parametric amplifier," IEEE Photon. Technol. Lett. **13**, 732–734 (2001).

[25] Q. Lin, R. Jiang, C. F. Marki, C. J. McKinstrie, R. Jopson, J. Ford, G. P. Agrawal, and S. Radic, "40-Gb/s Optical switching and wavelength multicasting in a two-pump parametric device," IEEE Photon. Technol. Lett. **17** 2376–2378 (2005).

[26] X. Li, P. L. Voss, J. E. Sharping, and P. Kumar, "Optical-fiber source of polarization-entangled photons in the 1550 nm telecomm band," Phys. Rev. Lett. **94**, 53601 (2005)

[27] K. O. Hill, D. C. Johnson, B. S. Kawasaki, and R. I. MacDonald, "cw three-wave mixing in single-mode optical fibers," J. Appl. Phys. **49**, 5098–5106 (1978).

[28] G. P. Agrawal, *Fiber-Optic Communication Systems*, 3rd ed. (Wiley, New York, (2002).

[29] C. Lin, W. A. Reed, A. D. Pearson, H. T. Shang, "Phase matching in the minimum-chromatic-dispersion region of single-mode fibers for stimulated four-photon mixing," Opt. Lett. **6**, 493–495 (1981).

[30] M. Nakazawa, Y. Kimura, and K. Suzuki, "Efficient Er^{3+}-doped optical amplifier pumped by a 1.48 μm InGaAsP laser diode," Appl. Phys. Lett. **54**, 295–297 (1989).

[31] M. E. Marhic, N. Kagi, T. K. Chiang, and L. G. Kazovsky, "Broadband fiber optical parametric amplifiers," Opt. Lett. **21**, 573–575 (1996).

[32] M. E. Marhic, K. K. Y. Wong, L. G. Kazovsky, "Wide-band tuning of th gain spectra of one-pump fiber optical parametric amplifiers," IEEE J. Sel. Top. Quantum Electron. **10**, 1133–1141, (2004).

[33] J. C. Knight, T. A. Birks, P. St. J. Russell, and D. M. Atkin, "All-silica single-mode optical fiber with photonic crystal cladding," Opt. Lett. **21**, 1547–1549 (1996).

[34] R. Tang, P. Devgan, J. Sharping, P. Voss, J. Lasri, P. Kumar, "Microstructure fiber based optical parametric amplifier in the 1550-nm Telecom band," Proc. Opt. Fiber Commun., (Optical Society of America, Washington, DC, 2003), pp. 562–563.

[35] K. Inoue and T. Mukai, "Signal wavelength dependence of gain saturation in a fiber optical parametric amplifier," Opt. Lett. **26**, 10–12 (2001).

[36] M. Ho, K. Uesaka, M. Marhic, Y. Akasaka and L. G. Kazovsky, "200-nm-Bandwidth fiber optical amplifier combining parametric and Raman gain," J. Lightwave Technol. **19**, 977–981 (2001).

[37] K. Shimizu, K. Wong, G. Kalogerakis, K. Uesaka, M. Marhic, L. Kazovsky, "High repetition-rate pulsed-pump fiber OPA for 10Gb/s NPZ modulated signals," Proc. Opt. Fiber Commun. (Optical Society of America, Washington, DC, 2003), pp. 566–567.

[38] M. E. Marhic, F. S. Yang, M. Ho, L. G. Kazovsky, "High-nonlinearity fiber optical parametric amplifier with periodic dispersion compensation," J. Lightwave Technol. **17**, 210–215 (1999).

[39] J. Kim, Özdal Boyraz, J. H. Lim, and M. N. Islam, "Gain enhancement in cascaded fiber parametric amplifier with quasi-phase matching: Theory and experiment," J. Lightwave Technol. **19**, 247–251 (2001).

[40] K. Inoue, "Arrangement of fiber pieces for a wide wavelength conversion range by fiber four-wave mixing," Opt. Lett. **19**, 1189–1191 (1994).

[41] L. Provino, A. Mussot, E. Lantz, T. Sylvestre, and H. Maillotte, "Broadband and flat parametric amplifiers with a multisection dispersion-tailored nonlinear fiber arrangement," J. Opt. Soc. Am. B **20**, 1532–1537 (2003).

[42] W. Zhang, C. Wang, J. Shu, and W. Hu, "Design of fiber-optical parametric amplifiers by genetic algorithm," IEEE Photon. Technol. Lett. **16**, 1652–1654 (2004).

[43] J. Hansryd and P. A. Andrekson, "Broad-band continuous-wave-pumped fiber optical parametric amplifier with 49-dB gain and wavelength-conversion efficiency," IEEE Photon. Technol. Lett. **13**, 194–196 (2001).

[44] T. Torounidis, P. A. Andrekson, and B. E. Olsson, "Fiber-optical parametric amplifier with 70 dB gain," IEEE Photon. Technol. Lett. **18**, 1194–1196 (2006).

[45] K. Inoue, "Polarization independent wavelength conversion using fiber four-wave mixing with two orthogonal pump lights of different frequencies," J. Lightwave Technol. **12**, 1916–1920 (1994).

[46] M. E. Marhic, Y. Park, F. S. Yang, and L. G. Kazovsky, "Broadband fiber-optical parametric amplifiers and wavelength converters with low-ripple Chebyshev gain spectra," Opt. Lett. **21**, 1354–1356 (1996).

[47] C. J. McKinstrie and S. Radic, "Parametric amplifiers driven by two pump waves with dissimilar frequencies," Opt. Lett. **27**, 1138–1140 (2002).

[48] S. Radic, C. J. McKinstrie, R. M. Jopson, J. C. Centanni, Q. Lin and G. P. Agrawal, "Record performance of parametric amplifier constructed with highly nonlinear fibre," Electron. Lett. **39**, 838–839 (2003).

[49] J. M. C. Boggio, J. D. Marconi, and H. L. Fragnito, "Double-pumped fiber optical parametric amplifier with flat gain over 47-nm bandwidth using a conventional dispersion-shifted fiber," IEEE Photon. Technol. Lett. **17**, 1842–1844 (2005).

[50] Q. Lin and G. P. Agrawal, "Vector theory of four-wave mixing: polarization effects in fiber-optic parametric amplifiers," J. Opt. Soc. Am. B **21**, 1216–1224 (2004).

[51] H. Kogelnik, R. M. Jopson, and L. E. Nelson, "Polarization-Mode Dispersion," in *Optical Fiber Telecommunications IV B*, I. P. Kaminow and T. Li, Eds. (Academic, San Diego, 2002), Chap. 15.

[52] P. K. A. Wai and C. R. Menyuk, "Polarization mode dispersion, decorrelation, and diffusion in optical fibers with randomly varying birefringence," J. Lightwave Technol. **14**, 148–157 (1996).

[53] T. I. Lakoba, "Concerning the equations governing the nonlinear pulse propagation in randomly birefringent fibers," J. Opt. Soc. Am. B **13**, 2006–2011 (1996).

[54] C. J. Mckinstrie, H. Kogelnik, R. M. Jopson, S. Radic, and A. V. Kanaev, "Four-wave mixing in fibers with random birefringence," Optics Express, **12**, 2033–2055 (2004).

[55] R. M. Jopson and R. E. Tench, "Polarization-independent phase conjugation of lightwave signals," Electron. Lett. **29**, 2216–2217 (1993).

[56] S. Yamashita and K. Torii, "Polarization-independent highly-efficient optical fiber wavelength converter," Conf. Lasers & Electro-Optics (Optical Society of America, Washington, DC, 2001), pp. 384–385.

[57] P. O. Hedekvist, M. Karlsson, and P. A. Andrekson, "Polarization dependence and efficiency in a fiber four-wave mixing phase conjugator with orthogonal pump waves," IEEE Photon Technol. Lett. **8**, 776–778 (1996).

[58] S. Radic, C. McKinstrie, R. Jopson, C. Jorgensen, K. Brar, and C. Headley, "Polarization dependent parametric gain in amplifiers with orthogonally multiplexed optical pumps," in *Proc. Conf. Optical Fiber Communications (OFC) 2003*, Anaheim, CA, Paper ThK3 (2003).

[59] K. K. Y. Wong, M. E. Marhic, K. Uesaka, and L. G. Kazovsky, "Polarization-independent two-pump fiber optical parametric amplifier." IEEE Photon. Technol. Lett. **14**, 911–913 (2002).

[60] A. Guimaraes, W. A. Arellano, M. O. Berendt, H. L. Fragnito, "Measurement of polarization dependent gain in a dual pump fiber optical parametric amplifier," Conf. Lasers & Electro-Optics, (Optical Society of America, Washington, DC, 2001), pp. 447–448.

[61] T. Tanemura and K. Kikuchi, "Polarization-independent broad-band wavelength conversion using two-pump fiber optical parametric amplification without idler spectral broadening," IEEE Photon. Technol. Lett. **15**, 1573–1575 (2003).

[62] M. Westlund, J. Hansryd, P. A. Andrekson, and S. N. Knudsen, "Transparent wavelength conversion in fiber with 24 nm pump tuning range," Electon. Lett. **38**, 85–86 (2002).

[63] C. Yu, Z. Pan, Y. Wang, Y. W. Song, D. Gurkan, M. C. Hauer, D. Starodubov, and A. E. Willner, "Polarization-insensitive all-optical wavelength conversion using dispersion-shifted fiber with a fiber bragg grating and a Faraday rotator mirror," IEEE Photon. Technol. Lett. **16**, 1906–1908 (2006).

[64] M. Ho, M. E. Marhic, K. Y. K. Wong, and L. G. Kazovsky, "Narrow-linewidth idler generation in fiber four-wave mixing and parametric amplification by dithering two pumps in opposition of phase," J. Lightwave Technol. **20**, 469–476 (2002).

[65] S. Radic, C. J. McKinstrie, R. M. Jopson, J. C. Centanni, A. R. Chraplyvy, C. G. Jorgensen, K. Brar, and C. Headley, "Selective suppression of idler spectral broadening in two-pump parametric architectures," IEEE Photon. Technol. Lett. **15**, 673–675 (2003).

[66] K. Torii and S. Yamashita, "Cancellation of spectral spread by pump frequency modulation in optical fiber wavelength converter," in *Proc. Conf. Optical Fiber Communications (OFC) 2001*, Anaheim, CA, Paper WW5-1.

[67] K. Torii and S. Yamashita, "Efficiency improvement of optical fiber wavelength converter without spectral spread using synchronous phase/frequency modulations," J. Lightwave Technol. **21**, 1039–1045 (2003).

[68] T. Torounidis, H. Sunnerud, P. O. Hedekvist, and P. A. Andrekson, "40-Gb/s transmission using RZ-pulse source based on fiber optical parametric amplification," IEEE Photon. Technol. Lett. **15**, 1159–1161 (2003).

[69] T. Torounidis, M. Westlund, H. Sunnerud, Bengt-Erik. Olsson, and P. A. Andrekson, "Signal generation and transmission at 40, 80 and 160 Gb/s using a fiber-optical parametric pulse source," IEEE Photon. Technol. Lett. **17**, 312–314 (2005).

[70] J. Hansryd and P. A. Andrekson, "Wavelength tunable 40-GHz pulse source based on fiber optical parametric amplifier," Electron. Lett. **37**, 584–585 (2001).

[71] Y. Su, L. Wang, A. Agarwal, and P. Kumar, "All-optical limiter using gain flattened fiber parametric amplifier," Electron. Lett. **36**, 1103–1104 (2000).

[72] E. Ciaramella and S. Trillo, "All-optical signal reshaping via four-wave mixing in optical fibers," IEEE Photon. Technol. Lett. **12**, 849–851 (2000).

[73] K. Inoue, "Suppression of level fluctuation without extinction ratio degradation based on output saturation in higher order optical parametric interaction in fiber," IEEE Photon. Technol. Lett. **13**, 338–340 (2001).

[74] S. Radic, C. J. McKinstrie, R.M. Jopson, J. C. Centanni, and A. R. chrapyvy, "All-optical regeneration in one and two-pump parametric amplifier using highly nonlinear optical fiber," IEEE Photon. Technol. Lett. **15**, 957–959 (2003).

[75] M. E. Marhic, K. K. Y. Wong, M. C. Ho, and L. G. Kazovsky, "92% pump depletion in a continuous-wave one-pump fiber optical parametric amplifier," Opt. Lett. **26**, 620–622 (2001).

[76] M. E. Marhic, K. K. Y. Wong, L. G. Kazovsky, and T. E. Tsai, "Continuous-wave fiber optical parametric oscillator," Opt. Lett. **27**, 1439-1441 (2002).

[77] J. L. Blows and S. E. French, "Low-noise-figure optical parametric amplifier with a continuous-wave frequency-modulated pump," Opt. Lett. **27**, 491–493 (2002).

[78] P. L. Voss, R. Tang, and P. Kumar, "Measurement of the photon statistics and the noise figure of a fiber-optic parametric amplifier," Opt. Lett. **28**, 549–551 (2003),

[79] K. K. Y. Wong, K. Shimizu, M. E. Marhic, K. Uesaka, G. Kalogerakis, and L. G. Kazovsky, "Continuous-wave fiber optical parametric wavelength converter with 40 dB conversion efficieny and a 3.8 dB noise figure," Opt. Lett. **28**, 692–694 (2003).

[80] M. Karlsson, "Four-wave mixing in fibers with randomly varying zero-dispersion wavelength," J. Opt. Soc. Am. B **15**, 2269–2275 (1998).

[81] C. W. Gardiner, *Handbook of Stochastic Methods*, 2nd ed. (Springer, New York, 1985), Chap. 4 pp.92–99.

[82] F. Yaman, Q. Lin, S. Radic, and G. P. Agrawal, "Impact of dispersion fluctuations on dual-pump fiber-optic parametric amplifiers," IEEE Photon Technol. Lett. **16**, 1292–1294 (2004).

[83] M. Karlsson and J. Brentel, "Autocorrelation function of the polarization-mode dispersion vector," Opt. Lett. **24**, 939–941, (1999).

[84] F. Yaman, Q. Lin, and G. P. Agrawal, "Effects of polarization-mode dispersion in dual-pump fiber-optic parametric amplifiers," IEEE Photon Technol. Lett. **16**, 431–433 (2004).

[85] Q. Lin, and G. P. Agrawal, "Effects of polarization-mode dispersion on fiber-based parametric amplifiers and wavelength conversion," Opt. Lett., **29**, 1114–1116, (2004).

[86] M. Karlsson, J. Brentel, and P. A. Andrekson, "Long-term measurement of PMD and polarization drift in installed fibers," J. Lightwave Technol. **18**, 941–951 (2000).

[87] C. M. Caves, "Quantum limits on noise in linear amplifiers," Phys. Rev. D **26**, 1817–1839 (1982)

[88] X. Zhang and B. F. Jorgensen, "Noise characteristics and optimization fiber length of spectral inversion using four-wave mixing in a dispersion-shifted fiber," Opt. Fiber Technol. **3**, 28–43 (1997).

[89] P. O. Hedekvist and P. A. Andrekson, "Noise characteristics of fiber-based optical phase conjugators," J. Lightwave Technol. **17**, 74–79 (1999).

[90] P. Kylemark, P. O. Hedekvist, H. Sunnerud, and M. Karlsson, P. A. Andrekson, "Noise characteristics of fiber optical parametric amplifiers," J. Lightwave Technol. **22**, 409–416 (2004).

[91] G. Kalogerakis, M. E. Marhic, K. K. Y. Wong, and L. G. Kazovsky, "Pump-to-Signal RIN Transfer in Fiber OPAs," in *Proc. Conf. Optical Fiber Communications (OFC) 2003*, Anaheim, CA, Paper CFA5.

[92] F. Yaman, Q. Lin, S. Radic, and G. P. Agrawal, "Pump-noise transfer in dual-pump fiber-optic parametric amplifiers: walk-off effects," Opt. Lett., **30**, 1048–1050 (2005).

[93] P. Kylemark, M. Karlsson, and P. A. Andrekson, "Impact of phase modulation and filter characteristics on dual-pumped fiber-optical parametric amplification," IEEE Photon. Technol. Lett. **18**, 439–441 (2006).

[94] A. Mussot, A. Durecu-Legrand, E. Lantz, C. Simonneau, and D. Bayart, "Impact of pump phase modulation on the gain of fiber optical parametric amplifier," IEEE Photon. Technol. Lett. **16**, 1289–1291 (2004).

[95] A. Durecu-Legrand, A. Mussot, C. Simonneau, D. Bayart, T. Sylvestre, E. Lantz, and H. Maillotte, "Impact of pump phase modulation on system performance of fibre-optical parametric amplifiers," Electron. Lett. **41**, 350–352 (2005).

[96] F. Yaman, Q. Lin, S. Radic, and G. P. Agrawal, "Impact of pump-phase modulation on dual-pump fiber-optic parametric amplifiers," IEEE Photon. Technol. Lett. **17**, 2053–2055 (2005).

[97] J. M. C. Boggio, A. Guimarães, F.A. Callegari, J. D. Marconi, and H. L. Fragnito, "Q penalties due to pump phase modulation and pump RIN in fiber optic parametric amplifiers with non-uniform dispersion," Optics Commun., **249**, 451–472 (2005).

[98] K. Petermann, "FM-AM noise conversion in dispersive single-mode fibre transmission lines," Electron. Lett. **26**, 2097–2098 (1990).

[99] M. E. Marhic, K. Y. K. Wong, L. G. Kazovsky, "Wide-band tuning of the gain spectra of one-pump fiber optical parametric amplifiers," IEEE. J. Sel. Top. Quantum Electron. **10**, 1133–1141 (2004).

[100] B. Huttner, C. Geiser, and N. Gisin,"Polarization-induced distortions in optical fiber networks with polarization-mode dispersion and polarization-dependent losses," IEEE. J. Sel. Top. Quantum Electron. **6**, 317–329 (2000).

[101] D. Q. Chowdhury, and L. Bhagavatula, "Polarization dependent loss induced gain ripple statistics in erbium-doped fiber amplifiers," IEEE Photon. Technol. Lett. **13**, 1301–1303 (2001).

[102] J. P. Gordon and H. Kogelnik, "PMD fundamentals: Polarization mode dispersion in optical fibers," Proc. Natl. Acad. Sci. USA **97**, 4541–4550 (2000).

[103] T. Hasegawa, K. Inoue, and K. Oda, "Polarization independent frequency conversion by fiber four-wave mixing with a polarization diversity technique," IEEE Photon. Technol. Lett. **5**, 947–949 (1993).

[104] A. Tersigni, V. Calle, A. T. Clausen, L. K. Oxenlłwe, J. Młrk and P. Jeppesen, "Polarization independent optical sampling using four-wave mixing," Conf.

Lasers & Electro-Optics, (Optical Society of America, Washington, DC, 2003), paper CMR2.

[105] S. Watanabe, S. Takeda, and T. Chikama, "Interband wavelength conversion of 320 Gb/s (32×10Gb/s) WDM signal using a polarization-insensitive four-wave mixer," in *Eur. Conf. Optical Communications (ECOC)* Copenhagen, Denmark, Paper (1998).

[106] K. K. Y. Wong, M. E. Marhic, K. Uesaka, and L. G. Kazovsky, "Polarization-independent one-pump fiber-optical parametric amplifier," IEEE Photon. Technol. Lett. **14**, 1506–1508 (2002).

[107] M. Westlund, H. Sunnerud, B. E. Olsson, and P. A. Andrekson, "Simple scheme for polarization-independent all-optical sampling," IEEE Photon. Technol. Lett. **16**, 2108–2010 (2004).

[108] P. N. Morgan and J. M. Liu, "Parametric four-photon mixing followed by stimulated Raman scattering with optical pulses in birefringent optical fibers," IEEE J. Quantum Electron. **27**, 1011–1021 (1991).

[109] C. J. McKinstrie, S. Radic, and C. Xie, "Parametric instabilities driven by orthogonal pump waves in birefringent fibers," Ot. Express. **11**, 2619–2633 (2003).

[110] A. S. Lenihan, R. Salem, T. E. Murphy, and G. M. Carter, "All-optical 80-Gb/s time-division demultiplexing using polarization-pnsensitive cross-phase modulation in photonic crystal fiber," IEEE Photon. Technol. Lett. **18**, 1329–1321 (2006).